

Cranfield University at Silsoe
National Soils Resources Institute

MSc by Research
Academic Year 2007/2008

Neil Coalter

Evaluation and proposal for a new PMC Pea
Harvester Support System

Dr James Brighton

2nd January 2008

Abstract

PMC Harvesters Ltd is an OEM (Original Equipment Manufacturer) for the pea and bean market. Their primary product line is a self propelled harvester known as the 979 CT harvester. The 979 CT is of considerable proportions being 4m x 4m x 12m in overall dimensions, six wheel drive and weighs 29,620 kg GVW (Gross Vehicle Weight) when fully laden.

The aim of this work was to identify and outline possible solutions for the support system (tyre or track and undercarriage), quantify the performance of each system, produce a design and evaluation method to determine an optimal structural specification and to produce a design recommendation for the application.

Analysis of the current 979 CT harvester wheel configuration highlighted many constraining factors in tyre choice. The most pertinent of these was that the wheels have a very limited operating space and following a study of the possible tyre options it became apparent only two manufactures, Michelin and Trelleborg, could provide tyres which met the vehicle parameters.

An experiment was conducted to evaluate the performance of the three chosen tyre options. From the findings of these tests it was clear that the optimal tyre for the PMC configuration was the Trelleborg Twin Radial tyre, operating at minimum road inflation pressure (1.6 bar) as designated by Trelleborg.

When operating the harvester in its normal working environment the tyre pressure should be set at minimum road inflation for in-field conditions with a DBD (Dry Bulk Density) of $> 1.3 \text{ g/cm}^3$, as excess damage caused by operating above minimum field operating pressure is superficial.

The use of low compaction equipment such as CTIS (Central Tyre Inflation System) or tracks would not be beneficial to the PMC application. The track tested created a hardened track pan, thus requiring more effort to rectify post harvest. A CTIS

increases the consumption of diesel and offered no reduction in soil compaction below plough depth as shown by the findings from operating the optimal tyre at minimum field inflation pressure (1.2 bar).

The primary objective of this project was to offer solutions to reduce the effects of the PMC harvester's weight on its operating medium. The first natural step was to assess the vehicles main structure in order to improve its performance to weight ratio. The initial phase of this process was to validate the modelling and analyses techniques used to assess the structure. This was done within a controlled test environment at CU@S and from this work a factor of safety of 10% was designated to be applied to all analysis in order to authenticate results and generate a "worst case" answer.

Revisions of the main chassis, main pivot and rear axle assemblies were created and analysed. Test metrics were defined which represented operating patterns of the harvester. The findings from these tests saw a 22.6% weight reduction, 43.1% increase in life expectancy and 10.2% reduction in peak stress in the main chassis and main pivot. Unlike the other two key assemblies, the rear axle was deemed fit for purpose and would not benefit from any further design changes.

Acknowledgements

Throughout the duration of my project I have been very fortunate to receive a lot of help and guidance; I therefore would like to take this opportunity to recognise and thank the individuals and organisations that played an integral role in the completion of this work.

Firstly I would like to thank my sponsors, PMC Harvesters Ltd, Norfolk, England for supporting me in undertaking this project both technically and financially and the National Soil Resources Institute for offering me the opportunity to undertake a further degree and bearing the cost of my tuition fees.

I would like to thank everybody at Cranfield University at Silsoe who has had an involvement in my project, but in particular I would like to thank the following people:

- My supervisor, Dr James Brighton. James' guidance, support and ideas were always invaluable and his challenging nature continually demanded more from me, which I feel has shown in this work.
- Company Supervisor, Mr Robert Plant. Robert's support through this project has been unyielding. He secured the use of resources for all aspects of the project from test equipment to vehicles for transportation and without his support the project would not have been possible.
- Mr Roy Newland, for the countless hours of soil bin preparation and knowledge of soil testing techniques.
- Dr Dirk Ansorge, for guidance on operating the single wheel test rig, exchanging ideas and an insight into track operation.
- Mr Roger Swatland and Mr Simon Stranks for assisting with experiment set-up and results gathering.
- Dr Kim Blackburn and Dr Terence Richards, for their support and technical knowledge on all aspects of instrumentation.

Finally I would like to thank Miss Hannah Cessford for the countless number of hours spent proof reading my thesis.

Thank you to everyone for your support.

Table of Contents

Abstract.....	I
Acknowledgements	III
Table of Contents	IV
List of Figures	IX
List of Tables	XIV
List of Equations	XV
List of Abbreviations.....	XVII
1 Introduction.....	1
1.1 Aim	3
1.2 Objectives.....	3
2 Details of Tyre Laboratory Studies	4
2.1 Methodology.....	4
2.2 Tyres.....	4
2.2.1 Tyre Specification	5
2.2.1.1 Trelleborg 425 Tyre.....	5
2.2.1.2 Trelleborg Twin Radial Tyre	5
2.2.1.3 Michelin Mega Xbib Tyre	5
2.3 Tyre Testing Process.....	6
2.3.1 Test 1	6
2.3.2 Test 2	6
2.3.3 Test 3	7
2.3.4 Test 4.....	7
2.4 Soil Dynamics Laboratory and Soil Conditions	8
2.4.1 Standard Bin Preparation.....	8
2.4.2 Soil Properties.....	9
2.5 Measurement Devices & Techniques	9
2.5.1 Dry Bulk Density	9
2.5.2 Moisture Content.....	11
2.5.3 Rut Profile.....	12
2.5.4 Cone Penetration Resistance.....	12

2.5.4.1	Penetrometer	12
2.6	Soil Deformation and Measurement	13
2.6.1	Soil Deformation	13
2.6.2	Soil Preparation for Deformation Measurement.....	14
2.7	Single Wheel Tester	15
2.7.1	Propulsion Method	17
2.8	Draft Force	17
2.9	Statistical Analysis.....	18
3	Soil Data Processing	20
3.1	Penetration Resistance Processing	20
3.2	Resolution of Measurement Techniques	22
3.2.1	Penetration Resistance	22
3.2.2	Deformation Measurement	23
3.3	Error Analysis.....	23
4	Literature Review	25
4.1	Soil	25
4.2	Compaction Under Tyres	26
4.2.1	Tyre Geometry	27
4.2.2	Tyre Construction.....	27
4.2.3	Lug Effect	28
4.2.4	Inflation Pressure	29
4.2.5	Vertical Load	29
4.3	Tyre Configuration.....	30
4.4	Tracks.....	31
4.4.1	Steel track	31
4.4.2	Rubber Tracks.....	31
4.4.3	Track vs. Tyre Performance Comparison.....	33
4.5	The Overall Effects of Soil Compaction for the Grower	34
4.5.1	Growth Potential Consequences of Soil Compaction	34
4.5.2	Rectification and Financial Costs	34
4.6	Key Areas of Influence	35
5	Results and Discussions.....	36
5.1	Triaxial Testing.....	36
5.2	Contact Patch.....	37

5.3	Study 1 – Compaction Comparison of the Three Chosen Tyres.	38
5.3.1	Further Analysis of the Three Tyre Options.....	40
5.4	Study 2 – Effect of Wheel Load on Penetration Resistance	41
5.5	Study 3 – Comparison of Transition Methods	43
5.6	Study 4 – Comparison between Operating Pressures	44
5.7	Rut Characteristics	46
5.8	Dry Bulk Density	47
5.9	Configuration Comparison	48
5.10	Compaction Remediation	50
6	FEA Laboratory Study.....	52
6.1	Structural Analysis.....	52
6.2	Methodology.....	52
6.3	Testing Criteria	54
6.4	Facilities & Equipment	56
6.5	Review of the Calibration Frame Potential	56
6.6	Hydraulic System.....	61
6.7	Strain Gauges and Installation Techniques	62
6.8	Gauge Location.....	63
6.9	Testing Procedure	64
6.9.1	Comparison between Computational and Measured Results	66
6.10	Calculation of Loads	66
6.11	Measured Results Processing	67
6.12	Computational Result Processing	70
7	FEA Results and Discussions.....	73
7.1	Single Load Tests.....	73
7.2	Multi load tests	75
7.3	Prediction of Tests	77
7.4	FEA comparison with Welding Institute report and Ansys on chassis.....	79
8	Support Structure Development	81
8.1	Modelling Technique	81
8.2	Main Pivot	82
8.2.1	Main Pivot Loading Criteria.....	82
8.3	Main Pivot Development	83
8.3.1	Current Main Pivot.....	83

8.3.2	Revision 1	83
8.3.3	Revision 2	83
8.3.4	Revision 3	85
8.4	Rear Axle.....	85
8.4.1	Rear Axle Loading Criteria	86
8.5	Rear Axle Development.....	87
8.5.1	Current Rear Axle	87
8.5.2	Revision 1	87
8.6	Main Chassis	88
8.6.1	Main Chassis Loading Criteria	89
8.7	Main Chassis Development.....	89
8.7.1	Current Main Chassis	89
8.7.2	Revision 1	90
8.7.3	Revision 2	90
9	Results & Discussions – FEA	92
9.1	Main Pivot	92
9.1.1	Peak Stress Analysis.....	92
9.1.2	Preliminarily Analysis of the Main Pivot.....	93
9.1.3	Analysis of Sectioned Main Pivot.....	94
9.1.4	Comparison of Values	97
9.2	Rear Axle.....	98
9.2.1	Peak Stresses.....	98
9.2.2	Preliminarily Analysis of the Rear Axle	98
9.2.3	Analysis of Sectioned Rear Axle	99
9.2.4	Comparison of Values	101
9.3	Main Chassis	102
9.3.1	Peak Stresses.....	102
9.3.2	Preliminarily Analysis of the Main Chassis	103
9.3.3	Analysis of Sectioned Main Chassis	103
9.3.3.1	Standard Chassis – Dog Leg	104
9.3.3.2	Revision 2 – Dog Leg.....	105
9.3.3.3	Standard Chassis – Levelling Structure.....	106
9.3.3.4	Revision 2 – Levelling Structure.....	107
9.3.4	Comparison of Values	108

10	Conclusions	110
10.1	Tyre Tests	110
10.2	FEA Verification.....	111
10.3	Structural Development	111
10.3.1	Main Pivot	111
10.3.2	Rear Axle	112
10.3.3	Main Chassis.....	112
11	Recommendations.....	113
12	References	115
13	Appendix A	118
13.1	Penetration Graphs.....	118
13.2	Deformation Graphs.....	128
14	Appendix B	144
14.1	FEA Verification.....	144
15	Appendix C	146
15.1	Support System Development	146
15.1.1	Picking Head Lugs	146
15.1.2	Tractive Forces.....	149
15.1.3	Side Impact	151
15.1.4	Levelling Rams	152
15.1.5	Stub Axle Calculation	154

List of Figures

Figure 2.1: Trelleborg 425 Tyre.....	5
Figure 2.2: Trelleborg Twin Radial Tyre	5
Figure 2.3: Michelin Mega Xbib Tyre	5
Figure 2.4: Soil bin at CU@S	9
Figure 2.5: Hammer, knife and cylindrical sample ring.....	10
Figure 2.6: Profile meter.....	12
Figure 2.7: a) Sample plate and b) Cone penetrometer	143
Figure 2.8: Talc layers in the soil profile.....	14
Figure 2.9: Sectioned view of the soil profile after 3 rd pass	15
Figure 2.10: Single wheel tester.....	16
Figure 2.11: Final reduction mounting point and linear bearing track.....	17
Figure 2.12: Tine used for compaction alleviation	18
Figure 3.1: Experimental data for one of the 3 rd pass measurements of the 680 loaded with 50 kN @ 1.2 bar	20
Figure 3.2: Average of left and right hand sides of bin.....	21
Figure 3.3: Average penetration value below tyre centreline.....	22
Figure 3.4: Layer displacement change through bin section	24
Figure 4.1: Comparison of radial and cross ply tyres under load	28
Figure 4.2: Shear stress generated by (a) single track vs. (b) four tyre counterpart. (Wong 2004).....	33
Figure 5.1: Displacement vs. Time, triaxial test result.....	36
Figure 5.2: Penetration resistance vs. Depth for the three proposed tyre solutions.....	38
Figure 5.3: Deformation vs. Depth for three proposed tyre solutions.....	40
Figure 5.4: Plot of deformation at key layer depths.....	41
Figure 5.5: Penetration resistance vs. Depth for three axle loads	41
Figure 5.6: Deformation vs. Depth for three axle loads	42
Figure 5.7: Penetration resistance vs. Depth for driven and towed wheels.....	43
Figure 5.8: Deformation vs. Depth for Driven and Towed wheels.....	44
Figure 5.9: Penetration resistance vs. Depth for two different operating pressures	45
Figure 5.10: Deformation vs. Depth for two different operating pressures	46
Figure 5.11: Average dry bulk density during tyre testing.....	48

Figure 5.12: Penetration resistance vs. Depth for Claas track and PMC tyre comparison.....	49
Figure 5.13: Deformation vs. Depth for Claas track/wheel vs. PMC tri-axle wheel configuration.....	50
Figure 5.14: Draft force.....	51
Figure 6.1: Exploded view of PMC Main Pivot.....	54
Figure 6.2: Single load case.....	55
Figure 6.3: Multiple loading case.....	55
Figure 6.4: Calibration frame.....	56
Figure 6.5: FEA screenshot of calibration frame during analysis.....	57
Figure 6.6: Main pivot stand.....	558
Figure 6.7: FEA screenshot of main pivot stand under defined loading criteria.....	58
Figure 6.8: Cylinder mount.....	59
Figure 6.9: FEA screenshot of cylinder mount.....	59
Figure 6.10: Full model of instrumentation facilities at CU@S.....	60
Figure 6.11: Layout drawing of the test bed with three detailed views.....	60
Figure 6.12: Schematic of the hydraulic system.....	61
Figure 6.13: Data logger circuit diagram.....	63
Figure 6.14: Gauge positions on axle web.....	64
Figure 6.15: Position of strain gauge on upper flange.....	64
Figure 6.16: Axle during testing.....	65
Figure 6.17: EORT and bottle jack being used during testing.....	65
Figure 6.18: Analysed main pivot assembly showing gauge locations.....	66
Figure 6.19: EORT calibration graph and equation.....	67
Figure 6.20: Strain vs. Load for strain gauge.....	69
Figure 6.21: Diagrammatic view of Poisson's ratio.....	70
Figure 6.22: Graphical representation of von Mises and Tresca criteria.....	71
Figure 7.1: Error plot for gauge 1 and gauge 5 for single load test.....	74
Figure 7.2: Average error for gauge 1 and gauge 5 for single load test.....	75
Figure 7.3: Error plot for gauge 1 and gauge 5 for multi-load test.....	76
Figure 7.4: Average error for gauge 1 and gauge 5 for multi load test.....	77
Figure 7.5: Prediction of errors in stress values at 200 kN in single load test.....	78
Figure 7.6: Prediction of errors in stress values at 200kN in multi load test.....	78
Figure 8.1: Exploded drawing sheet for 979 CT main pivot.....	82

Figure 8.2: Exploded view of 979 CT rear axle.....	86
Figure 8.3: Exploded drawing of 979 CT chassis.....	88
Figure 9.1: Triangulation of forces	93
Figure 9.2: Equivalent stress vectors distribution.....	94
Figure 9.3: Sectioned view of standard main pivot under maximum loading criteria .	95
Figure 9.4: Sectioned view of the main pivot - revision 3 under maximum loading criteria.....	96
Figure 9.5: Force vector plot of the axle when under a normal static load condition..	99
Figure 9.6: Sectioned view of the standard rear axle	100
Figure 9.7: Sectioned view of the revised rear axle	101
Figure 9.8: Stress vectors in standard main chassis during normal loading.....	103
Figure 9.9: Cross brace network located on the underside of the current main chassis dogleg	104
Figure 9.10: Cross brace network located on the underside of the revision 2 main chassis dogleg	105
Figure 9.11: Standard chassis showing levelling structure under load	106
Figure 9.12: Revision 2 main chassis showing levelling structure under load.....	107
Figure 13.1: Michelin tyre control	118
Figure 13.2: Michelin tyre, 1st pass @MMRI, 50 kN load.....	118
Figure 13.3: Michelin tyre, 2nd pass @MMRI, 50 kN load.....	119
Figure 13.4: Michelin tyre, 3rd pass @MMRI, 50 kN load	119
Figure 13.5: Trelleborg 425 tyre control	119
Figure 13.6: Trelleborg 425 tyre, 1st pass @MMRI, 50 kN load.....	120
Figure 13.7: Trelleborg 425 tyre, 2nd pass @MMRI, 50 kN load.....	120
Figure 13.8: Trelleborg 425 tyre, 3rd pass @MMRI. 50 kN load	120
Figure 13.9: Trelleborg Twin Radial Control.....	121
Figure 13.10: Trelleborg Twin Radial, 1st pass @1.6 Bar, 45 kN	121
Figure 13.11: Trelleborg Twin Radial, 2nd pass @1.6 Bar, 45 kN	121
Figure 13.12: Trelleborg Twin Radial, 3rd pass @1.6 Bar, 45 kN.....	122
Figure 13.13: Trelleborg Twin Radial, Control, load 40 kN.....	122
Figure 13.14: Trelleborg Twin Radial, 1st pass @MMRI, load 40 kN.....	122
Figure 13.15: Trelleborg Twin Radial, 2nd pass @MMRI, load 40 kN	123
Figure 13.16: Trelleborg Twin Radial, 3rd pass @MMRI, load 40 kN.....	123
Figure 13.17: Trelleborg Twin Radial, Control, load 45 kN.....	123

Figure 13.18: Trelleborg Twin Radial, 1st pass @MMRI, load 45 kN.....	124
Figure 13.19: Trelleborg Twin Radial, 2nd pass @MMRI, load 45 kN	124
Figure 13.20: Trelleborg Twin Radial, 3rd pass @MMRI, load 45 kN.....	124
Figure 13.21: Trelleborg Twin Radial, Control, load 50 kN.....	125
Figure 13.22: Trelleborg Twin Radial, 1st pass @MMRI, load 50 kN.....	125
Figure 13.23: Trelleborg Twin Radial, 2nd pass @MMRI, load 50 kN	125
Figure 13.24: Trelleborg Twin Radial, 3rd pass @MMRI, load 50 kN.....	126
Figure 13.25: Trelleborg Twin Radial, Control, load 45 kN, trailed	126
Figure 13.26: Trelleborg Twin Radial, 1st pass @MMRI, load 45 kN, trailed.....	126
Figure 13.27: Trelleborg Twin Radial, 2nd pass @MMRI, load 45 kN, trailed	127
Figure 13.28: Trelleborg Twin Radial, 3rd pass @MMRI, load 45 kN, trailed	127
Figure 13.31: Control sample for Michelin wheel at MMRI with 50 kN	129
Figure 13.32: 3rd pass sample for Michelin wheel at MMRI with 50 kN test.....	129
Figure 13.33: 3rd pass sample for Michelin wheel at MMRI with 50 kN test.....	130
Figure 13.34: 3rd pass sample for Michelin wheel at MMRI with 50 kN test.....	130
Figure 13.35: Control sample for Trelleborg 425 wheel at MMRI with 50 kN test..	130
Figure 13.36: Control sample for Trelleborg 425 wheel at MMRI with 50 kN test..	131
Figure 13.37: Control sample for Trelleborg 425 wheel at MMRI with 50 kN test..	131
Figure 13.38: 3rd pass sample for Trelleborg 425 wheel at MMRI with 50 kN test.	131
Figure 13.39: 3rd pass sample for Trelleborg 425 wheel at MMRI with 50 kN test.	132
Figure 13.40: 3rd pass sample for Trelleborg 425 wheel at MMRI with 50 kN test.	132
Figure 13.41: Control sample for Trelleborg Twin Radial wheel at MMRI with 40 kN test	132
Figure 13.42: Control sample for Trelleborg Twin Radial wheel at MMRI with 40 kN test	133
Figure 13.43: Control sample for Trelleborg Twin Radial at MMRI with 40 kN test	133
Figure 13.44: 3rd pass sample for Trelleborg Twin Radial wheel at MMRI with 40 kN test	133
Figure 13.45: 3rd pass sample for Trelleborg Twin Radial wheel at MMRI with 40 kN test	134
Figure 13.46: 3rd pass sample for Trelleborg Twin Radial wheel at MMRI with 40 kN test	134

Figure 13.47: Control sample for Trelleborg Twin Radial wheel at MMRI with 45 kN test	134
Figure 13.48: Control sample for Trelleborg Twin Radial wheel at MMRI with 45 kN test	135
Figure 13.49: Control sample for Trelleborg Twin Radial wheel at MMRI with 45 kN test	135
Figure 13.50: 3rd pass sample for Trelleborg Twin Radial wheel at MMRI with 45 kN test	135
Figure 13.51: 3rd pass sample for Trelleborg Twin Radial wheel at MMRI with 45 kN test	136
Figure 13.52: 3rd pass sample for Trelleborg Twin Radial wheel at MMRI with 45 kN test	136
Figure 13.53: Control sample for Trelleborg Twin Radial wheel at MMRI with 50 kN test	136
Figure 13.54: Control sample for Trelleborg Twin Radial wheel at MMRI with 50 kN test	137
Figure 13.55: Control sample for Trelleborg Twin Radial wheel at MMRI with 50 kN test	137
Figure 13.56: 3rd pass sample for Trelleborg Twin Radial wheel at MMRI with 50 kN test	137
Figure 13.57: 3rd pass sample for Trelleborg Twin Radial wheel at MMRI with 50 kN test	138
Figure 13.58: 3rd pass sample for Trelleborg Twin Radial wheel at MMRI with 50 kN test	138
Figure 13.59: Control sample for Trelleborg Twin Radial wheel at MMRI with 45 kN test, trailed.....	138
Figure 13.60: Control sample for Trelleborg Twin Radial wheel at MMRI with 45 kN test, trailed.....	139
Figure 13.61: Control sample for Trelleborg Twin Radial wheel at MMRI with 45 kN test, trailed.....	139
Figure 13.62: 3rd pass sample for Trelleborg Twin Radial wheel at MMRI with 45kN test, trailed.....	139
Figure 13.63: 3rd pass sample for Trelleborg Twin Radial wheel at MMRI with 45kN test, trailed.....	140

Figure 13.64: 3rd pass sample for Trelleborg Twin Radial wheel at MMRI with 45kN test, trailed.....	140
Figure 13.65: Control sample for Trelleborg Twin Radial wheel at 1.6 bar with 50 kN test	140
Figure 13.66: Control sample for Trelleborg Twin Radial wheel at 1.6 bar with 50 kN test	141
Figure 13.67: Control sample for Trelleborg Twin Radial wheel at 1.6 bar with 50 kN test	141
Figure 13.68: 3rd pass sample for Trelleborg Twin Radial wheel at 1.6 bar with 50 kN test	141
Figure 13.69: 3rd pass sample for Trelleborg Twin Radial wheel at 1.6 bar with 50 kN test	142
Figure 13.70: 3rd pass sample for Trelleborg Twin Radial wheel at 1.6 bar with 50 kN test	142

List of Tables

Table 2.1: Trelleborg 425 specification.....	5
Table 2.2: Trelleborg Twin Radial specification	5
Table 2.3: Michelin Mega Xbib Specification.....	5
Table 2.4: Experiment details – Test 1	6
Table 2.5: Experiment details – Test 2.....	6
Table 2.6: Experiment details – Test 3.....	7
Table 2.7: Experiment details – Test 4.....	7
Table 5.1: Triaxial test results.....	37
Table 5.2: Contact patch geometry of the tyres	37
Table 5.3: Rut characteristics.....	47
Table 5.4: Comparison of draft force requirements	51
Table 6.1: Bill of Materials for hydraulic system	61
Table 6.2: Gauge configuration	63
Table 6.3: Excel processing table.....	68

Table 7.1: Results for gauge number 1 under single loading	73
Table 7.2: Results for gauge number 5 under single loading	74
Table 7.3: Results for gauge number 1 under multi loading	76
Table 7.4: Results for gauge number 5 under multi loading	76
Table 7.5: Comparison of Welding Institute testing and Ansys 10 simulations.....	79
Table 8.1: Design changes for main pivot revision 1	83
Table 8.2: Design changes for main pivot revision 2.....	84
Table 8.3: Design changes for main pivot revision 3.....	85
Table 8.4: Design changes for rear axle revision 1	87
Table 8.5: Design changes for standard chassis revision 1	90
Table 8.6: Design changes for standard chassis revision 2	91
Table 9.1: Peak stresses measured on the four front axle models.....	92
Table 9.2: Standard and revised main pivot stress comparison	97
Table 9.3: Peak stresses measured on the standard and revised rear axle	98
Table 9.4: Standard and revised rear axle peak stress comparison	102
Table 9.5: Peak stresses measured on the standard and revised main chassis.....	102
Table 9.6: Standard and revised main chassis equivalent stress comparison	108
Table 9.7: Shear stress comparison between standard and revision 2 chassis.....	109
Table 9.8: Deformation comparison between standard and revision 2 chassis	109

List of Equations

Equation 2.1: Dry bulk density	10
Equation 2.2: Moisture content.....	11
Equation 6.1: EORT calibration co-efficient.....	67
Equation 6.2: Strain calculation	68
Equation 6.3: Strain vs. Load.....	69
Equation 6.4: Maximum normal stress – rosette gauge set, 3 gauges wired.....	69
Equation 6.5: Maximum normal stress – rosette gauge set, 2 gauges wired.....	70
Equation 6.6: Poisson’s ratio	70
Equation 6.7: Tresca (Maximum shear stress).....	71

Equation 6.8: Equivalent stress (von Mises)72

List of Abbreviations

1 Introduction

It became apparent in the late 1800's that as traction engines began to be used to generate the power required to pull basic ploughs for land cultivation, mechanisation within the agricultural industry was inevitable. However, it wasn't until the late 1930's that the first major progression was made, with machines such as the Ferguson Tractor and Massey Harris Combine.

PMC Harvesters Ltd, formerly FMC Technologies Ltd, have been producing pea harvesters in Fakenham, Norfolk, England since 1970. The first harvester produced at Fakenham was the H2. The H2 was a tandem axle trailed harvester operating on Vredestein eight ply 'super single' tyres with a maximum permissible gross weight of 7,650 kg. Within 6 years of H2 production FMC developed the first self-propelled harvester. This machine, the 679, utilised a wheel configuration similar to a modern combine with two large diameter wheels on the front axle and two smaller variants on the rear. The 679 was much heavier than the H2 with its maximum permissible gross weight stated as 14,700 kg. The next evolution of the harvester produced at Fakenham was the 879 in 1984; this vehicle maintained the "combine" wheel configuration, but again was subjected to an increase in maximum gross weight to approximately 18,500 kg. In 1988 the first self propelled harvester with six equally sized wheels was produced at Fakenham; the maximum gross weight was further increased to 27,620 kg. However with the addition of two wheels, individual wheel loads were marginally reduced, and utilising this new configuration it was found that a reduction in compaction of 17% was achieved, when compared to its 879 four wheel counterpart (Smith (1989)). The 979 is still in production today, albeit in a highly evolved state; the wheel configuration remains the same as it was in 1989, however the weight has increased by a further 2000 kg, to 29620 kg gross weight. The gross weight is spread equally over the three axles, resulting in an axle load of approximately 10,000 kg, with a wheel load of 5000 kg, when fully laden in field conditions. The main increase in vehicle gross mass has been generated by the additional strengthening of the vehicle support system, which is defined as the front axle, rear axle and main chassis.

Quantifying the evolution of the FMC/PMC pea harvester it is possible to state the following: Gross weight has increased by 287% and crop yield increased in excess of 100% from that achieved with the original 679 (Hewitt, 2006). The crop yield increase is not directly related to the increase in gross weight, instead it is accredited to an increase in threshing capacity generated by the increased threshing reel volume.

Although agricultural mechanisation has been developing since the early 1900's, it was not until 1970 that the detrimental effects of using large machinery in crop harvesting were recognised. A report published by the Agricultural Advisory Council in 1970 explained how the "wet" harvest of 1968 had resulted in severe damage to the land. After severe compaction it has been proven that there is a reduction in crop yield; this occurs because open pores become consolidated, thus leading to a reduction in pore space. The reduction not only blocks crop root passage but also reduces passage of water and nutrients. This can lead to localised flooding and as a large majority of crop production land is located in relatively flat regions, such as the Fens in the UK, then flooding will severely affect yields.

Peas are a high value crop, with current market values at approximately £250 per metric ton, this, coupled with strict guidelines enforced by the frozen pea market sector, means quality is paramount. The frozen food industry requires young "green" peas with low tender ratings. For instance, Birdseye requires peas to be frozen within 150 minutes, from their time of harvest, and as a consequence, peas are harvested on the grounds of their readiness for market, rather than field conditions. In dry summer conditions this does not pose any major issues for the growers, however with the UK weather being as unpredictable as it is, harvesting can take place on saturated soils, thus leading to severe compaction. This compaction can, in extreme cases, be at such a level that remediation is not possible.

Compaction rectification is an expensive and time dependent process; consequently modern farming practices strive to reduce compaction potential in preference to compaction remediation.

As an OEM, PMC Harvesters recognise their responsibility to the environment and the potential implications their primary product has on it, therefore by reviewing the

current vehicle configuration in terms of support system layout, method of support and vehicular gross weight a better understanding of the impact of the machine may be gained. By coupling these areas, a heightened knowledge of the PMC 979 CT will be gained and thus allow for more advanced design practices to be implemented within the company, leading to a greater awareness of the product and techniques which should be applied in its design.

1.1 Aim

To determine the performance of possible pea harvester support systems and recommend a design specification to reduce soil compaction.

1.2 Objectives

- To identify the design brief and potential solutions for the support system,
- To quantify the performance of each system,
- To produce a design and evaluation method to determine the optimal structural system specification,
- To produce a design recommendation for the application.

2 Details of Tyre Laboratory Studies

2.1 Methodology

This study quantified the relative performance of the three suitable tyres available for the PMC application. The tests were undertaken within the soil dynamics laboratory at Cranfield University at Silsoe, CU@S. By using a controlled environment, rather than a field, soil variability was reduced and accuracy during the testing sequence increased.

Each sequence of measurements was repeated three times during the test process with the following key factors being recorded:

- Soil penetration resistance
- Soil deformation
- Soil bulk density
- Rut profile
- Moisture content

For each test, the tyre completed three runs along the length of the soil bin to mimic one pass of a complete harvester. Following the findings from the triaxial tests (Section 5.1) a constant 15 minute interval was maintained between each run to eliminate errors due to reconsolidation of the soil between tests. The forward velocity of the wheel was maintained at 1 ms^{-1} .

2.2 Tyres

The PMC 979 CT Harvester has many constricting factors with respect to tyre choice, mainly due to its current configuration and working environment requirements. The harvester has the following levelling capabilities: 8.5 degrees fore and aft, 10.2 degrees side to side. Consequently, for a tyre to be suitable it must fit within an “envelope” of 1.5 m diameter and 0.8 m wide. Due to these constraining factors, the

following three tyres were selected for testing: Trelleborg 425, Trelleborg Twin Radial and Michelin Mega Xbib.

2.2.1 Tyre Specification

2.2.1.1 Trelleborg 425 Tyre

Table 2.1: Trelleborg 425 specification

Tyre	Trelleborg T425
Tyre Dimensions	700/50 - 26.5
Static Loaded Radius	0.57 m
Rolling Circumference	4.05 m
Road Pressure	2.2 bar
Field Pressure	1.6 bar



Figure 2.1: Trelleborg 425 Tyre

2.2.1.2 Trelleborg Twin Radial Tyre

Table 2.2: Trelleborg Twin Radial specification

Tyre	Trelleborg TwinRadial
Tyre Dimensions	680/55 - 26.5
Static Loaded Radius	0.63 m
Rolling Circumference	4.21 m
Road Pressure	1.6 bar
Field Pressure	1.2 bar



Figure 2.2: Trelleborg Twin Radial Tyre

2.2.1.3 Michelin Mega Xbib Tyre

Table 2.3: Michelin Mega Xbib Specification

Tyre	Michelin Mega Xbib
Tyre Dimensions	750/65 - 26
Static Loaded Radius	0.622 m
Rolling Circumference	4.469 m
Road Pressure	2.0 bar
Field Pressure	1.6 bar



Figure 2.3: Michelin Mega Xbib Tyre

2.3 Tyre Testing Process

The tyre testing process was split into four main areas of interest - tyre geometry, vertical load, propulsion method and inflation pressure.

2.3.1 Test 1

Test 1 involved the three different tyres, each inflated to their minimum manufacturer recommended inflation pressure, self propelled and subject to a constant vertical load.

Table 2.4: Experiment details – Test 1

Tyre	Tyre Dimensions	Inflation Pressure (bar)	Vertical Load (kN)	Propulsion Method
Trelleborg 425	700/50 - 26.5	1.6	50	Self Propelled
Trelleborg Twin Radial	680/55 - 26.5	1.2	50	Self Propelled
Michelin Mega Xbib	750/65 - 26	1.6	50	Self Propelled

2.3.2 Test 2

In Test 2 the Trelleborg Twin Radial tyre was inflated to the minimum manufacturer recommended pressure and then tested using three different vertical loads.

Table 2.5: Experiment details – Test 2

Tyre	Tyre Dimensions	Inflation Pressure (bar)	Vertical Load (kN)	Propulsion Method
Trelleborg Twin Radial	680/55 - 26.5	1.2	40	Self Propelled
Trelleborg Twin Radial	680/55 - 26.5	1.2	45	Self Propelled
Trelleborg Twin Radial	680/55 - 26.5	1.2	50	Self Propelled

2.3.3 Test 3

Test 3 investigated the distinction between self propelled and towed wheel test methods. The Trelleborg Twin Radial was used and inflated to the manufacturers minimum recommended pressure.

Table 2.6: Experiment details – Test 3

Tyre	Tyre Dimensions	Inflation Pressure (bar)	Vertical Load (kN)	Propulsion Method
Trelleborg Twin Radial	680/55 - 26.5	1.2	45	Self Propelled
Trelleborg Twin Radial	680/55 - 26.5	1.2	45	Towed

2.3.4 Test 4

Test 4 compared the influence of inflation pressure on compaction through the soil profile. The tyre used was the Trelleborg Twin Radial and the vertical load was maintained at a constant throughout the test sequence.

Table 2.7: Experiment details – Test 4

Tyre	Tyre Dimensions	Inflation Pressure (bar)	Vertical Load (kN)	Propulsion Method
Trelleborg Twin Radial	680/55 - 26.5	1.2	50	Self Propelled
Trelleborg Twin Radial	680/55 - 26.5	1.6	50	Self Propelled

2.4 Soil Dynamics Laboratory and Soil Conditions

2.4.1 Standard Bin Preparation

The tyre tests were undertaken in the soil dynamics laboratory located at CU@S, as shown in Figure 2.4; the soil bin is a concrete lined pit 20 m long, 1.5 m wide and 1 m deep. The bin is prepared using a soil processor that runs along a set of rails located immediately above the bin. The processor is powered by an IC diesel engine and wire ropes. The processor has three main features - grab, levelling blade and 750 kg roller. The rails are used as the datum point. Before commencing bin preparation the soil is scraped away from the testing zones to the opposite end of the bin. The grab, which is capable of lifting approximately 0.5 m³ of soil, is used to carry the soil to the front of the bin where it is then levelled at the required height by the blade, thus spreading the soil along the length of the test section. The normal layer levels are set at 50 mm increments; once each level has been reached it is rolled to increase the bulk density of the soil. The rolling preparation governs the bulk density; increasing the number of rolls increases the bulk density. As a medium bearing capacity soil (1.38 gcm⁻³) was to be used for all tests, each layer received a single roll. Once the layer is rolled it is then wetted; the wetting process governs the level of moisture found within the test soil. The actual moisture level is calculated after the test sequence has been completed.



Figure 2.4: Soil bin at CU@S

2.4.2 Soil Properties

The soil used in the soil laboratory at CU@S is a sandy loam soil with a particle composition of 66% sand, 17% silt and 17% clay. Sandy loam soil accounts for over 25% of UK and European arable land. This soil is used because of its highly replicable nature and the results obtained may be used as a prediction tool for other soil types.

2.5 Measurement Devices & Techniques

2.5.1 Dry Bulk Density

The dry bulk density was measured from soil samples taken from three locations within both the control and test zones of the soil profile. The samples were removed from the following depths: 0, 250 and 500 mm from the upper surface. To acquire the samples, a hollow cylindrical ring (shown in Figure 2.5) of known volume was driven

into the soil face. The soil around the ring was then carefully removed using a knife and the soil sample placed into a tin of known mass. The tins were then reweighed and the new masses recorded. Subsequently, the tins were placed in an oven, which was preheated to 105°C, for 48 hours to dry out. The dried samples were then removed and reweighed. Dry bulk density was calculated by the taking the difference between the wet and dry masses and dividing it by the known volume of the ring as shown in Equation 2.1.

$$\rho_{db} = \frac{m_{wet} - m_{dry}}{v}$$

Equation 2.1: Dry bulk density

where:

ρ_{db}	dry bulk density, kgm^{-3}
m_{wet}	wet mass, kg
m_{dry}	dry mass, kg
v	volume, m^3

Although the weighing equipment used has an accuracy of ± 0.01 g, this technique has a relatively large error. Ansorge (2005) undertook a study to determine the minimum error that occurs by using this method and he concluded: “a trained and experienced person can hardly reduce the measurement error to less than 4 %.



Figure 2.5: Hammer, knife and cylindrical sample ring

2.5.2 Moisture Content

Moisture content is derived from the values obtained from the dry bulk density samples. Equation 2.2 was used to calculate the moisture content (dry basis).

$$MC = \left[\frac{m_{wet} - m_{dry}}{m_{dry}} \right] \times 100$$

Equation 2.2: Moisture content

where:

MC	moisture content, %
m_{wet}	wet mass, kg
m_{dry}	dry mass, kg

It was necessary to monitor the levels of moisture within the soil samples as moisture affects cohesion levels within the soil and thus directly affects the soils performance - high levels of moisture will severely reduce bearing capacity of soil, thus leading to greater compaction.

2.5.3 Rut Profile

The rut profile was measured using a profile meter (Figure 2.6). The meter is one metre long with fifty pointed steel rods. The profile meter was placed on the surface of the soil and by turning the handle indicated, the metal rods are released. These fall due to gravity and thus map the rut profile. The rods are 20 mm apart; therefore the profile obtained is a close representation of the rut. The profile meter is then removed from the soil surface and placed on a piece of paper. The shape of the profile meter is traced onto the paper, thus giving both the width at which the tyre deformed the soil surface and the depth to which it penetrated. To maintain accuracy, this process is repeated three times and the values recorded are then compared.

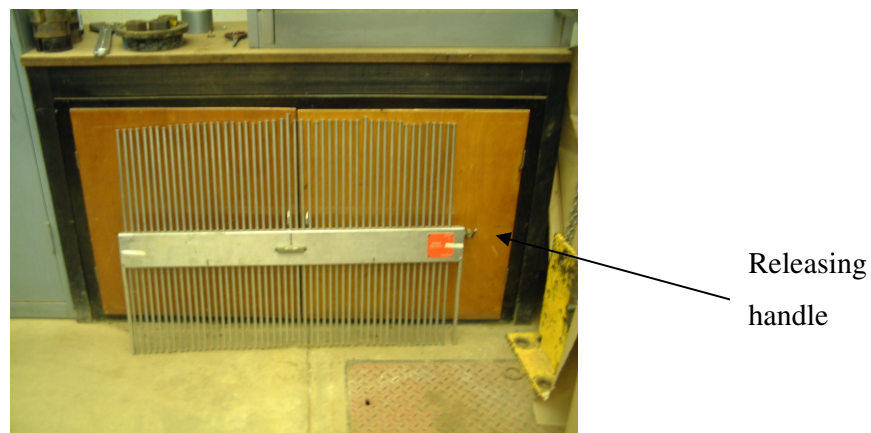


Figure 2.6: Profile meter

2.5.4 Cone Penetration Resistance

2.5.4.1 Penetrometer

Cone penetration resistance is defined as the force required to push a cone of known cross-sectional area through a soil sample. For this study the Eijkelkamp Penetrometer was used with a 125 mm² 30° cone as shown in Figure 2.7. The Eijkelkamp logs the forces at 10 mm intervals in the vertical plane through the soil profile up to a depth of 800 mm.

The measurement technique was as follows: an aluminium plate with 10 holes on a 120 mm equidistant spacing, (Figure 2.7), was placed perpendicular to the direction of travel of the tyre with holes 5 & 6 being approximately 60 mm either side of the tyre centreline. Starting from the right hand side of the plate the penetration resistance at each hole was measured by inserting the penetrometer. This process was repeated three times for each of the following scenarios, Control, 1st Pass, 2nd Pass and 3rd Pass. The data was then exported from the logger in .txt format into MS Excel for initial processing.

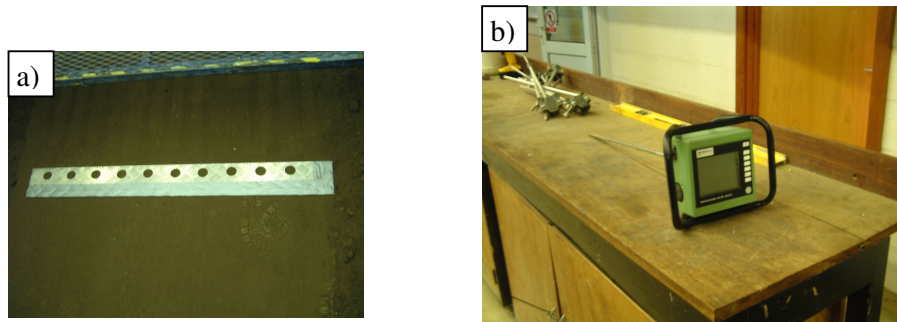


Figure 2.7: a) Sample plate and b) Cone penetrometer

2.6 Soil Deformation and Measurement

2.6.1 Soil Deformation

In the past, many methods have been used when monitoring layer deformation through a soil profile. Trein (1995) developed a method of marking each layer with a white emulsion paint; although found to be very accurate, it had two main drawbacks, excessive time consumption and variation in definition. Ansorge (2005) developed a variation of Trein's procedure using talcum powder. Talcum powder, in the required quantities, does not affect the cohesive potential of the soil and definition within the soil profile is good. Ansorge checked his adaptation of Trein's procedure by carrying out multiple tests, 3D modelling and manual card plotting and concluded that error levels of ± 1 mm are achieved when using this technique.

2.6.2 Soil Preparation for Deformation Measurement

Using the soil preparation technique, as described previously, the soil was scraped back and initial layers were placed, rolled and wetted. The first talc lines were placed on layer 2, 100 mm above the datum. Talc was not placed on layers below this point as they are influenced by edge effects from the concrete floor. In total 8 layers of talc were placed in the soil profile, with the first seven being 100 mm apart and the final layer being 50 mm above layer seven and 50 mm below upper surface. An interim layer is added to give both higher resolution of the topsoil displacement and to provide a layer close to the surface, but lacking the tread/lug indentation of the tyre.

Using the method defined by Ansorge (2005) the talc is placed on top of the wetted layer parallel to the direction of travel of the wheel (Figure 2.8). To record the result accurately, three dedicated zones were created within the soil bin, one control zone and two sample zones. When creating the talc layers within these zones a plywood rig was placed parallel to the direction of travel of the tyre and touching the left-hand wall. Each layer within the zones consisted of 14 lines of talcum powder, 6.5 ± 0.5 mm wide with an equidistant spacing of 100 mm across the width of the bin.



Figure 2.8: Talc layers in the soil profile

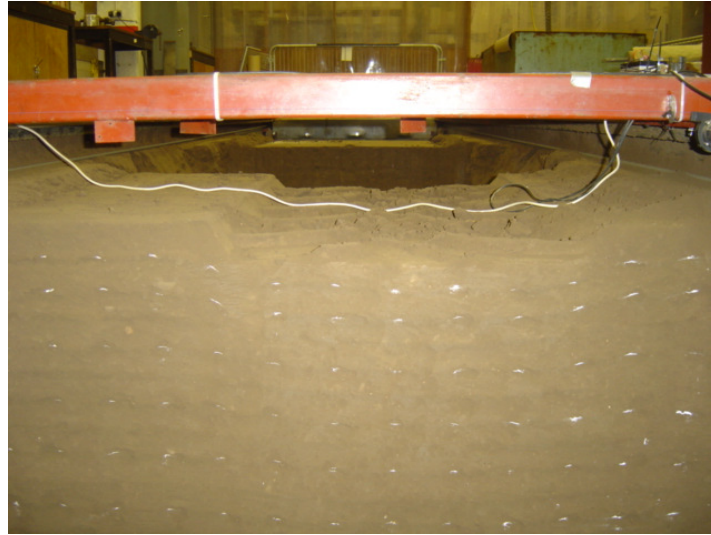


Figure 2.9: Sectioned view of the soil profile after 3rd pass

Once a test is completed, the soil profile is excavated at the start of the sample zones. As the profile is excavated white talcum powder dots become apparent as shown in Figure 2.9. The face of the soil profile is kept square at all times, maintaining the bi-planar measurement characteristics. A hand brush and knife help to locate the exact position of the talc lines as smearing can occur when profiling with a spade. Deformation is measured using a drawstring transducer rig developed by Oliver & Cathey L (2003). The drawstrings are mounted at either end of the rig and are joined together by a marking pin. The drawstrings are calibrated in both the x and y planes to an accuracy of ± 1 mm. The normal method of recording the deformation results is from left to right side of the bin, moving down through the layers once all horizontal points have been recorded on the layer. Moving the pin to a point of talc and depressing the switch gathers the reading. This is then recorded using a PMD 1208LS analogue data logger with a USB connection to a laptop computer with DaisyLab 8.0. The raw values recorded are voltages, using DaisyLab 8.0 these are converted to millimetres for both the x and y planes.

2.7 Single Wheel Tester

The single wheel tester, as shown in Figure 2.10, used in this study was designed by Ansoorge (2005) for use on tyre and track studies. The rig is mainly constructed from

box section and comprises a Claas combine gearbox, linear bearings, hydraulic ram, pressure control valve, pressure transducer and calibrated weights.

The hydraulic ram has two functions, the first is to lower the wheel assembly to the soil level and the second is to apply a vertical force on the tyre. Varying the restriction of the calibrated pressure control valve alters the force exerted and this is monitored by relating the voltage output to the calibration plot for the pressure transducer. As the rig travels along the rails of the soil bin it is not attached by any means to the rail, masses totalling 3,500 kg are placed into the boxes either side of the frame to counteract the force being exerted by the hydraulic ram (50 kN), thus maintaining the connection between the rig wheels and the rail.



Figure 2.10: Single wheel tester

The final reduction is mounted to the plate, as shown in Figure 2.11. The axle is connected through a frame to the linear bearings; the bearings are frictionless and have been used on this rig to counteract the torque and any random forces generated when accelerating the wheel from rest.

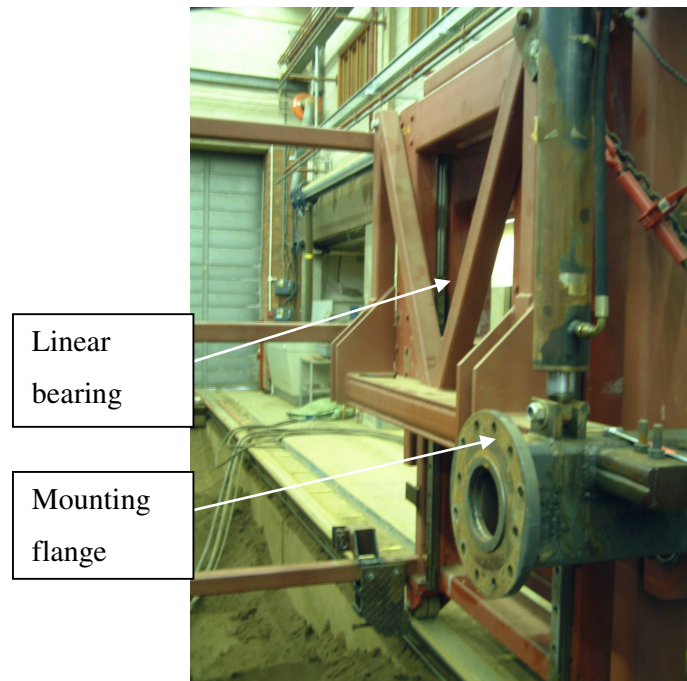


Figure 2.11: Final reduction mounting point and linear bearing track

2.7.1 Propulsion Method

Two method of propelling the tyre were used:

- Self propelled
- Towed

The splined driveshaft on the final reduction is the key component that determines the type of drive method used for testing. When carrying out self-propelled tests a driveshaft was connected from the gearbox to the splined input shaft of the final reduction, thus allowing self-drive of the tyre. Disconnecting the shaft gave a wheel, which was able to rotate freely, thus allowing the rig to be trailed by the soil processor.

2.8 Draft Force

To determine the effort required to remove compaction at a depth of 350 mm a subsoil tine (Figure 2.13) was pulled through the soil in the centreline of the tyre track. The tine was mounted on an Extended Octagonal Ring Transducer (EORT) which measured the force required to pull the tine, with the force directly relating to the soil density. The EORT was mounted to the lift frame of the soil processor and can be moved in both the x and y planes, thus allowing accurate positioning of the tine through the centre of the rut. The EORT, (full description Godwin (1975)), measured the force generated by the tine as it was pulled through the soil bin. Data acquisition was carried out by connecting a flyd and Daisylab 8.0 to the EORT. The raw data was then exported to MS Excel for initial processing.

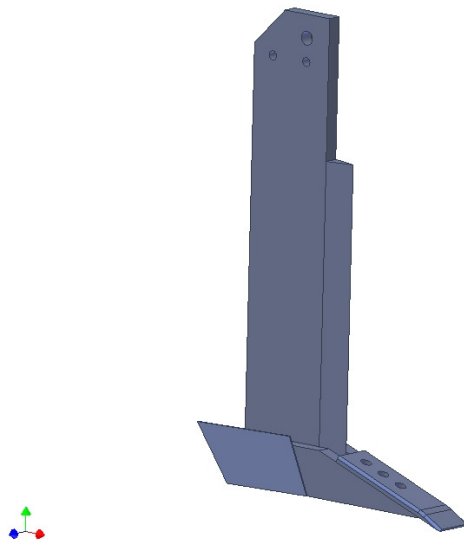


Figure 2.12: Tine used for compaction alleviation

2.9 Statistical Analysis

Statistical analysis was undertaken using Statistica 7. For each test three sample sets were taken in each zone. These samples showed consistent values, therefore the tests were considered as unpaired measurements. Due to the minimal levels of difference between each sample the tests values were then averaged and the new values used in the detailed analysis. The results were processed using a least significant difference (LSD) with a confidence interval (CI) of 95%.

3 Soil Data Processing

3.1 Penetration Resistance Processing

The penetration sampling holes span 1.2 m; therefore not all the holes are directly above the rut. Figure 3.1 shows samples 1, 2, 9 and 10 have penetration resistances with no significant difference when compared to the control readings therefore they have not been compacted.

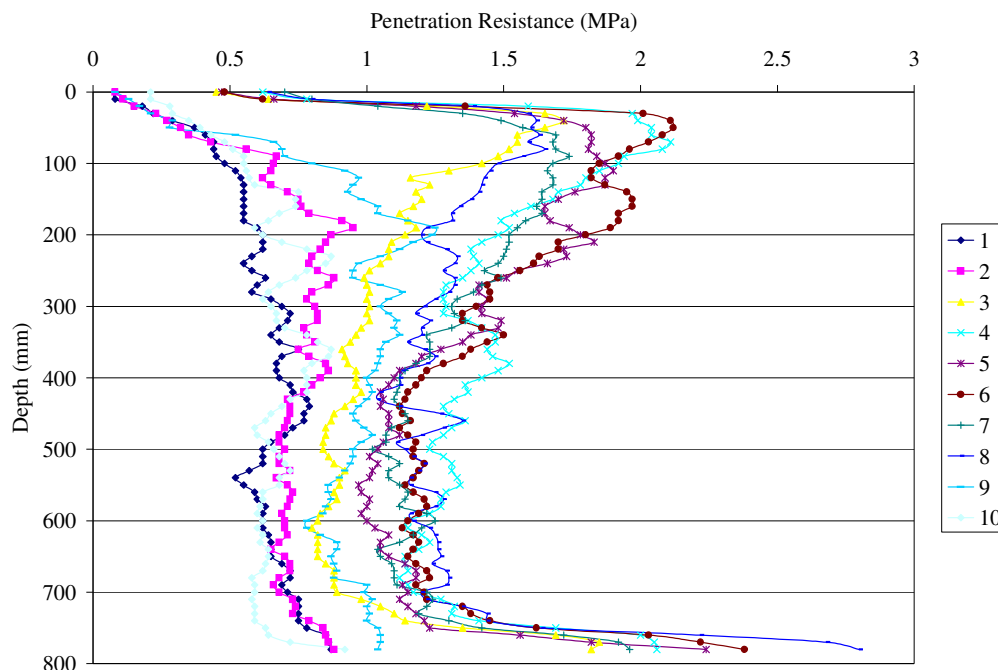


Figure 3.1: Experimental data for one of the 3rd pass measurements of the 680 loaded with 50 kN @ 1.2 bar

Further analysis of Figure 3.1 shows the resistance plots under the tyre are relatively symmetrical about the mid point of the samples, with 1 & 10 being the lowest and 5 & 6 being the highest. This is to be expected within the measurement resolution of the system and therefore in order to represent the data with a single trace the plots can be averaged by summing of the plots opposite each other about the centre point.

Figure 3.2 shows the average of the plots. The graph shows that plots 4 & 7 and 5 & 6 display the highest level of penetration resistance. These four samples are immediately adjacent to the centre of the tyre, therefore by summing these two plots and taking the average a value for the penetration resistance directly below the centreline of the tyre is retrieved.

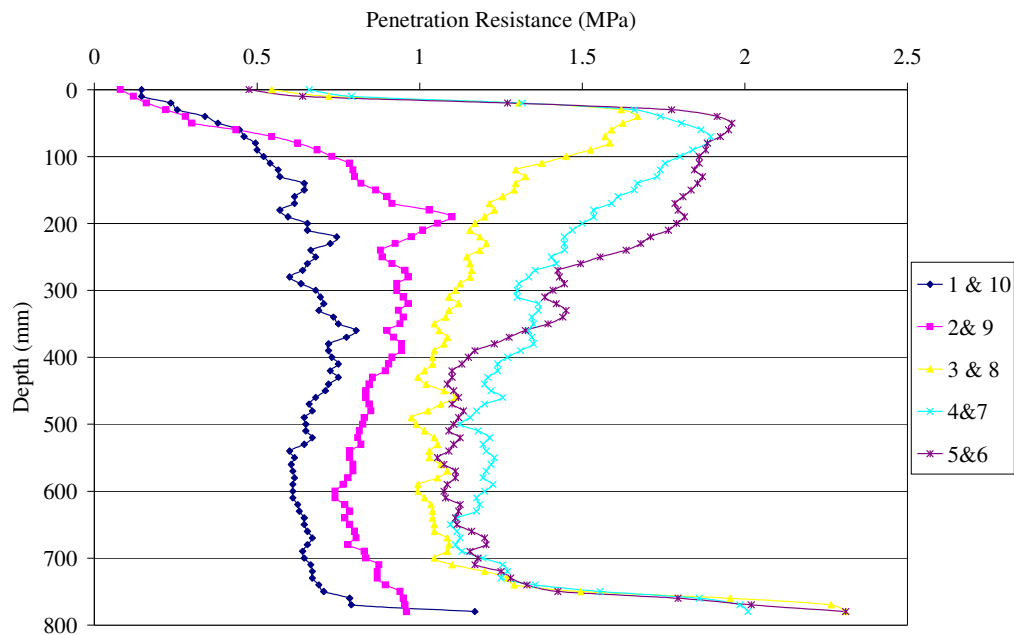


Figure 3.2: Average of left and right hand sides of bin

Figure 3.3 shows the predicted peak value of penetration resistance below the tyre through the centreline. The significant difference noted between all the results at depth ≥ 650 mm was negligible therefore below this stated depth all results will be disregarded.

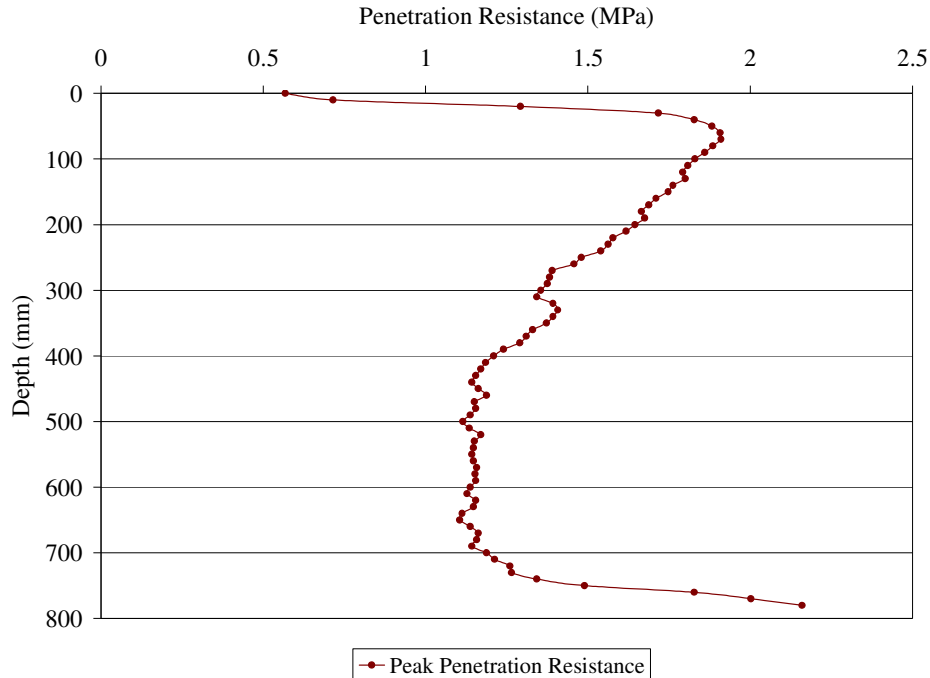


Figure 3.3: Average penetration value below tyre centreline

3.2 Resolution of Measurement Techniques

The two main measurement techniques used in the soil tests are penetration resistance and deformation measurement. Each technique has different error ranges and potential pitfalls which are governed by both the level of human interaction and scientific calibration of the test equipment

3.2.1 Penetration Resistance

The process of recording penetration resistance is fully documented in Section 2.5.4. As stated in that section, the equipment used to measure the resistance records every 10 mm, this incremental recording results in a maximum of 80 points measured per sample. As the penetrometer is pushed into the soil profile it must be subjected to a constant velocity in the vertical plane. If this varies, sample rates and thus resolution of results vary and inevitably errors between readings can be accrued. Due to this factor, it can be assumed penetrometer readings may be taken as a guide to sub-

surface conditions, however, due to the variability of human input into the measurement technique the resolution of the results are of low quality.

3.2.2 Deformation Measurement

The process of recording deformation using drawstring transducers is documented in Section 2.6. 112 results are recorded during each individual sample and as stated an error of ± 1 mm was found for this measurement technique. Deformation recording is undertaken in a “visible” manner; therefore the risk of human error distorting the measurement is negligible.

3.3 Error Analysis

The final aspect of work within the soil bin was to assess the preparation techniques and the magnitude of errors incurred during this process. Figure 3.4 shows the average error recorded when undertaking the lay-up and compaction of the layers during testing. From this study it can be seen that the layer closest to the concrete floor was continually laid and compressed $<1\%$ below its desired height. All layers above the base layer were finished fractionally higher with the upper layer having the maximum increase, 7% . A possible reason for this is the position of the blade height marker and the marker detail. The marker is at a declination angle from the seated processor operator and the marks on the blade are approximately 5 mm high, therefore each layer could be as much as ± 5 mm out of position. Another possible reason is variation of the pressure exerted by the roller due to thermal changes in the hydraulic circuits. The layer errors found were consistent for all tests undertaken in the soil bin at CU@S, therefore, the discrepancies pose no problem to the results recorded from the PMC tests.

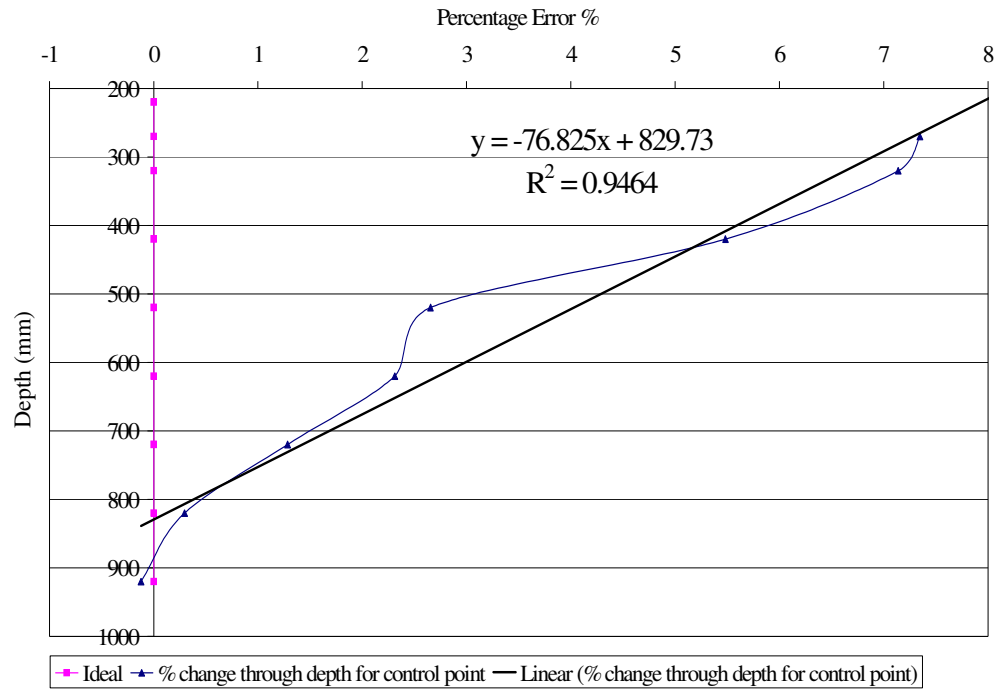


Figure 3.4: Layer displacement change through bin section

4 Literature Review

4.1 Soil

Soil is defined as: “The unconsolidated mineral or organic material on the immediate surface of the earth that serves as a natural medium for the growth of land plants” (Soil Science Society of America).

The roots of plants can establish a good “footing” in soil, and are supplied with an abundance of vital nutrients and oxygen, provided the soil has sufficient cohesion to supply support for development, whilst also being largely unconsolidated, to allow unrestricted root passage. However, this low level of consolidation means soil, in most cases, does not possess the required properties to support locomotion of heavy vehicles without damaging its growing potential, Håkansson & Reeder, (1994). This leads to a major problem within crop production, as the mechanical methods used to sow, tend and harvest crops depend upon weighty vehicles.

The common terminology used to describe this damage is soil compaction. There are many different definitions for compaction, which vary to suit the specific viewpoint the writer had in mind. For this specific application, the most suitable definition was defined by Carmen (2002); he stated, “Soil compaction is a volumetric strain or the packing of soil particles to a dense state as a result of an applied load”. Further differentiating this statement, it can be said that compaction directly affects the original pore volume and structure by reducing the pore space, thus reducing the permeability of water and nutrients through the soil strata and inevitably reducing the soil’s potential ability to support growth.

In essence, soil compaction only occurs when a pressure is applied to the soil that exceeds the bearing capacity of the soil. The capacity is dependent on many different variables, including soil type, moisture content, particle cohesion and initial level of consolidation; all of which may be subject to vast local variations. Söhne (1958) found that if the moisture content of soil was increased by 11.6% then the pressure required to compact it to 42% porosity would be reduced from 19 bar to 3.25 bar, thus

demonstrating that increasing the soil moisture content has a negative effect on the load bearing capacity of the medium. Blackwell (1978) carried out a study that showed when soil water content was 23 % (w/w) the increase in bulk density at a depth of 150 mm was four times larger than when the water content was 14 % (w/w), under the same loading. This increase in bulk density occurred as a result of the reduction in bearing capacity caused by the increase in soil moisture level, therefore causing an increase in compaction.

When soil compaction occurs a definitive increase in dry bulk density will be noted due to the consolidation of the soil particles. Dry bulk density has a direct relationship to both the mean normal and mean shear stresses, as shown by Van den Berg (1966). Topsoil and upper subsoil compaction is not irreversible; it can be eradicated in the short term by mechanical loosening or possibly in the long term by nature itself through freeze/thaw or wetting and drying cycles, however this method has not been firmly accepted. Hedberg (1976) carried out intensive tests within laboratory conditions to mimic the natural phenomena of freeze/thaw; he concluded that it took many sequential cycles to bring the compacted soil into a new loosened equilibrium state; therefore showing that alleviation was possible through nature. This work was contradicted by Bake et al, (1976) who found no alleviation of subsoil compaction over a 9 year period in soils with clay content ranging from 6 to 85%, in spite of annual freezing to approximately 1 m; this work confirmed the earlier findings of Van Ouwerkerk (1968), suggesting that mechanical rectification of upper soil layers is the only effective option post severe consolidation. Deep subsoil compaction is much harder to rectify, Håkansson and Reeder (1994) reported that at an axle load of greater than 10 Mg compaction could be measured at a depth of 1 m; at this depth standard mechanical methods are unable to remove the compaction, therefore a persistent and possibly permanent reduction in crop yields may result.

4.2 Compaction Under Tyres

For wheeled harvesters and prime movers, the tyre is normally the first point of contact between the machine and the soil. At the tyre-soil interface, forces such as thrust and vertical load will be exerted on the tyre by the machine and then transferred

to the surface of the land through the tyres contact patch. The contact patch characteristics are defined by four main factors: tyre geometry, tyre construction, inflation pressure and the applied torque/resulting slip.

4.2.1 Tyre Geometry

The load carrying capability of a tyre is directly related to the size of the tyre. If the construction method and carcass stiffness of a tyre are kept constant and the diameter or section width increased, the contact patch will increase and thus bearing capacity increases, to an upper limit. As a direct result of these increases the inflation pressure can be reduced to its lowest viable load/inflation pressure limit for the carcass, this reduction will decrease the contact pressure and subsequently the compaction. However, as the section width of the tyre is increased so is the rolling resistance, this can have detrimental consequences in relation to both tractive ability and the amount of surface compaction. Tractive ability will decrease and surface compaction will increase on low strength soils due to an increased width of soil disturbance.

4.2.2 Tyre Construction

Tyre construction plays a major role in load transfer to the operating medium. The construction method of a tyre affects its deflection properties. These affects are non-linear due to the materials and components which are combined in making a standard pneumatic tyre and thus are not easily predicted. The two types of construction are radial and cross-ply. A radial tyre is constructed with belts of steel in the tangential direction, a cross ply has the belts laid in a bias format normally placed at +60° and -60° angles to the direction of rotation. When a cross ply tyre is subjected to a vertical load the sidewall flex is transferred to the crown of the tyre which causes inward deflections of the crown. This deflection reduces the contact patch of the tyre, as the load is unevenly distributed across the contact patch, Michelin Ag (2007). Large load concentrations form at the outer edges of the contact patch, thus the load is concentrated into a smaller area, therefore increasing contact pressure and subsequent compaction. Radial tyres however have an independent crown, therefore sidewall

flex is not directly transmitted to the crown and contact area is increased when load is applied, this was proven by Knight and King (1962) who stated, “As a [general] rule cross-ply tyres show inward deflections only, whereas a radial tyre shows outward deformation”, as shown in Figure 4.1. Steiner (1979) found the outward deformations of a radial tyre also act over a much greater area of the tyre, approximately 75% of the rotation angle, this work also concluded that a towed cross-ply tyre has half a circumference free from relative displacement giving reduced carcass flex and therefore a lower contact patch increase potential. This work concurs with that done by Michelin Ag (2007) that found, under a known load, a radial tyre can be up to 40% smaller in section width compared to its cross ply counterpart without a reduction in total effective contact area.

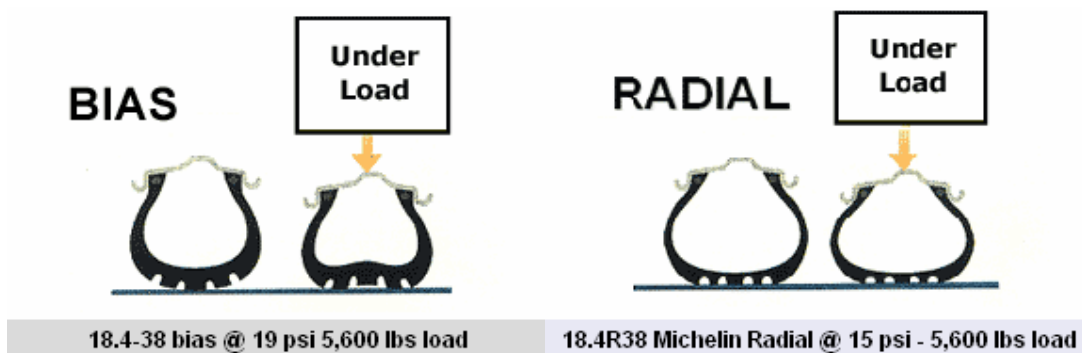


Figure 4.1: Comparison of radial and cross ply tyres under load

4.2.3 Lug Effect

The magnitude of tread void on a tyre governs the peak contact pressure directly below the tyre. As the lugs offer the first point of contact between the tyre and the soil a tyre with long thin lugs will have greater peak pressure concentrations below the lugs than a tyre with shallow, wide lugs. Carmen (2002) found that “Spreading the applied load over greater lug area and less lug height, reduced soil contact peak pressure”. From these findings it can be assumed that a tyre with a plain/smooth profile would offer the optimal reduction in peak contact pressure, however a tyre with such a profile will have limited tractive potential and thus will be inappropriate for high draft operations.

4.2.4 Inflation Pressure

Van den Berg (1966) found that inflation pressure directly influenced the topsoil compaction; however pressure variation had no effect on subsoil compaction. This was further corroborated by Smith & Dickson (1990) who found a significant increase in soil compaction near the soil surface for increased inflation pressure and a reduction in topsoil compaction when inflation pressure was reduced. Olsen (1994) reviewed the interaction of a tyre and soil with respect to subsoil stresses and stress profiles and from this concluded that the contact volume below a tyre could be split into three zones:

An upper zone where the vertical stresses are nearly the same as the ground contact pressure. An intermediate zone where stresses decrease at a high rate, dependent upon both ground contact pressure and wheel load. A lower zone where stresses decrease very slowly with depth and depend almost exclusively on the wheel load.

From these three zones it can be concluded that compaction in the upper layers of the soil is dependent on tyre inflation pressure and contact area, with axle load governing the compaction levels in the deeper layers.

4.2.5 Vertical Load

Utilising the findings of the effects of inflation pressure in Section 4.2.4 it can be assumed that vertical load affects the deeper layers in the soil profile with regards to soil compaction. Håkansson & Reeder (1994) defined high axle loads to be of the magnitude of 10 Mg and greater, and concluded from their study that subsoil compaction with this level of load could be detected at a depth of up to 500 mm, with greater loads giving compaction to a depth of 1 m; these findings were a result of collaboration of work carried out by the International Soil and Tillage Research Organisation working group on 25 different sites in several different countries using high axle load vehicles. Smith & Dickson (1990) noted that increasing the axle load increased the level of compaction at depth in the soil profile; Olsen (1994) also confirmed these findings with his soil model.

4.3 Tyre Configuration

Tyre configuration is governed by many factors including government legislation, physical constraints, tractive potential and mobility. With high axle load vehicles tyre configuration is critical, as it is one of the major factors in determining the level of compaction occurring below the soil surface. Several studies have reviewed the effects of using single wheels, dual wheels and tandem wheels. From these it has been widely accepted that dual wheels cause less compaction than single wheels when operating under the same vertical load and inflation pressure criteria. This occurs as the load is spread over a greater surface area and stress is uniformly distributed below the wheels. Danfors (1974) reviewed the levels of detrimental compaction caused by a single wheel and tandem wheels and concluded “In layers deeper than 400 mm, plastic deformations were observed to persist after passage of the vehicles when the load on a single axle was 6 Mg or more and on a tandem axle was 8 Mg or more”. The soil type was mainly clay and clay loams; the tyres sizes were kept constant, as were inflation pressures.

The advantage gained using tandem wheels over the other two options was investigated by Håkansson & Reeder (1994), following their study they stated: “Tandem wheels are more effective than dual wheels in reducing compaction”. This is due to the wider spacing involved in the tandem axle, as the spacing between wheels governs the quantity of stress interaction between them. The load application in a tandem axle configuration is in series therefore there is potential for the 2nd wheel to accentuate the stress generated by the 1st wheel, rather than acting solely on the permanent deformation created by the passage of the 1st wheel. This is governed by the recovery rate of the medium and time between applications. Trein (1995) also concluded that using a tandem axle configuration reduced deformation through the soil profile by 27%, in these tests he maintained wheel size, inflation pressure and soil conditions.

4.4 Tracks

Tracks have been used within heavy industry and agriculture for many years; the first commercially produced diesel fuelled crawler was designed and manufactured by Caterpillar in 1931. This machine used steel tracks to provide locomotion. Tracks are normally fitted to machines if they require low ground pressure or high tractive potential in unfavourable conditions. There are two common types of tracks; steel tracks and rubber belts, each with their own unique characteristics.

4.4.1 Steel track

Advantages:

- High tractive ability,
- Relatively uniform load distribution governed by segment size and number of idlers.

Disadvantages:

- Low speed,
- The track does not readily flex, consequently it does not mould to the terrain,
- No suspension, resulting in high vibration transfer and an uncomfortable ride for operators,
- Not suitable for use on the public highway.

4.4.2 Rubber Tracks

Advantages:

- Offers an improved medium to absorb vibrations,
- Track can be both flexible and extendable, which offers the potential to “mould” to the surface depending on number of idlers,
- A rubber-tracked vehicle can travel at higher speeds and can be used on the public highway.

Disadvantages:

- Stress distribution below the track is not uniform because of rigid road wheels fitted as idlers,
- A marginal loss in tractive potential will be noted, when compared to a steel track, due to belt tension and flex of segments, Ansorge (2006),
- The drive belts are not as tight and thus “rip” off more easily when turning at speed.

Since the early 1990's rubber tracks have been a topic of much research and development by the major manufacturers. Erbach (1994) stated, “Tracks are beneficial compared to wheels”, however he did not feel these findings would apply in all situations a track may be used in and concluded the following:

- Sequential application of shear stress under tyres offers lower total shear stress when compared to that observed with the required equivalent length of track.
- Tracks can suffer from poor pressure distribution leading to high-pressure concentrations.
- High levels of vibration transfer between the machine and ground occur with tracks.

4.4.3 Track vs. Tyre Performance Comparison

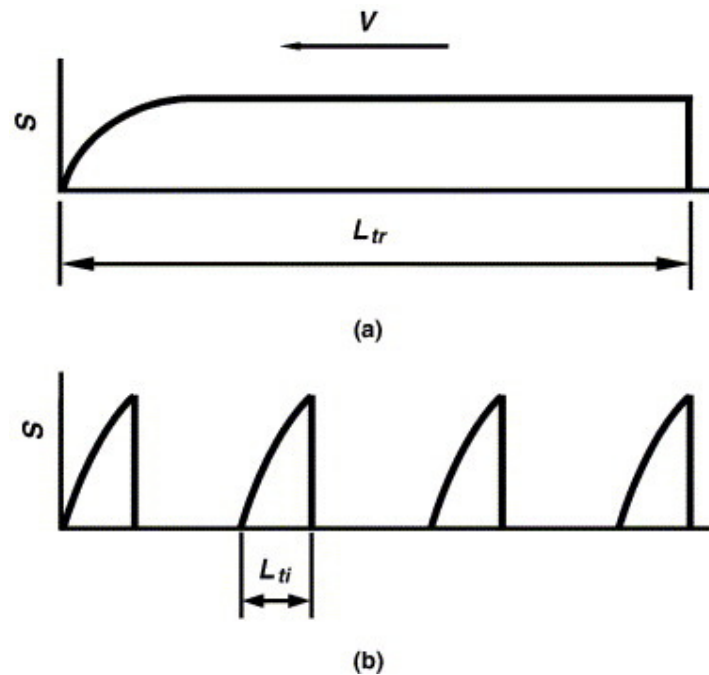


Figure 4.2: Shear stress generated by (a) single track vs. (b) four tyre counterpart. (Wong 2004)
 S – Shear stress, L_{tr} – Track contact length, L_{ti} – Tyre contact length, V – Velocity

For a given track and tyre, with equal section widths and equivalent track contact length and tyre wheelbase, the track will have a much greater thrust potential than the tyre counterpart. Wong and Huang (2004) stated; “Thrust potential is the integration of shear stress over the contact area.” The wheeled vehicle has a much shorter active contact length therefore it cannot maintain the same levels of thrust. During Wong’s investigation he noted that the wheeled vehicle developed 50.4% of the tracked vehicles thrust. Figure 4.2 demonstrates that the four tyres apply their thrust in series. Using Figure 4.2 to analyse the tractive performance of the two undercarriages it can be concluded that if a wheeled vehicle was to traverse a short saturated section of soil then the tractive potential is governed by the wheel spacing. However the track applies an equal amount of thrust along its total length therefore potentially out performing the tyre alternative.

4.5 The Overall Effects of Soil Compaction for the Grower

4.5.1 Growth Potential Consequences of Soil Compaction

The most important factor in soil compaction is hydraulic conductivity changes resulting in variation of soil water potential. “The change in hydraulic conductivity affects the infiltration, evaporation, redistribution, capillary rise and downward flow of water”, Boone et al, (1986). As water contains the oxygen necessary for plant growth, any reduction in the passage potential of water through the soil profile directly affects plant growth. Boone et al, (1987) found that as soil compaction increased both the duration and the severity of oxygen stress increased for plants. He also reported that run-off and evapotranspiration increased when compaction was increased which was attributed to the “sealed” surface generated by the compaction.

4.5.2 Rectification and Financial Costs

At 2006 fuel prices, rectification costs were expected to be as high as £4 per hectare depending on method and quality of job, Ansorge (2006). This does not include man hours, machinery depreciation or associated costs. The typical method of soil loosening is to pull a tine, or similar implement, through the soil. Problems can occur during rectification, Ehlers et al (1994) found that “ploughing caused rapid reconsolidation of the subsoil, which had been previously ameliorated by strip loosening”, therefore, after initial loosening, care should be taken not to cause reconsolidation of the subsoil; practises such as on-land ploughing reduce this risk.

Compaction can have a long term financial impact, Gameda et al, (1987) showed that in Canada persistence of increased bulk density caused by traffic with an axle load of 12 t was still detected six years after initial traffic, therefore giving a tangible reduction in crop productivity and inevitably profits.

4.6 Key Areas of Influence

Summarising section 4 it can be concluded that for the PMC application the following areas are relevant:

- Tyre configuration - Determine whether the second wheel amplifies the first wheel compaction, due to the soil being in “recovery” from the plastic deformation caused by the first pass. If the subsequent wheel passage magnified compaction, it could be hypothesised that following initial loading there is recovery of the soil to a new settled displacement - less than the peak displacement - in a time governed process.
- Tyre performance with reference to construction method, geometry, lug geometry
- Vertical load variance
- Inflation pressure variance within one tyre under fixed load
- Drive method
- Utilisation of tracks in a hybrid track/tyre configuration
- Cost of rectification to compacted land.

5 Results and Discussions

5.1 Triaxial Testing

Examining the hypothesis generated in Section 4.6 a triaxial test series was developed to review the potential of 2nd wheel interaction. During testing the following procedure was employed. A soil sample was created inside a cylindrical membrane and then placed inside the triaxial test equipment. The soil sample was loaded vertically by means of an axial load to a magnitude of 50 kN with a time interval between each load application of 1.3 seconds. The soil which was tested was taken from the test bin and prepared to a DBD of 1.37 g/cm³

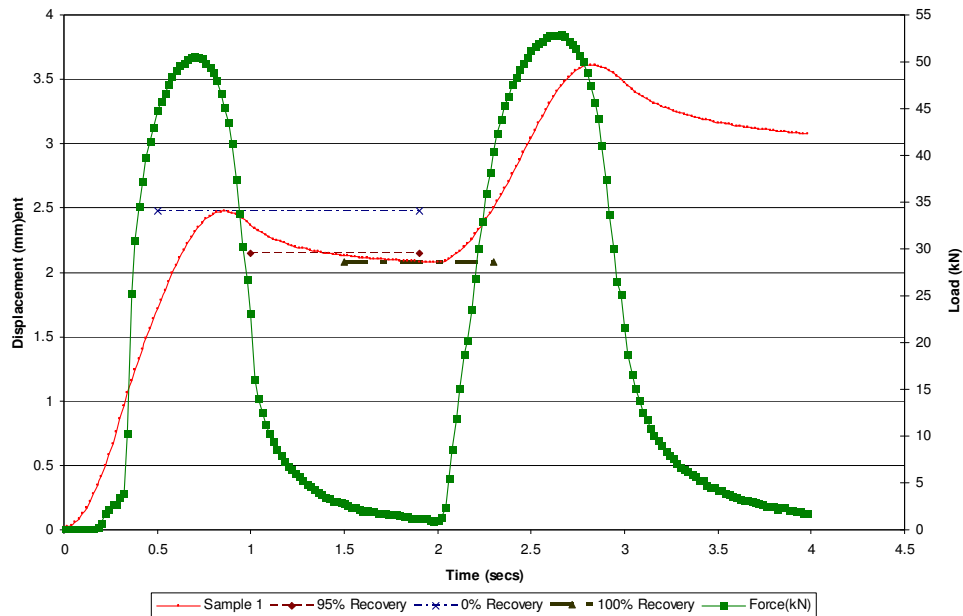


Figure 5.1: Displacement vs. Time, triaxial test result

Table 5.1 shows the average of the results recorded from the triaxial tests. These results demonstrate that the compacted soil had recovered to 95% of the peak deflection 0.54 seconds after load application. The soil then took a further 0.59 seconds to fully recover. The normal time period between wheel load applications for the 979 CT in harvesting conditions travelling at 4 km/hr is 1.3 seconds, therefore the second wheel of the tandem axle does not alter the peak soil displacement due to the

first wheel. Thus, from the triaxial study, it may be concluded that using a single wheel test rig is appropriate for the PMC tyre tests.

Table 5.1: Triaxial test results

Recovery (%)	Time (secs)
95	0.54
100	1.13

In order to affirm these findings multiple tests with a range of interval durations were performed. The findings from these tests corresponded with the results given in Table 5.1.

5.2 Contact Patch

Contact patch geometry is directly related to the following physical properties: tyre diameter, tyre width, carcass stiffness, inflation pressure and vertical load. Table 5.2 shows the contact patch characteristics of the three tyres on test. The measurements are the total contact area including lugs and were undertaken in the soil dynamics facility using soil with a DBD of 1.37g/cm^3 .

Table 5.2: Contact patch geometry of the tyres

Tyre	Inflation Pressure (bar)	Load (kN)	Max. Width (m)	Max. Length (m)	Contact Area (m ²)
Michelin 750	1.6	50	0.73	0.91	0.51
Trelleborg 425	1.6	50	0.62	0.53	0.30
Trelleborg Twin Radial	1.2	50	0.68	0.90	0.50
Trelleborg Twin Radial	1.2	45	0.665	0.77	0.43
Trelleborg Twin Radial	1.2	40	0.665	0.645	0.37

The Michelin 750 tyre was the largest diameter and section width tyre on test and subsequently generated the largest values in all three aspects. The Trelleborg 425 is a

cross-ply tyre, this construction method means the tyre will not readily deflect under load and will produce a relatively small contact patch, as shown in Table 5.2. Reviewing the findings for the Trelleborg Twin Radial in Table 5.2 it can be noted that when the inflation pressure is 1.2 bar and the vertical load is increased the contact patch length is increased. The lateral geometric increase is negligible which is typical of a radial construction tyre.

5.3 Study 1 – Compaction Comparison of the Three Chosen Tyres.

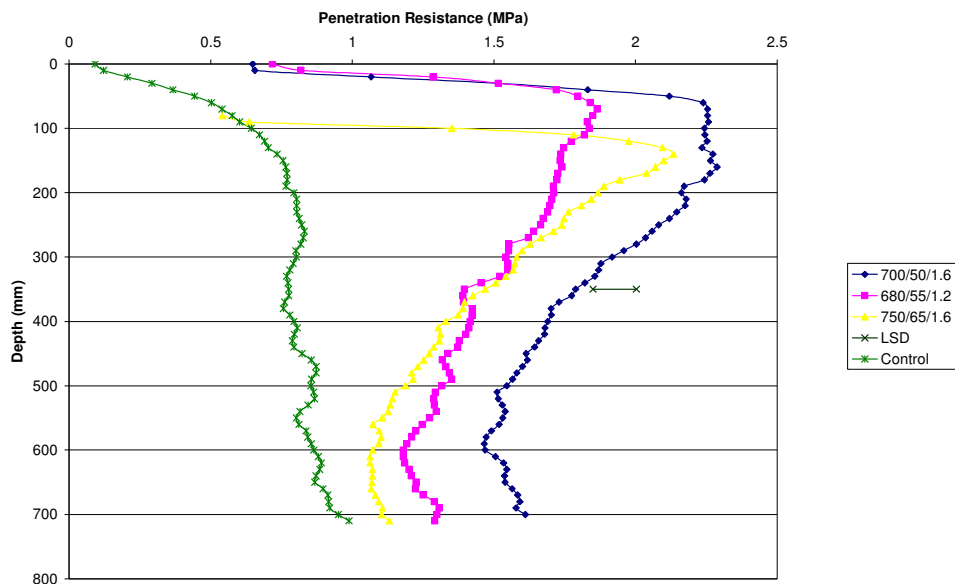


Figure 5.2: Penetration resistance vs. Depth for the three proposed tyre solutions

Figure 5.2 shows the average penetration resistance of the soil for the three tyres after the three pass test sequence. The graph shows the 700 tyre not only creates the highest peak penetration resistance of 2.45 MPa, but also the highest levels of resistance throughout the soil profile. The 750 tyre generates a peak penetration resistance of 2.2 MPa occurring at 150 mm depth; however the rate of decline of

penetration resistance is fast and at 400 mm depth a value of 1.43 MPa was observed. The 680 tyre causes the lowest peak penetration resistance, 1.78 MPa, occurring at a depth of 75 mm, and a shallow rate of decline resulting in a value of 1.47 MPa at 400 mm depth.

The performance of the 700 tyre was the poorest of the three tyres; the primary reason for this is expected to be directly related to its contact patch and reduced deflection as shown in Section 5.2. The rut profile showed deflection at the centre of the wheel was approximately 10 mm less than the deflection at the outside of the tyre, this confirms the finding of Knight and King (1962) that cross ply tyres show inward deflections at the centre of the crown when subjected to high axle loads. Considering the contact patch issues with the higher field inflation pressure meant the tyre deflected less, had a smaller effective contact patch and therefore caused the most compaction.

The 750 tyre has an aggressive chevron pattern (tractor pattern), with long, tall, narrow lugs which should aid traction in wet conditions, however with respect to the effects of lug contact area in the soil, these lugs generate higher peak pressure concentrations directly below the lug, giving rise to higher levels of penetration resistance at the soil surface. The topsoil compaction would be further magnified if the 750 tyre was operated at road pressure in field conditions.

The 680 tyre has shallow, wide lugs arranged in a chevron pattern with a centre bar around the middle of the tyre. The results from deformation tests show that the contact pressure and penetration resistance generated by the 680 is the lowest; this can be attributed to both the low operating inflation pressure – 1.2 bar and a good lug/void ratio.

The deformations versus depth results are shown in Figure 5.3; these concur with the penetration resistance findings. Again the 700 tyre caused the most deformation throughout the 800 mm deep soil bin. The results for the 680 tyre and 750 tyre show that the difference between the two tyres lie within the LSD for this plot, therefore indicating that statistically the difference between these two tyres is minimal.

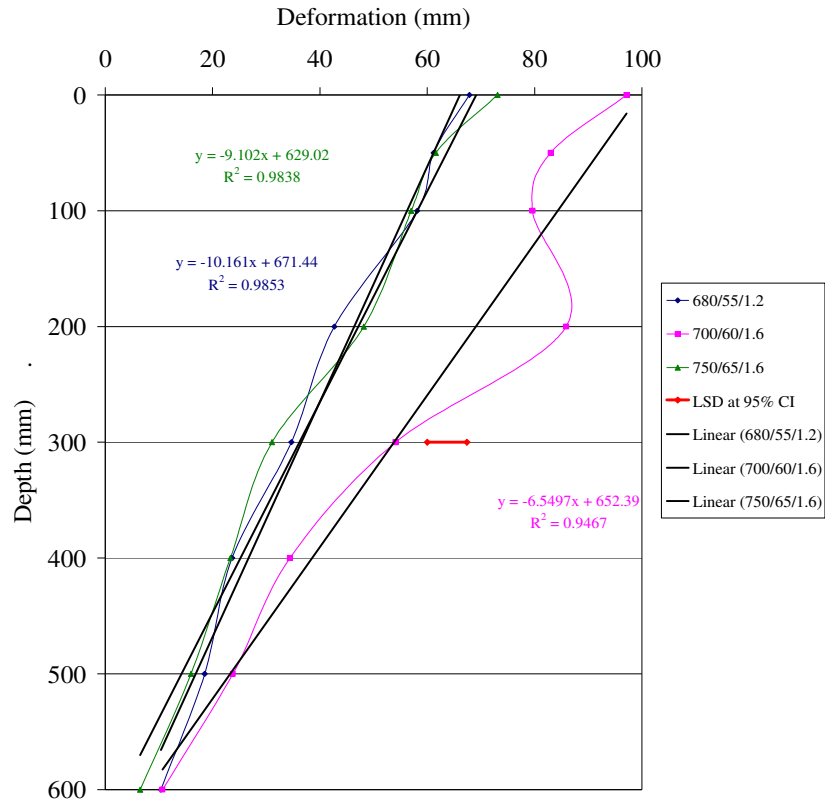


Figure 5.3: Deformation vs. Depth for three proposed tyre solutions

5.3.1 Further Analysis of the Three Tyre Options

Figure 5.4 shows a deformation plot of the three tyres at key depths in the soil profile. These depths have been chosen as they offer information on the three key areas of the wheels compaction. The upper plot shows results directly below the surface of the soil. It shows the type of visual deformation that the operator will see after traversing the soil. The middle plot is at normal plough depth and shows the amount of deformation which will be removed after ploughing, the lowest plot is below all normal subsoiling processes and represents the level of irreversible deformation which cannot be reached. Studying the upper two plots it can be concluded that the tyre which causes the least deformation is the Trelleborg Twin Radial inflated at 1.2 bar, this is closely followed by the Michelin at 1.6 bar with the Trelleborg 425 at 1.6 bar coming last. From the lower plot, it is apparent that the differences in tyre geometry and inflation have no bearing on the deformation, therefore it could be surmised that deformation at this depth is now solely due to the axle load.

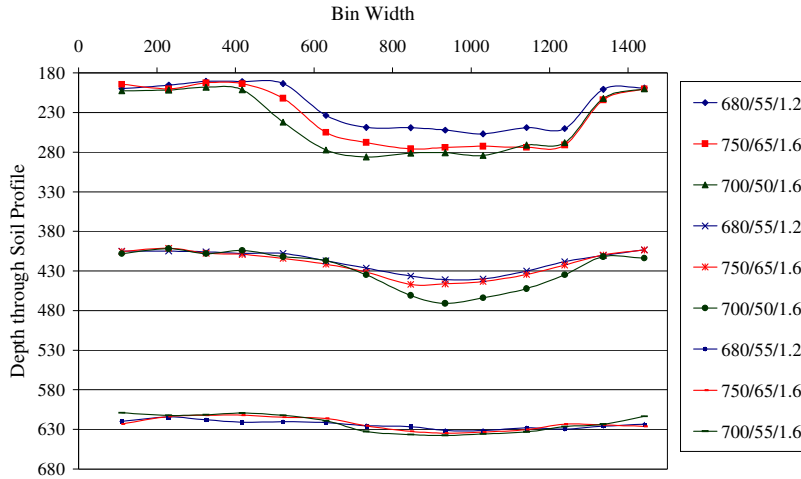


Figure 5.4: Plot of deformation at key layer depths

Following analysis of the results from Study 1 it was decided the Trelleborg Twin Radial tyre would be used for all further studies. The Michelin Mega Xbib produced results similar to the Trelleborg Twin Radial

5.4 Study 2 – Effect of Wheel Load on Penetration Resistance

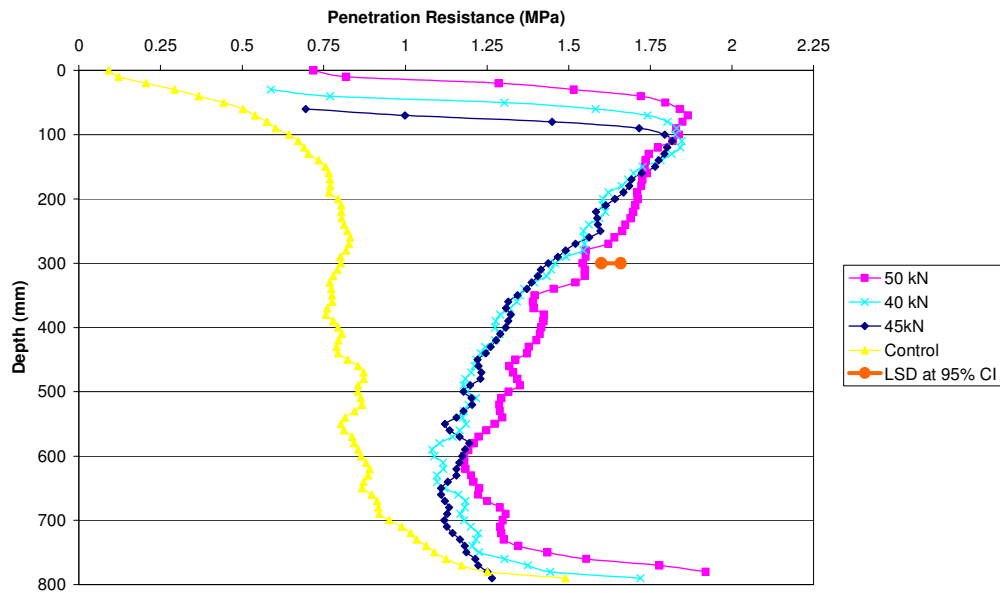


Figure 5.5: Penetration resistance vs. Depth for three axle loads

The penetration resistance results, (Figure 5.5), do not show a vast distinction between the vertical loads. The 50 kN load generated the highest peak and highest continual penetration resistance through the soil profile. The difference between the 45 kN and 40 kN graphs is less clear, the 45 kN appears to have a marginally lower peak value, however as depth through the soil profile increases, on average, the 45 kN reading is higher. The factors mentioned in Section 3.1.1 help to explain this discrepancy. Penetration resistance is a low resolution measurement technique which in this case, where the incremental load changes are relatively small (< 10%) means that the findings are unclear.

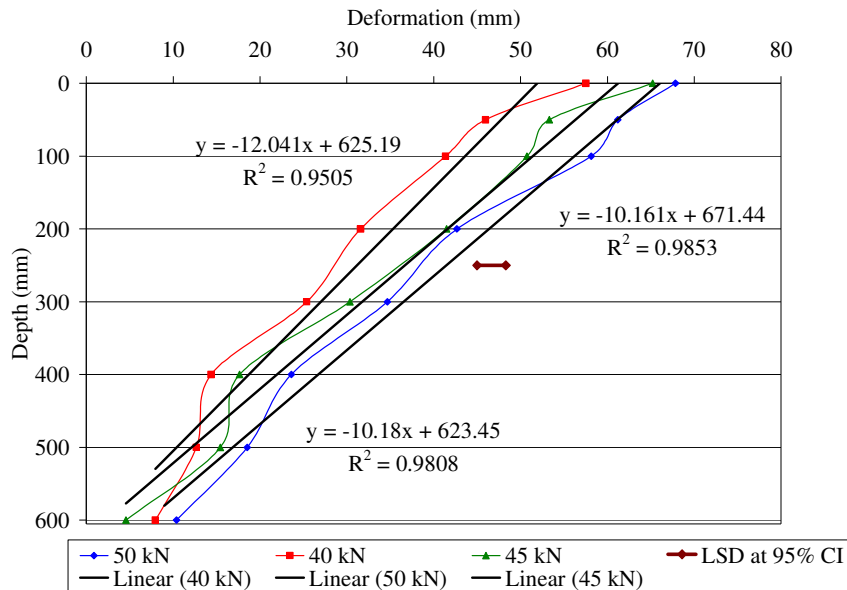


Figure 5.6: Deformation vs. Depth for three axle loads

In contrast to Figure 5.5, Figure 5.6 clearly shows the difference between the three loading scenarios. The lowest load (40 kN) gave the lowest deformation through the soil profile, similarly the highest load (50 kN) gave the highest level of deformation. The three plots will converge to zero deformation at depth in the soil profile. The convergence to zero will occur at great depth in the profile and will not take a true linear profile. The findings from Study 2 concur with the work done by Olsen (1994), in which he concluded that wheel load almost exclusively effects the subsoil deformation with the rate of stress regression being slow.

The resolution superiority of the deformation measurement technique is clearly seen in this study, the penetrometer showed little change with wheel load variation,

whereas with the deformation it can be concluded that at 300 mm depth in the soil profile a 26.8% reduction can be achieved if 10 kN were to be removed from each wheel.

5.5 Study 3 – Comparison of Transition Methods

Figure 5.7 shows that the towed wheel causes a higher peak resistance at topsoil level when compared to its driven counterpart. Beneath a depth of 75 mm both traces closely mirror one another, with the only significant difference occurring between 220 – 320 mm.

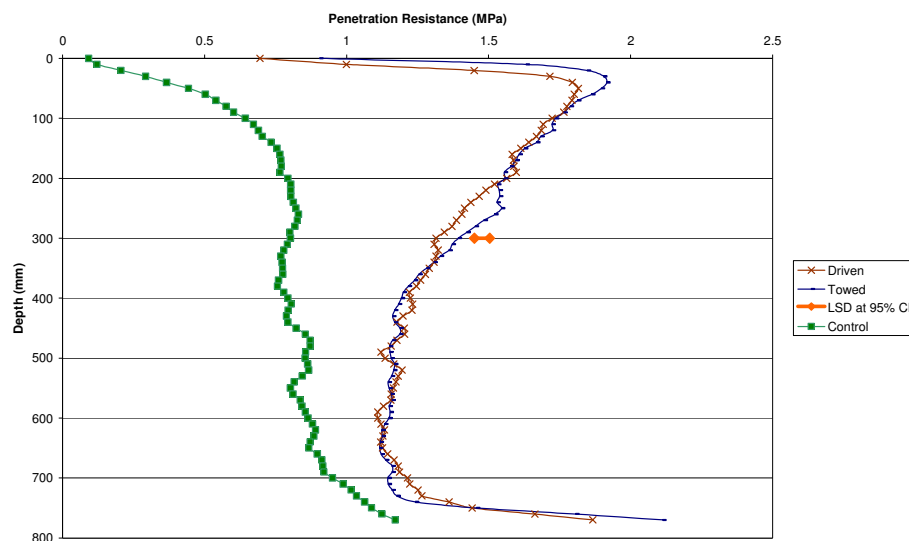


Figure 5.7: Penetration resistance vs. Depth for driven and towed wheels

Figure 5.8 shows a different scenario. Both plots mirror each other and, unlike Figure 5.7, a clear distinction can be made between the two transition methods, albeit deformation on occasions is minimal. Each propulsion method offers unique characteristics; the driven tyre is subjected to a positive driving torque whereas the towed tyre is subjected to negative wheel slip/skid and will “bull doze” its way along the soil bin. When a driving torque is applied to the tyre it produces a contact patch with the centre of pressure in front of the tyre centreline therefore it tends to climb the soil face. When this occurs the soil particles beneath the tyre shear, this shearing

causes a heightened level of deformation in the topsoil and consolidation of the pore space below. Quantifying the difference between the two methods we see that at 300 mm depth the driven tyre causes 21.3% more compaction to the soil profile. Therefore tests carried out for self propelled vehicles using towed wheels will underestimate the true level of compaction generated.

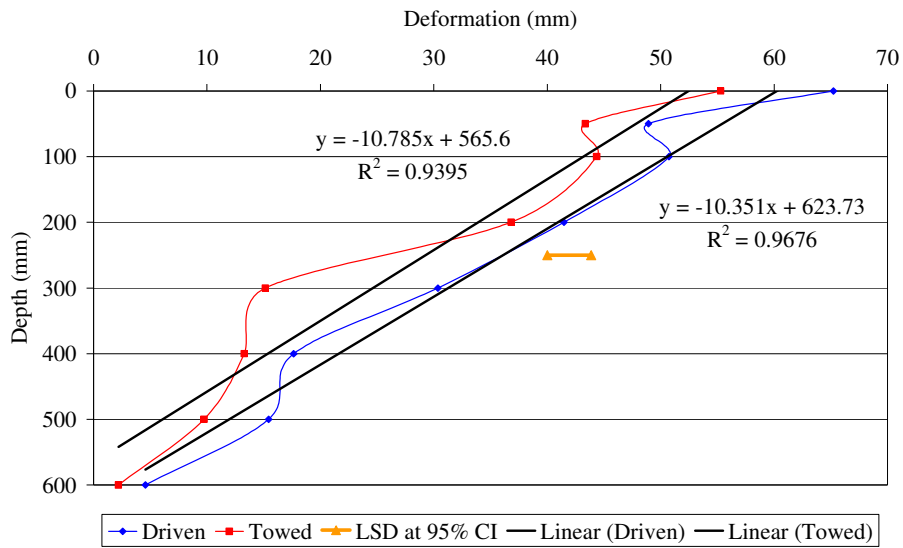


Figure 5.8: Deformation vs. Depth for Driven and Towed wheels

5.6 Study 4 – Comparison between Operating Pressures

Figure 5.9 shows the penetration resistance results for two inflation pressures of the Trelleborg Twin Radial, one at the minimum recommended field (1.2 bar) pressure and another at road (1.6 bar) pressure. The recorded penetration resistance shows that when the tyre was inflated at 1.6 bar it produced increased penetration readings through the upper 300 mm of the soil profile with the difference thereafter falling within LSD for the plot.

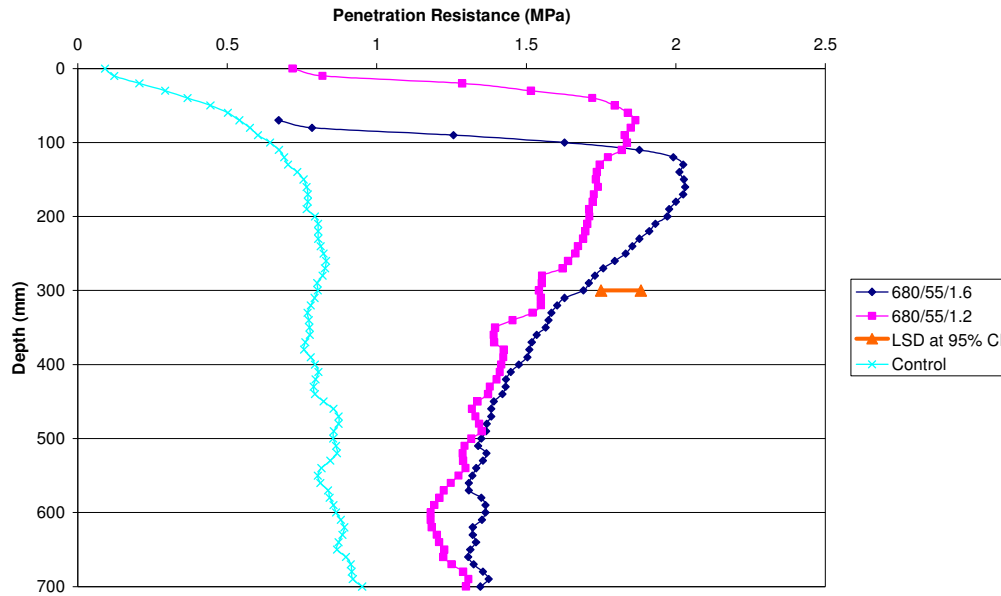


Figure 5.9: Penetration resistance vs. Depth for two different operating pressures

Reviewing Figure 5.10 it can be seen that initially the tyre at 1.6 bar inflation pressure causes more deformation in the topsoil; however as depth increases deformation tends towards the same levels of deformation found with the tyre inflated for field conditions (1.2 bar). Below 250 mm the plots are within LSD and therefore variability can be disregarded. These results suggest that for a given axle load inflation pressure defines topsoil damage. This theory was first stated by Sohne (1958) and further supported by Smith and Dickson (1990). Normal plough depth is approximately 250 mm, therefore it could be assumed for the PMC application that to use the Trelleborg Twin Radial inflated at road pressures in field conditions will cause only cosmetic damage to the field and not magnify deep soil compaction. The actual increase in topsoil compaction is 12.6% when the tyre inflation pressure is increased by 0.4 bar.

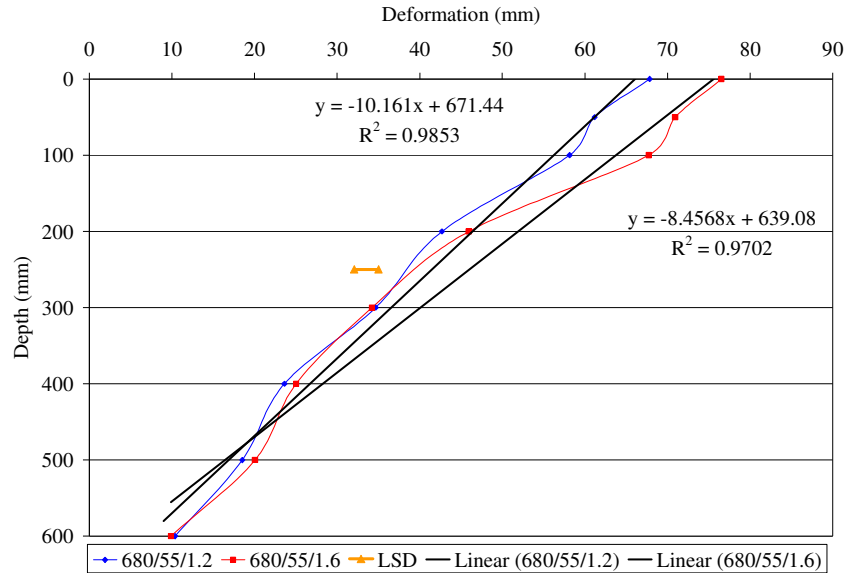


Figure 5.10: Deformation vs. Depth for two different operating pressures

5.7 Rut Characteristics

Reviewing Table 5.3, it can be seen that the Trelleborg 425 tyre and Michelin 750 tyre caused the deepest ruts. Both tyres were subjected to the same loading and inflation pressures and produced rut depths of similar magnitude. Both of these tyres have a chevron tread pattern similar to that of a conventional tractor tyre. Comparing the values gained when the Trelleborg Twin Radial tyre was inflated at 1.2 bar it can be concluded that the increase in rut depth is not linear although the linear regression value for rut depth over the load range for this tyre is 0.9868. The percentage increases noted were as follows, 6.7% increase in rut width and 10% increase in rut depth when tyre load was increased from 40 kN to 50 kN. Comparing the rut width with the values recorded in the contact patch tests for the Trelleborg Twin Radial, section 5.2, it will be noted that there is an upper increase of 56 mm, this is due to the rut characteristic values being a measure taken after three dynamic passes of the tyre. The contact patch was a statically recorded measurement and thus does not have influences such as inconsistent tread pattern due to a multiple pass test or thrust/skid due to drive method.

Table 5.3: Rut characteristics

Tyre	Rut Width (mm)	Rut Depth inc. lug influence (mm)	Inflation Pressure (bar)	Load (kN)
Trelleborg 425	710	80	1.6	50
Michelin 750	710	77	1.6	50
Trelleborg Twin Radial	701	58	1.6	45
Trelleborg Twin Radial	736	55	1.2	50
Trelleborg Twin Radial	700	52	1.2	45
Trelleborg Twin Radial	690	50	1.2	40

5.8 Dry Bulk Density

Figure 5.11 shows the average dry bulk densities (DBD) recorded for the three tyres during their respective studies. The initial DBD was recorded as 1.37g/cm^3 on average for all studies with an average increase in DBD of 10.5%. Due to the high correlation coefficient between all studies a linear relationship between depth and deformation can be assumed. Therefore the equation of the regression line can be converted into a function of depth rather than deformation. This is done by differentiating the equations which reveals the average increase in soil density over depth. The individual increase in DBD for the tyres calculated from the soil deformation plots is as follows; 700 – 15%, 680 – 9% and 750 – 11%. These values fall within the LSD at 95% CI for the actual values, shown in Figure 5.11.

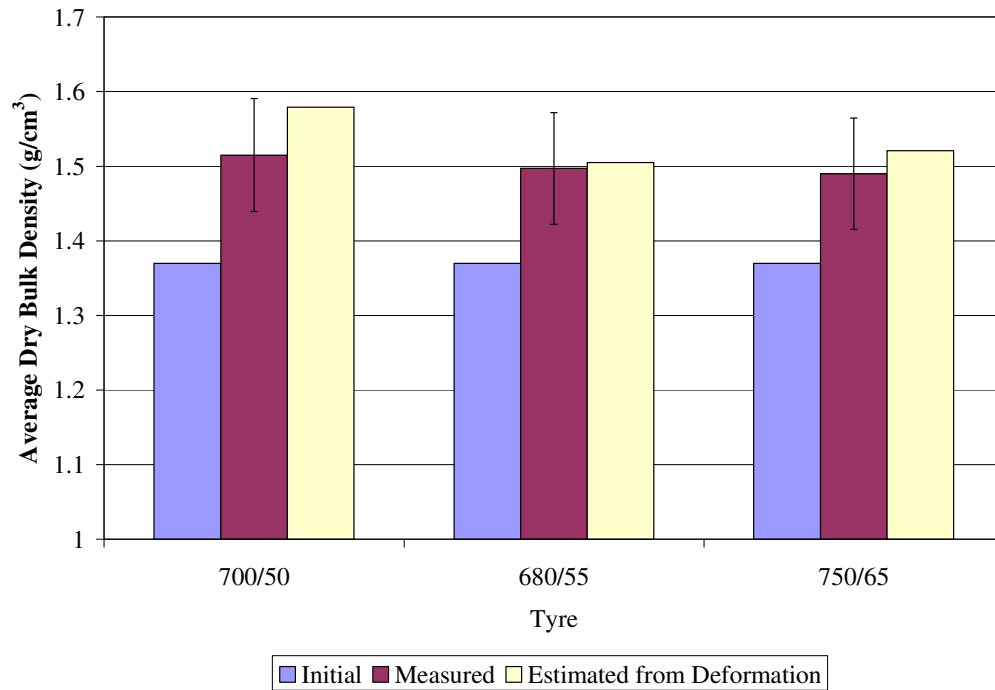


Figure 5.11: Average dry bulk density during tyre testing

5.9 Configuration Comparison

The Claas Lexion combine is a 30,000 kg self propelled harvester which has two standard undercarriage configurations, a four wheeled “classic” combine configuration and a rubber tracked front running gear and small tyre rear axle. The track on a Claas combine carries 10,000 kg per side and thus makes it suitable for comparison with the PMC tandem bogie tyre front axle.

Figure 5.12 shows the optimal track/tyre combination for a Claas Lexion combine and the PMC wheeled tri-axle harvester. From Figure 5.12 it is clear the optimal Claas track configuration is out performed by the PMC configuration within the initial 250 mm of the soil profile. The track causes a significantly higher peak penetration resistance which can be explained by the longer contact patch of the track, as it shears and compacts more soil particles in the topsoil at any one time. The penetration resistance for the Claas configuration declines very quickly and below 250 mm these two plots can be assumed to fall within the LSD.

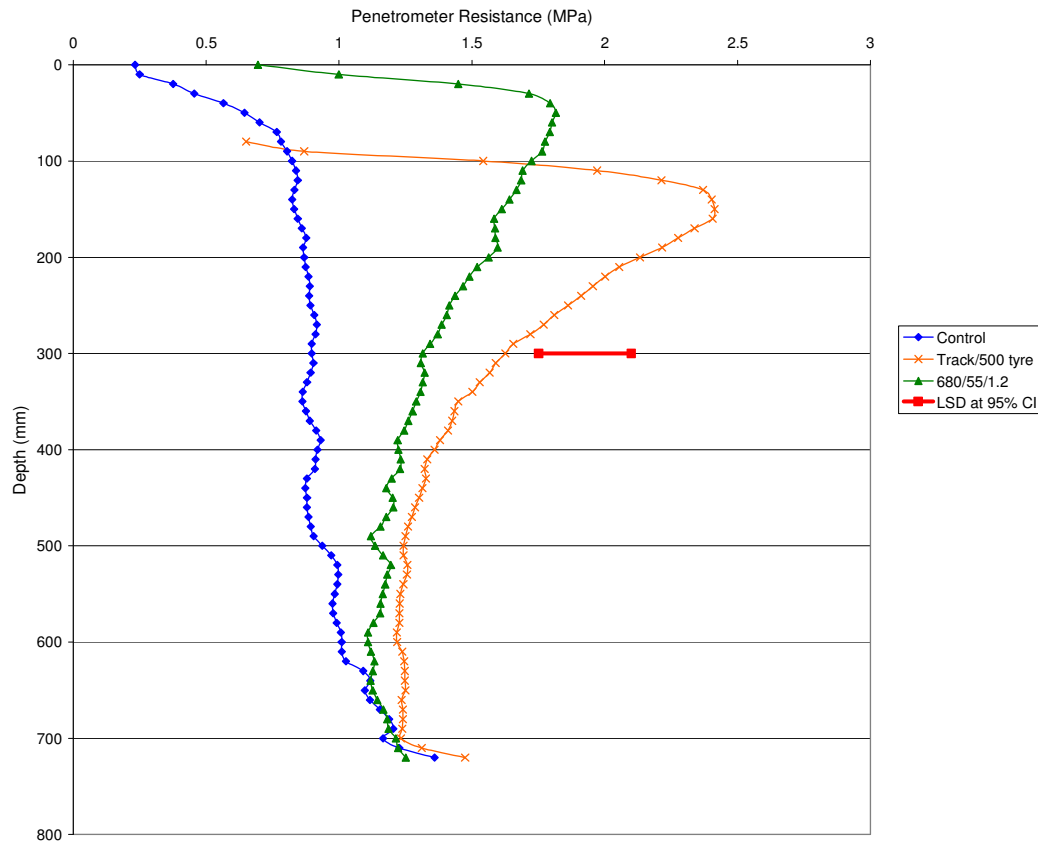


Figure 5.12: Penetration resistance vs. Depth for Claas track and PMC tyre comparison

Figure 5.13 shows that although the 680 tyres initially cause a lower level of deformation on the top 100 mm of the soil profile, Claas's track/tyre combination generates lower compaction from 100 mm to 290 mm depth. Beneath 290 mm the two traces intertwine and fall within the LSD, therefore showing the advantage gained using tracks is minimal.

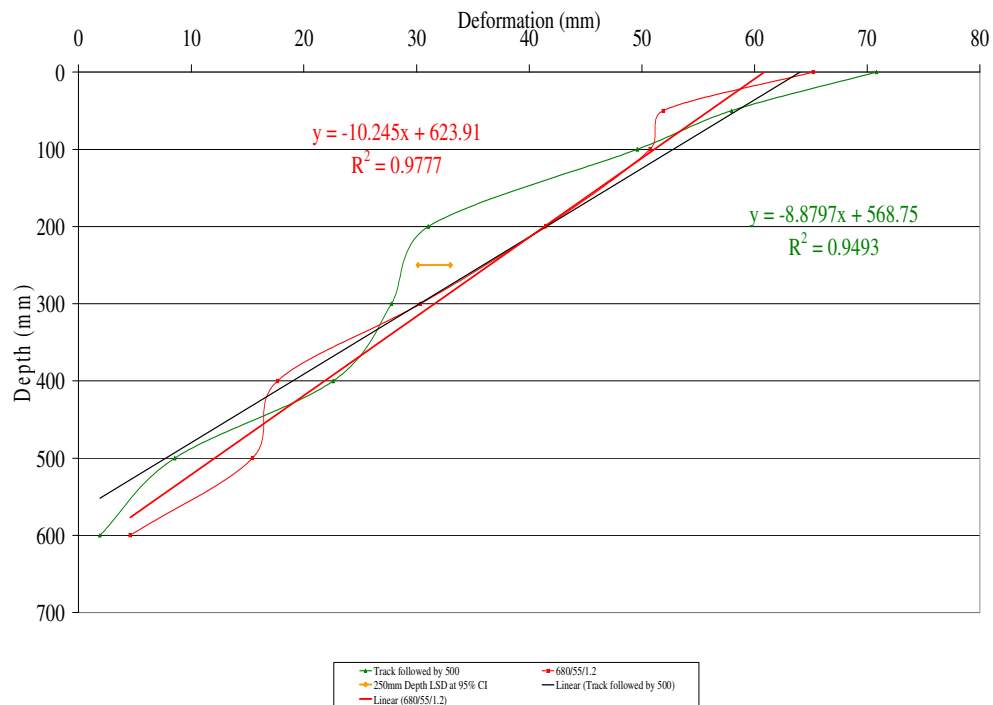


Figure 5.13: Deformation vs. Depth for Claas track/wheel vs. PMC tri-axle wheel configuration

5.10 Compaction Remediation

As discussed in Section 4.5.2, compaction rectification is an expensive process. Figure 5.14 shows the draft force required to pull a sub-soiling tine through the soil profile after a single pass by the Trelleborg Twin Radial at 1.2 bar inflation pressure under 50 kN load. From the graph it is can de deduced that the draft load requirement for compaction remediation following the PMC harvester configuration is 5.5 kN.

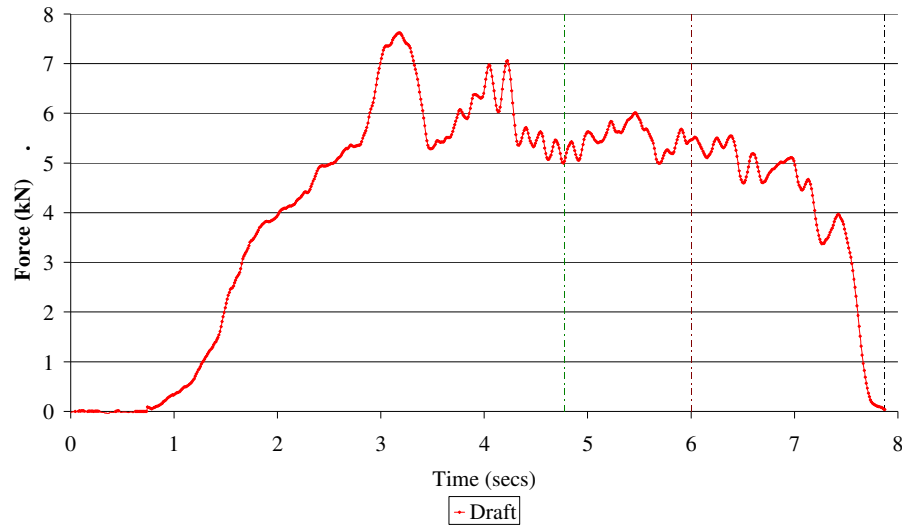


Figure 5.14: Draft force

Table 5.4 shows the draft force requirements when sub-soiling post compaction at a depth of 350 mm for the PMC 979 CT Harvester optimum wheel and Claas combine undercarriage configurations. It shows that the PMC configuration requires lower draft force to be exerted on the tine to remove the compaction. A possible reason for PMC's tyre configuration offering lower draft requirements than Claas track/tyre is the lack of surface hard pan created by the track, however further studies would be required to confirm this theory. This finding implies that using a configuration such as the Claas track/tyre on the PMC machine would incur more expense for the farmer when undertaking post harvest rectification.

Table 5.4: Comparison of draft force requirements

Configuration	Draft Force (kN)	Depth (mm)
PMC optimal tyre	5.5	350
Claas Track/Tyre	10	350
Claas Tyre - standard	15	350

6 FEA Laboratory Study

6.1 Structural Analysis

“Structural analysis is a detailed evaluation intended to ensure that, for any structure, the deformations will be sufficiently below allowable values that structural failure will not occur”, (McGraw-Hill Encyclopaedia of Science and Technology, 5th edition).

Structural analysis may be done by either, hand calculation or computer simulation. By using computer simulation it is possible to analysis complex structures in a time effective manner; software used for such analysis is known as Finite Element Analysis, or FEA. FEA is a mathematical simulation software that accurately predicts how a material or design will react to its environmental influences. FEA was first developed in 1943 by R. Courant for generating approximate solutions to vibration problems. The numerical analysis used in this first system was the Ritz method; however, since 1970 FEA has undergone serious development and evolved to its current state with analysis capabilities ranging from structural to vibrational analysis and fatigue to thermal analysis.

6.2 Methodology

The initial design criterion applied by FMC for the 979 Harvester was; “a factor of safety of 4 should be applied to all major structural components - the chassis and undercarriage should never fail” (personal comments 2). However, this goal was not realised as the machine suffered localised fatigue due to high concentrations of stress near joints and intersections. To remove these fatigue zones the natural progression was to “beef” up the area in question. This had the knock-on effect of moving the stress concentrations to the next weakest zone and causing an increase in weight. The practice of fatigue chasing has continued to occur over the last 18 years of the 979 production cycle.

As stated in Section 1 the PMC 979 CT Harvester has a gross operating mass of 30,000 kg. The harvester is an off-road vehicle that operates in all weather and ground conditions, thus this large mass can have severe adverse effects when operating in non-favourable conditions. As such, it was deemed necessary not only to review the vehicles performance at the interface with its environment but also to identify improvements that would reduce the magnitude of the load acting on this interface.

This scenario posed two questions:

1. How can axle weight be reduced from the current maximum of 10,000 kg?
2. How can stress distribution be improved, as the current configuration causes concentrated pockets of high stress and premature failure?

Utilisation of modern design techniques and software, such as 3D CAD and FEA, allowed comprehensive study of the performance of the current configuration and thus highlighted design changes which could benefit both the stress distribution and overall vehicle gross weight. As with any modelling or computational technique, validation of the techniques used to model and analyse is vital. To perform a thorough comparison and to validate modelling techniques, the computational results must be compared to values retrieved from “real life” tests; therefore the following areas of work were decided upon:

- Quantification of the FEA process relative to real life scenarios,
- Generation of viable options to improve the current chassis and undercarriage.

The tests were carried out in the instrumentation laboratory located at CU@S. This laboratory offers a controlled test facility in which to conduct the work, thus reducing the risk of “noise” influenced results.

6.3 Testing Criteria

Figure 6.1 shows an exploded view of the PMC 979 Harvester main pivot that was chosen for use in the quantification process. The main pivot is a 47 part welded assembly which resembles a “normal” welded assembly in terms of engineering tolerances and construction techniques used on the PMC harvester.

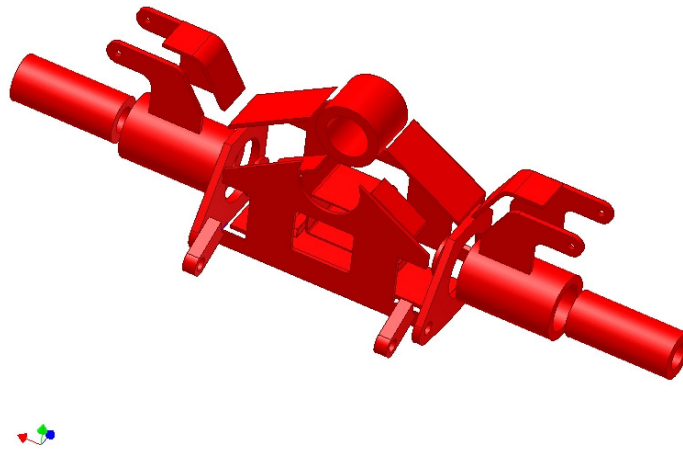


Figure 6.1: Exploded view of PMC Main Pivot

Two loading criteria were decided upon for the “live” testing of the main pivot, as follows;

Single load: vertical load applied through the main pivot centre boss of magnitude ≤ 100 kN, as shown in Figure 6.2.

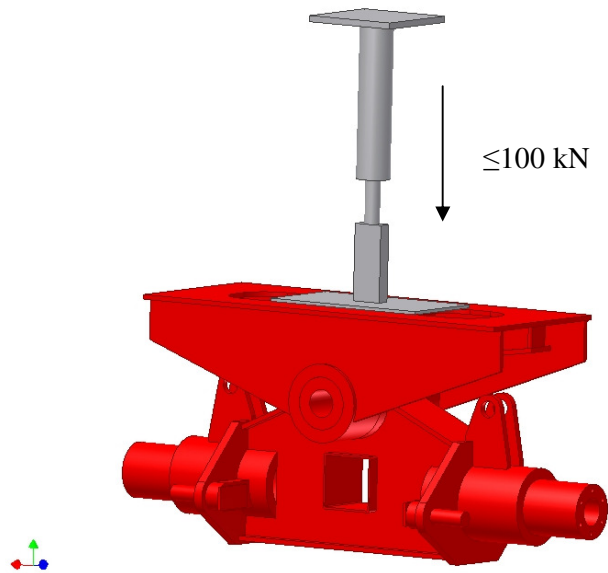


Figure 6.2: Single load case

Multiple load: constant horizontal load of 40 kN applied to the pick-up pins on the main pivot with a varying vertical load of $\leq 100 \text{ kN}$, as shown in Figure 6.3.

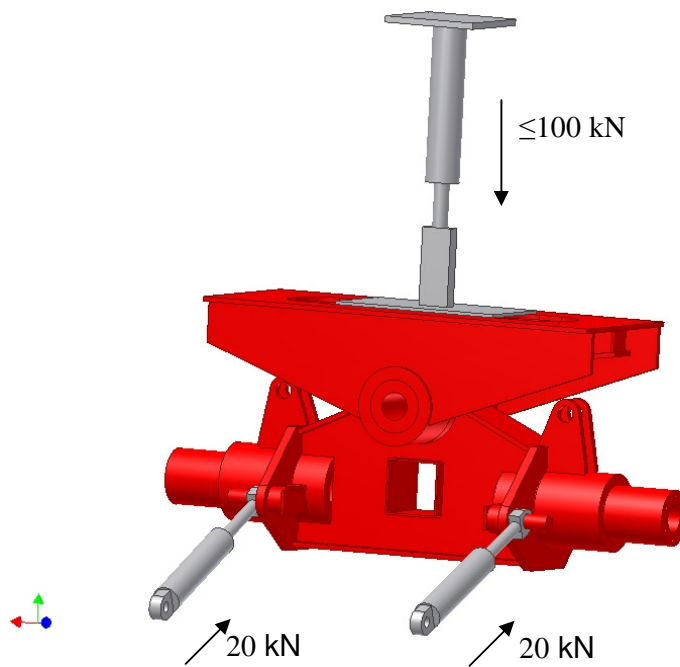


Figure 6.3: Multiple loading case

6.4 Facilities & Equipment

The instrumentation laboratory at CU@S contains a steel calibration frame constructed of 460 mm x 190 mm I-beams bolted together. The floor below the structure consists of fibrous concrete poured to a depth of 1 metre with five steel mounting tracks located along the surface of the floor. The calibration frame is fixed to the floor by T-bolts slotted into the tracks and pulled tight. Previous to this work, the calibration frame had never been used to test such a large piece of equipment and thus the structure itself required to be analysed before it was deemed suitable for this test. To analyse the structure it was recreated in a 3D model, using AI 11, as shown in Figure 6.4.

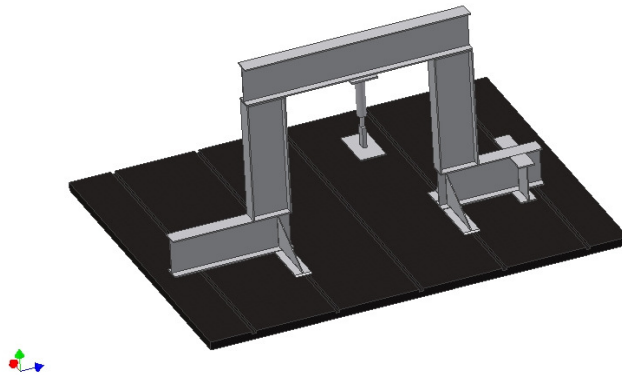


Figure 6.4: Calibration frame

6.5 Review of the Calibration Frame Potential

The first step in the verification was to check the bolt specification for both the structure and the floor mounting. It was found that both the bolts and floor rails were capable of withstanding 1.25 kN per bolt in tension with spacing of 250 mm between bolt centres. The next step was to analyse the I-beams in the calibration frame. The maximum loading criteria was chosen prior to the testing and this was input to the Ansys simulation model, as shown in Figure 6.5.

The following results were obtained for the devised loading criteria:

Maximum stress (von Mises)	48 MPa
Maximum deformation (mm)	0.34 mm

For a detailed description of von Mises stress refer to Section 6.12.

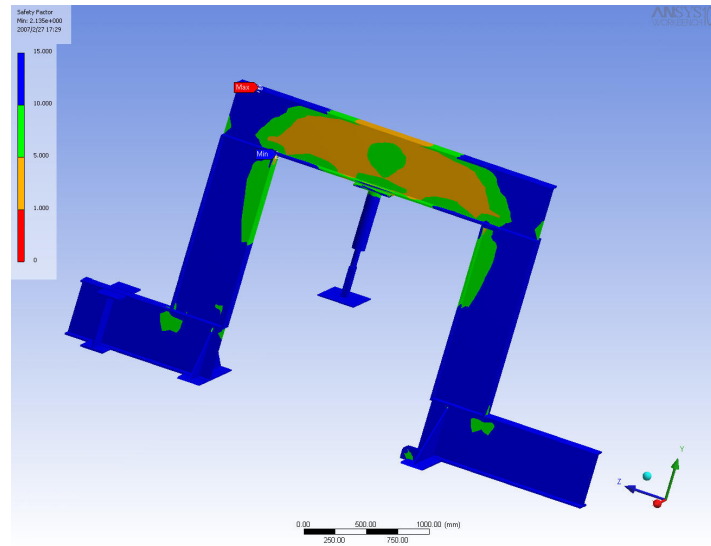


Figure 6.5: FEA screenshot of calibration frame during analysis

After quantifying the suitability of the calibration frame for the testing sequence, the rig for holding the axle during testing was designed. It was decided I-beams provided the optimum shape for construction of the structure due to longitudinal loading and zero lateral loading. By placing a CAD model of the main pivot into the calibration frame model the geometrical spacing could be visualised, and thus the rig height and span was determined.

Figure 6.6 shows the main pivot stand developed for the test rig. The footplates were welded on their top edge and down their sides, ensuring no weld was applied to the underside, as this would result in uneven contact between the stand and the concrete floor. The upper I-beam section was drilled for six M16 holes equidistantly spaced on a 140 mm PCD, these matched up to the threaded holes on the face of the axle stub shafts, thus creating a bolted connection to join the axle to the rig.

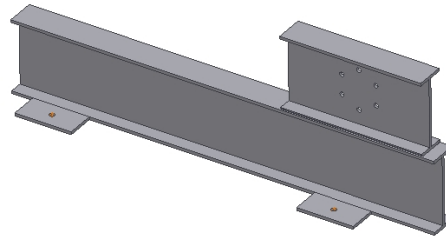


Figure 6.6: Main Pivot stand

The main pivot stands were subjected to FEA to quantify the levels of stress and deformation that would be generated during testing, as shown in Figure 6.7. The following values were recorded from Ansys 10:

Maximum stress (von Mises)	29 MPa
Total deformation	0.45 mm

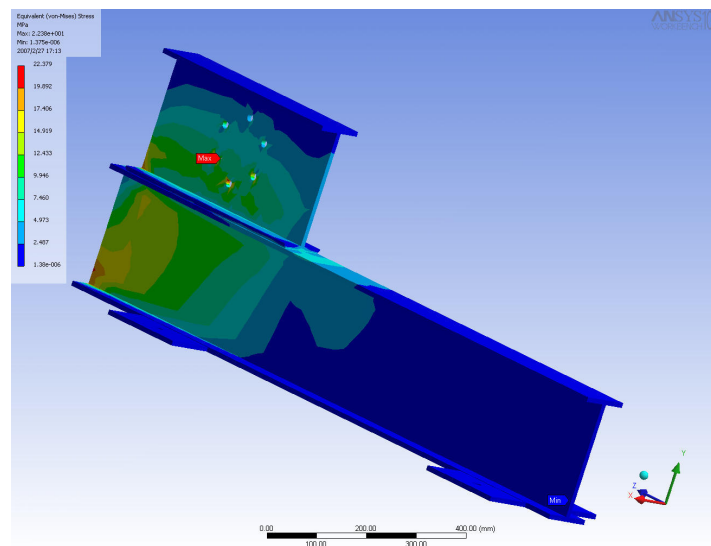


Figure 6.7: FEA screenshot of main pivot stand under defined loading criteria

The main pivot was to be subjected to a multi-load test sequence; therefore a mounting point perpendicular to the axle was designed, as shown in Figure 6.8. Due to the rail spacing and maximum load capability it was necessary to design a unique mount that welded to the base of the calibration frame and utilised its complex fixing pattern. Additionally, using the base of the calibration frame was advantageous, as loads generated from the diagonal force were directed into the concrete floor, reducing the applied moment and thus stress on the tracks and T-bolts.

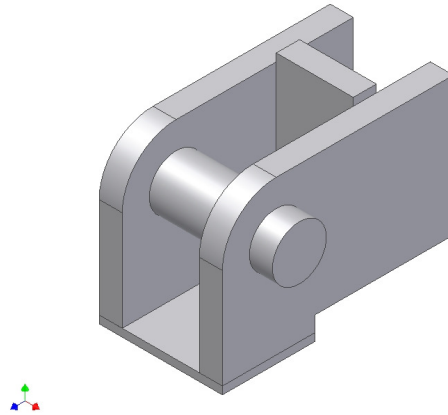


Figure 6.8: Cylinder mount

As with all of the previous designs the cylinder mount was analysed with Ansys, as per Figure 6.9. The results gained from the FEA were as follows:

Maximum stress (von Mises)	34 MPa
Total deformation	0.45 mm

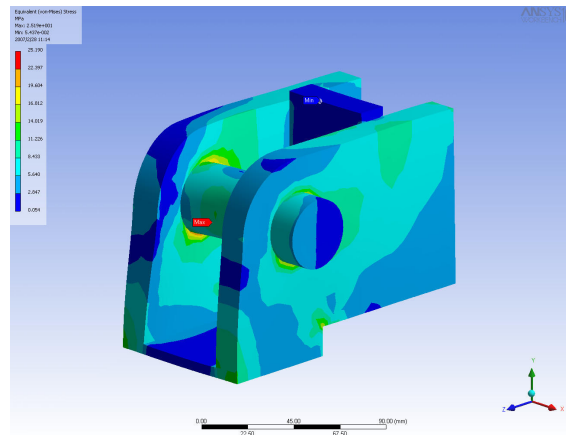


Figure 6.9: FEA screenshot of cylinder mount

Before engineering drawings were compiled the complete model was assembled within AI 11 to check for possible fouling in the layout. Using 3D CAD offers an accuracy level of ± 0.0001 mm.

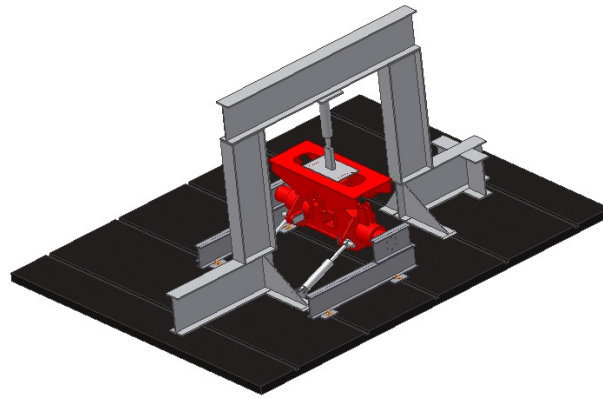


Figure 6.10: Full model of instrumentation facilities at CU@S

Figure 6.10 and Figure 6.11 show a model of the test facility at CU@S. The model includes the calibration frame, PMC main pivot, axle stands, cylinder mounts and cylinders

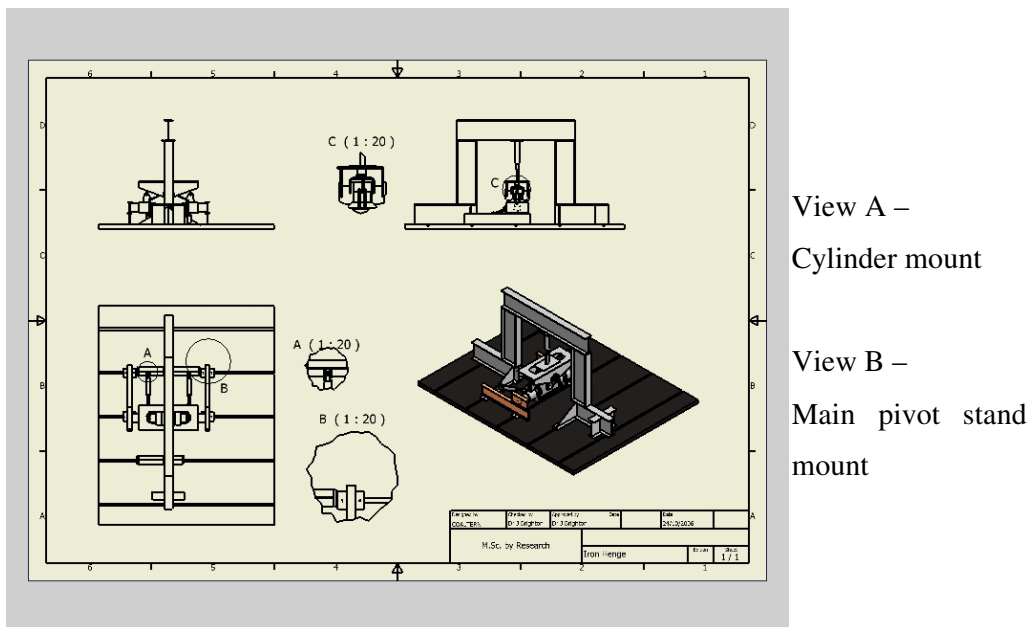


Figure 6.11: Layout drawing of the test bed with three detailed views

6.6 Hydraulic System

As mentioned previously, the maximum single required force will be ≤ 100 kN; to achieve this force a portable hydraulic pump was used. Two hydraulic cylinders were obtained from PMC Harvesters with maximum capabilities of 125 kN at 220 bar. The PMC cylinders provided the diagonal loading, and the single cylinder already fitted to the calibration frame, with 150 kN capability at 150 bar potential, supplied the vertical loading. To utilise the portable power pack a hydraulic system was designed that contained the items indicated in Table 6.1, configured as per Figure 6.12.

Table 6.1: Bill of Materials for hydraulic system

No.	Item	Quantity	Specification	Operating Pressure
1	Power pack	1	3-phase motor, fixed displacement pump	
2	Vertical cylinder	1	150 kN @ 100 bar	100 bar
3	Horizontal cylinder	2	125kN @ 220 bar	50 bar
4	T valve	2	Inline installation	
5	Calibrated pressure gauge	2	0 - 200 bar gauge	

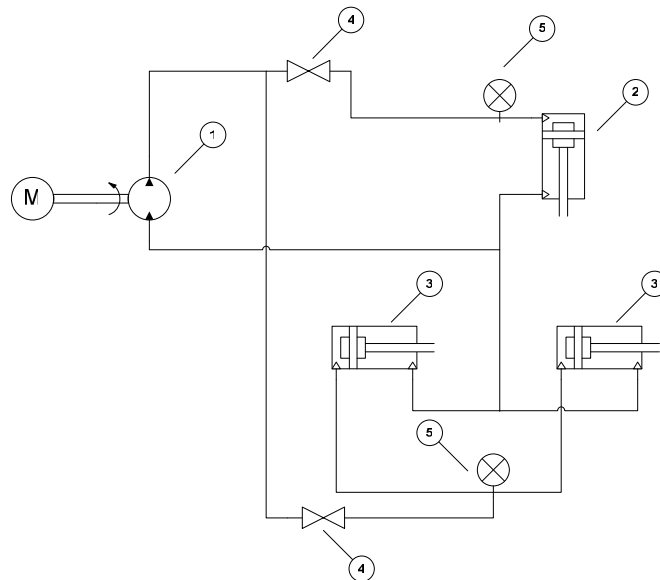


Figure 6.12: Schematic of the hydraulic system

6.7 Strain Gauges and Installation Techniques

The techniques used to apply a strain gauge are critical to the ability of the gauge to give accurate and replicable readings. When preparing a test sample, several different steps are involved before a gauge can be cemented in place. The following is a basic guide for strain gauge installation. For a more comprehensive explanation of the techniques refer to Perry & Lissner (1962).

The first objective is to prepare the area of the test sample. All contaminants, such as paint, rust and dirt must be removed. This can be carried out using a range of emery papers, starting with coarse grit, such as P80, moving sequentially to a fine grit paper, such as a P400, with wet treatment. Although the surface must be smooth and clean, over polishing will lead to poor adhesion of the gauges. This has obvious detrimental effects on the accuracy of the gauges.

Once the area has been sanded, the next step is to decontaminate the test sample by the application of metal conditioner followed by neutraliser. Cleanliness is paramount at this point - care should be taken not to contaminate the gauge area - this is achieved by using fresh swabs once and wiping the solutions from the centre to the outside; no contact should be made with the test area after it has been cleaned.

To fit the gauges in the correct orientation lines should be burnished onto the surface, the lines should not pass under the gauge, but mark the boundary locations; a burr in the metal below the gauge could lead to a short or open circuit. Bonding of the gauges is one of the most critical aspects to the fitting of the strain gauges; if the bonding is not carried out correctly then random fluctuations may occur.

The gauges are bonded using strain gauge “super glue”. The super glue is applied evenly to the prepared metal surface, then, using adhesive tape, the gauge is picked up. The gauge is “rolled” into position, once contact has been made application of even pressure is required until the glue has cured. Once the gauge is bonded the adhesive tape is removed by pulling it back on itself with a constant even pull.

There are four common types of strain gauge configurations used in instrumentation. Rosette gauges were chosen for this application; they offer a comprehensive view of the strains within a 90° range as they feature three gauges, rather than two as found on a standard rectangular gauge. The strain gauges were configured in a $\frac{1}{4}$ bridge layout with the other three “dummy” bridges located on a calibrated EORT. Figure 6.13 shows the electrical schematic for the logging circuit used in the calibration frame tests.

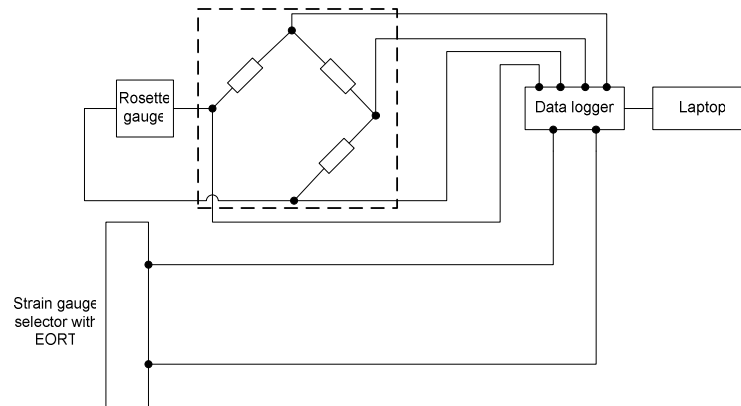


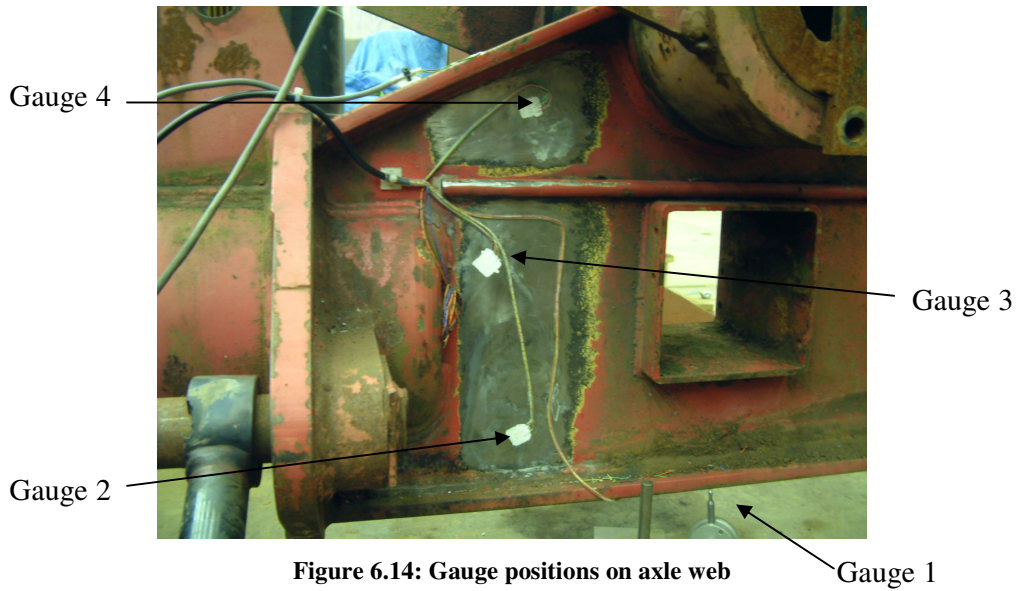
Figure 6.13: Data logger circuit diagram

6.8 Gauge Location

Five sets of rosette gauges were fitted to the PMC main pivot; the breakdown of their position is shown in Figure 6.14 and Figure 6.15 and gauge wiring in Table 6.2.

Table 6.2: Gauge configuration

Gauge	Type	Number of wired gauges
1	Rosette	2
2	Rosette	3
3	Rosette	3
4	Rosette	3
5	Rosette	3



6.9 Testing Procedure

The procedure used for obtaining the measured results was as follows:

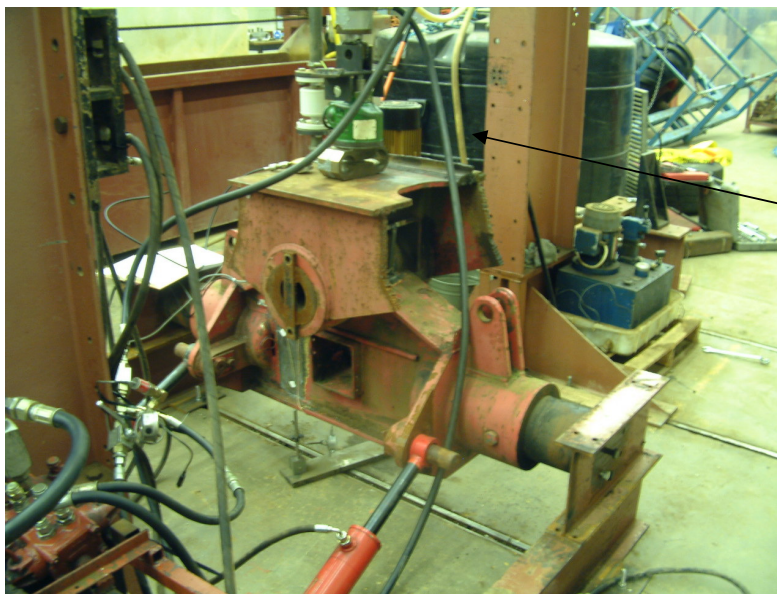
1. Start DaisyLab,
2. Switch to chosen gauge,
3. Load to desired value,
4. Switch DaisyLab to record,

5. Slowly release load and continue recording until load fully released.



Figure 6.16: Axle during testing

As testing (shown in Figure 6.16) progressed it became clear that the portable power pack was not capable of producing the required maximum pressure nor could it maintain a pressure of more than 100 bar long enough to carry out all the necessary tests. Therefore, it was necessary to evolve the hydraulic system into a mechanical/hydraulic system. A bottle jack was used to exert force through the main bush via a calibrated EORT while the hydraulic system generated the diagonal loading, as shown in Figure 6.17. The datalogging software was also modified to accept the load data from the EORT.



Jack &
EORT

Figure 6.17: EORT and bottle jack being used during testing

6.9.1 Comparison between Computational and Measured Results

The computer model was manipulated such that five additional coordinate systems were placed locally within the model, three of which are shown in Figure 6.18. These coordinate systems corresponded to the gauge locations on the actual axle, to an accuracy of ± 1 mm, allowing accurate comparison of results.

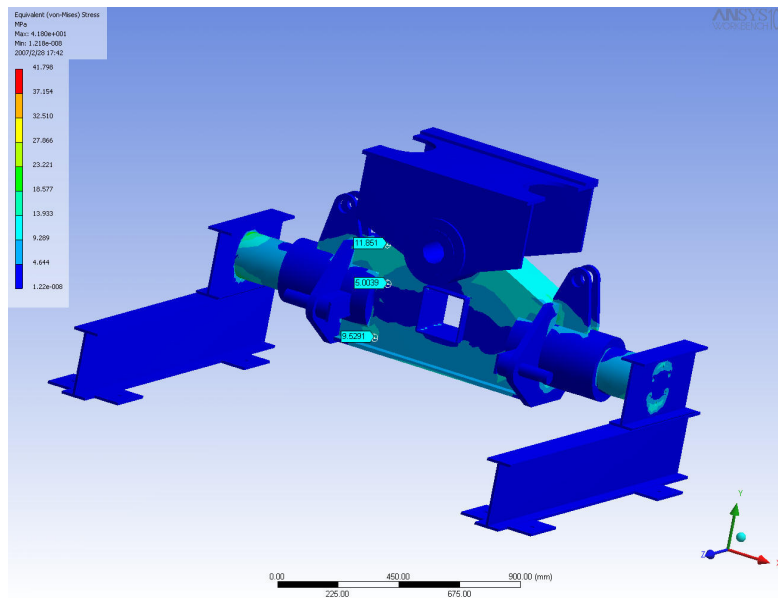


Figure 6.18: Analysed main pivot assembly showing gauge locations

6.10 Calculation of Loads

The EORT used for measuring the vertical load applied by the jack was calibrated in an Avery test machine at CU@S, Figure 6.19 shows the results from the calibration process. The raw output voltage was recorded using Daisylab 8.0.

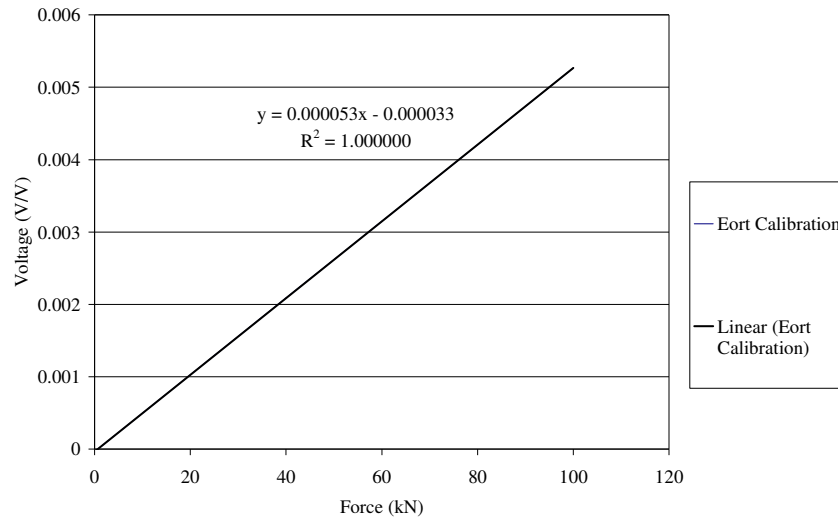


Figure 6.19: EORT calibration graph and equation

$$V/V = 0.000053f - 0.00003$$

Equation 6.1: EORT calibration co-efficient

where:

- V/V volts/volt, dimensionless
 f force, kN

6.11 Measured Results Processing

The initial results were processed with MS Excel. Table 6.3: Excel processing table shows an extract from these results. Columns 1 and 2 are raw data values as recorded by DaisyLab. Column 3 shows the true value retrieved from the EORT as the system did not start with a zero value. Column 4 shows the corrected value from the EORT, which was then inserted into the EORT calibration equation (Equation 6.1) thus producing a value for the actual force generated by the bottle jack (column 5). Column 6 shows delta V from the gauge while column 7 is the value, which is used in the strain calculation. Column 8 is the calculated value of strain at the given force. This accounts the bridge factor and gauge factor.

Table 6.3: Excel processing table

Column1	Column2	Column3	Column4	Column5	Column6	Column7	Column8
EORT (V)	Gauge (V)	Raw EORT (V)	Corrected EORT	Force (kN)	Gauge (Delta V)	Gauge (Delta V/V)	Strain
-5.29761	-0.30932	5.432835	0.005433	103.129	0.003864	7.73E-06	2.5760E-5
-5.29759	-0.30934	5.432818	0.005433	103.1286	0.003843	7.69E-06	2.5620E-5
-5.29749	-0.30935	5.432718	0.005433	103.1268	0.003833	7.67E-06	2.5553E-5

The strain was calculated using Equation 6.2, which uses values specific to the experiment configuration at the time of testing;

$$\varepsilon = \frac{V_{gauge}}{Gain \times V_{in}} \frac{1}{GF \times BF}$$

Equation 6.2: Strain calculation

where:

- ε strain
- V_{gauge} gauge voltage, V
- V_{in} input voltage, 5V
- $Gain$ gain, 100
- GF gauge factor, 1.2
- BF bridge factor, 0.25

Strain versus force was then plotted (Figure 6.20) to give Equation 6.3, which was used to retrieve values for strain at any given load. These values were then inserted into Equation 6.4 and Equation 6.5.

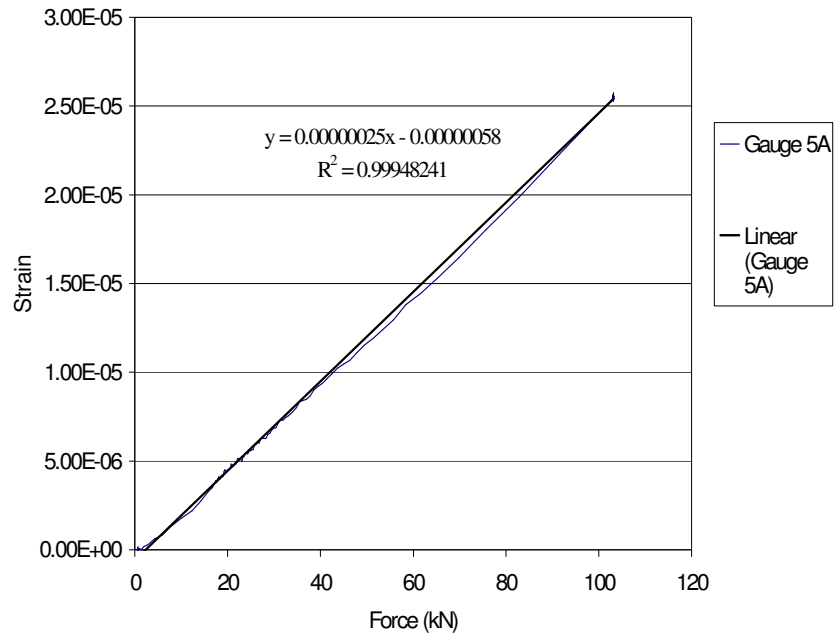


Figure 6.20: Strain vs. Load for strain gauge

$$\varepsilon = 0.00000025 f - 0.00000058$$

Equation 6.3: Strain vs. Load

where:

- ε strain
- f force, kN

The maximum normal stress was then obtained using the corresponding values from Figure 6.20 and either Equation 6.4 or Equation 6.5 depending on which gauge type was being calculated.

$$\sigma_{\max} = \frac{E}{2} \left\{ \frac{\varepsilon_1 + \varepsilon_3}{1 - \mu} + \frac{1}{1 + \mu} \sqrt{(\varepsilon_1 - \varepsilon_3)^2 + [2\varepsilon_2 - (\varepsilon_1 + \varepsilon_3)]^2} \right\}$$

Equation 6.4: Maximum normal stress – rosette gauge set, 3 gauges wired

where:

- σ_{\max} maximum normal stress
- ε_1 strain at point 1
- ε_2 strain at point 2
- ε_3 strain at point 3

μ Poisson's ratio
 E Young's modulus

$$\sigma_{\max} = \frac{E}{1 - \mu^2} (\varepsilon_1 + \mu\varepsilon_2)$$

Equation 6.5: Maximum normal stress – rosette gauge set, 2 gauges wired

where:

σ_{\max} maximum normal stress
 ε_1 strain at point 1
 ε_2 strain at point 2
 μ Poisson's ratio
 E Young's modulus

Poisson's ratio is the ratio of transverse contraction strain to longitudinal extension strain in the direction of the tension force, as shown by Equation 6.6 and Figure 6.21.

$$\mu = -\frac{\varepsilon_{\text{transitional}}}{\varepsilon_{\text{longitudinal}}}$$

Equation 6.6: Poisson's ratio

where:

μ Poisson's ratio
 $\varepsilon_{\text{transitional}}$ transitional strain
 $\varepsilon_{\text{longitudinal}}$ longitudinal strain

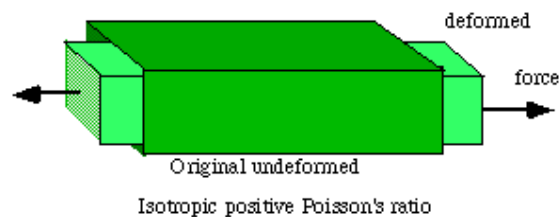


Figure 6.21: Diagrammatic view of Poisson's ratio

6.12 Computational Result Processing

Ansys 10 uses two main criteria for stress calculation, they are as follows;

- Tresca (maximum shear stress) – Equation 6.7
- von Mises (equivalent stress) – Equation 6.8

Figure 6.22 shows a graphical comparison between the two criteria, it clearly shows the Tresca criterion (dashed line) produces a linear plot and von Mises an elliptical plot, therefore it can be assumed that the von Mises criterion may over estimate stress values within an analysed structure. This was confirmed by the findings of Zhu and Leis (2006) which showed the von Mises criteria over estimated by 12% on average when compared to Tresca.

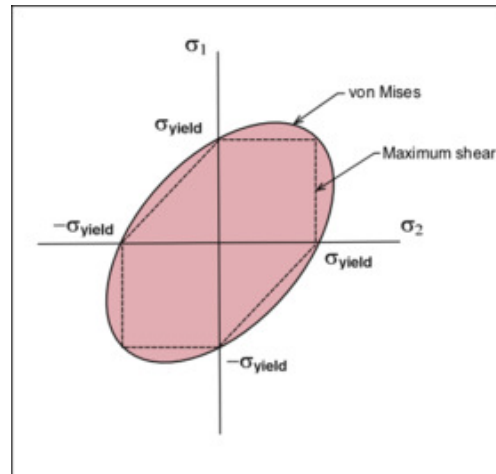


Figure 6.22: Graphical representation of von Mises and Tresca criteria

$$\sigma_{\max} = \frac{E}{2(1+\mu)} \sqrt{(\varepsilon_1 - \varepsilon_2)^2 + [2\varepsilon_2 - (\varepsilon_1 + \varepsilon_2)]^2}$$

Equation 6.7: Tresca (Maximum shear stress)

where:

- σ_{\max} maximum shear stress
- ε_1 strain at point 1
- ε_2 strain at point 2
- μ Poisson's ratio
- E Young's modulus

Ansys relates the equivalent stress to the principle stresses using Equation 6.8.

$$\sigma_v = \sqrt{\frac{(\sigma_1 - \sigma_2)^2 + (\sigma_2 - \sigma_3)^2 + (\sigma_3 - \sigma_1)^2}{2}}$$

Equation 6.8: Equivalent stress (von Mises)

where:

- σ_v equivalent stress
- σ_1 stress at point 1
- σ_2 stress at point 2
- σ_3 stress at point 3

7 FEA Results and Discussions

7.1 Single Load Tests

A load was applied vertically through the main boss of the main pivot, compressing the assembly, mimicking normal load application. It was chosen that the maximum singular permissible load to be exerted by the calibration frame would be 100 kN which is 50% of the normal main pivot vertical load.

During the testing process it was noted several of the gauges were subject to random interference, after closer inspection of the gauges it was concluded that they had moved before complete curing. This movement caused the film of super glue to vary in thickness thus allowing the gauges to creep during testing. The gauges affected were located on the axle web, which did not pose a major concern as the gauges mounted on the upper and lower flanges were working correctly and offered optimal locations for data acquisition.

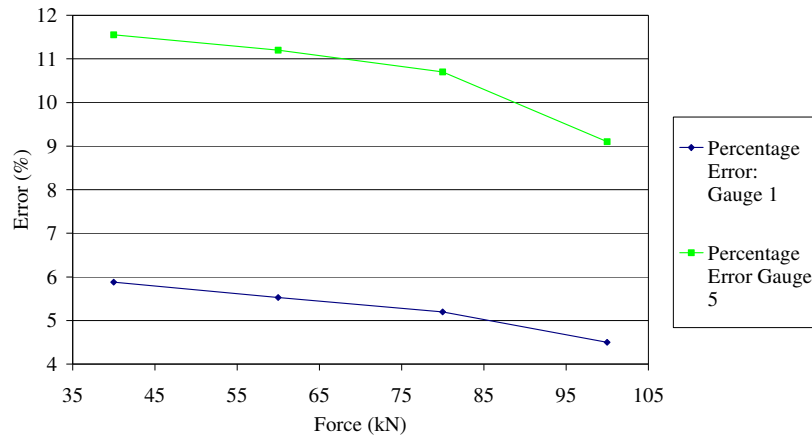
Table 7.1 and Table 7.2 show a small representation of the many values generated during testing. The tables list the calculated percentage error between the measured stress and simulation stress for gauges 1 and 5. Looking at the change in percentage error in both tables we see that as the load is increased, the rate of over estimation by Ansys is reduced. One explanation for the decrease in over estimation is that the PMC main pivot is a welded assembly which has minor levels of residual stress in-built due to the fabrication process; therefore the low loads are overcoming the residual stresses.

Table 7.1: Results for gauge number 1 under single loading

Force (kN)	Actual Stress (MPa)	FEA model Stress (MPa)	Error
40	3.61E+06	3.83E+06	5.74%
60	5.46E+06	5.78E+06	5.54%
80	7.31E+06	7.71E+06	5.19%
100	9.16E+06	9.59E+06	4.48%

Table 7.2: Results for gauge number 5 under single loading

Force (kN)	Actual Stress (MPa)	FEA model Stress (MPa)	Error
40	4.27E+06	4.83E+06	11.59%
60	6.67E+06	7.51E+06	11.19%
80	8.51E+06	9.54E+06	10.80%
100	1.06E+07	1.16E+07	8.62%

**Figure 7.1: Error plot for gauge 1 and gauge 5 for single load test**

Looking at Figure 7.1 we see that both traces have a very similar shape with gauge 5 being approximately 5% higher in error throughout the load range. Both traces take a slight down turn in percentage error rate at approximately 80 kN force which suggests that the load has overcome the residual stress in the main pivot and now the pivot is under a true loaded scenario.

The average error percentage, shown in Figure 7.2, for the single load case is 8.75% at 40 kN and declines to 7% at 100 kN load. The error is in the order of over estimation of the stresses therefore Ansys in this particular case is giving values which would offer a built-in safety factor of approximately 7%.

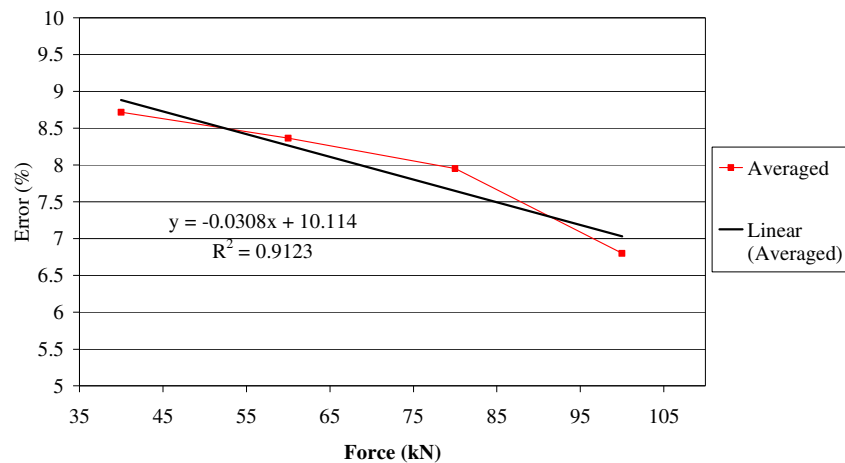


Figure 7.2: Average error for gauge 1 and gauge 5 for single load test

7.2 Multi load tests

The multi load test uses the same vertical loading as the single load test and includes a fixed magnitude diagonal load on the pick-up pins of the main pivot. This load adds two extra force components to the test and causes a twisting effect of the axle thus making the simulation of the test procedure much more complex.

Values for both gauges are shown in the tables below (Table 7.3 and Table 7.4), as per the single load test it can be seen that the errors recorded in the low force simulations are the highest and as the force increases the errors decrease. By applying the additional diagonal load a 3% increase in gauge 1's peak error occurs when compared to the single load test, however at 100 kN the error is much lower than that calculated in the single load test.

Gauge 5's error increase is dramatic in comparison to the single load test. At 40 kN the error is over 30% with a reduction to 15.9% at 100 kN, these values are highly exaggerated when compared to the single load tests. An increase in percentage error would be normal when further loads are added however the increase seen in gauge 5 results could be deemed as too high.

Gauge 1 was located at the centre of the lower flange with no weld zones or edges close by, gauge 5 was close to the edge of the upper flange and was approximately 15 mm from a weld joint. Both these factors could affect the readings obtained from gauge 5. The upper flange has compression from the vertical load and twist applied in the vertical direction by the diagonal load which may have distorted the reading as the gauge was near to the edge.

Table 7.3: Results for gauge number 1 under multi loading

Force (kN)	Actual Stress (MPa)	FEA model Stress (MPa)	Error
40	3.91E+06	4.26E+06	8.22%
60	5.89E+06	6.34E+06	7.10%
80	7.88E+06	8.32E+06	5.29%
100	9.86E+06	9.93E+06	0.70%

Table 7.4: Results for gauge number 5 under multi loading

Force (kN)	Actual Stress (MPa)	FEA model Stress (MPa)	Error
40	4.33E+06	6.20E+06	30.16%
60	6.58E+06	8.59E+06	23.40%
80	8.83E+06	1.10E+07	19.73%
100	1.11E+07	1.32E+07	15.91%

Figure 7.3 shows the calculated error plots between recorded test and simulation for gauges 1 and 5. Gauge 1 shows a slow decline in error rate in the 40 kN - 80 kN range with a marginal increase in the gradient of percentage error thereafter. The plot of gauge 1 is relatively constant in shape when compared to the single load test plot for gauge 1.

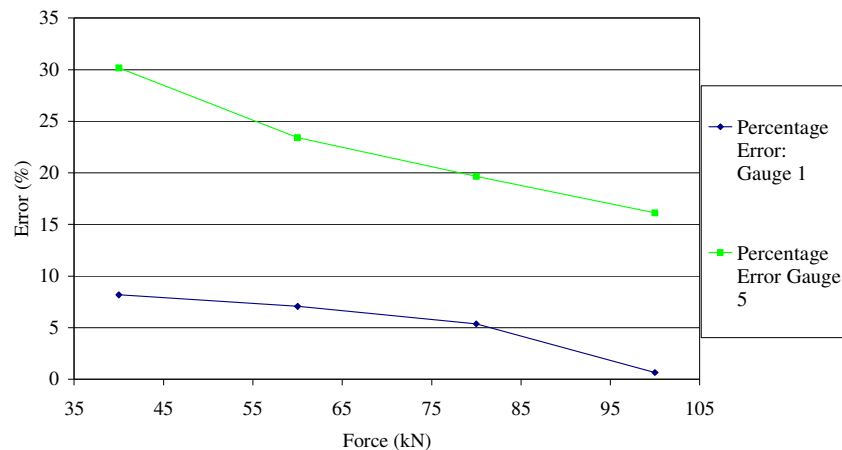


Figure 7.3: Error plot for gauge 1 and gauge 5 for multi-load test

Gauge 5 shows a sharp decline within the first 60 kN load, subsequent loading generates a relatively uniform percentage error plot. The plot of the percentage error for this gauge shows slightly different characteristics when compared to its counterpart from the single load test. The rate of error declines with increasing load, however it does not take the same shape as the single load trace. This could be explained by the constraint techniques used to hold the model in the simulation and/or the welded section edge close to the gauge distorting the reading.

Figure 7.4 shows the average error for the multi load test. The combined error rate is 19.2% at 40 kN and 8% at 100 kN. The regression value for the line is very close to one, suggesting that the percentage error rate is very close to a linear relationship and therefore could be accurately predicted for different loads.

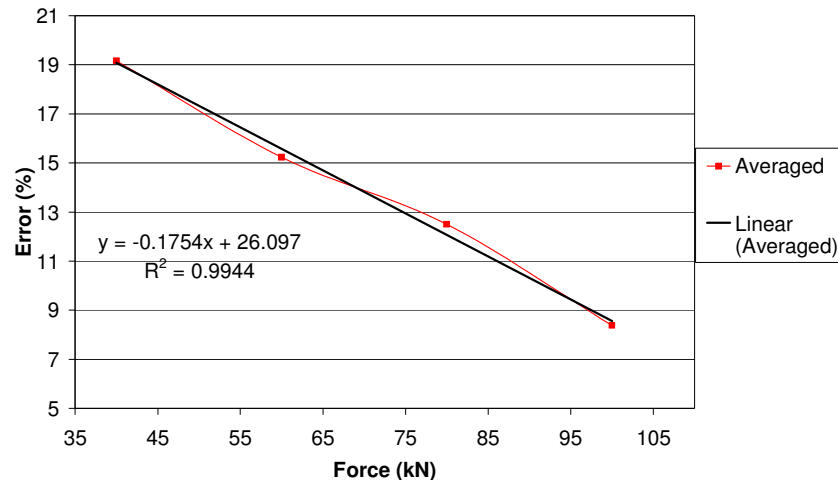


Figure 7.4: Average error for gauge 1 and gauge 5 for multi load test

7.3 Prediction of Tests

The PMC axle is subjected to a maximum load of 200 kN in field conditions, this loading falls within the linear region of extension for the structure. The normal vertical load which the main pivot is subjected to is 200 kN. Using the equations generated from the linear trend lines for the previous graphs a prediction of the stress under normal vertical loading conditions has been made. The simulation model was then configured using the new load, tested and percentage errors calculated.

Figure 7.5 shows the results for the predicted single load test case. Reviewing the plot shows that the over prediction by Ansys has continued through to the 200 kN mark with the estimated average error being 4%.

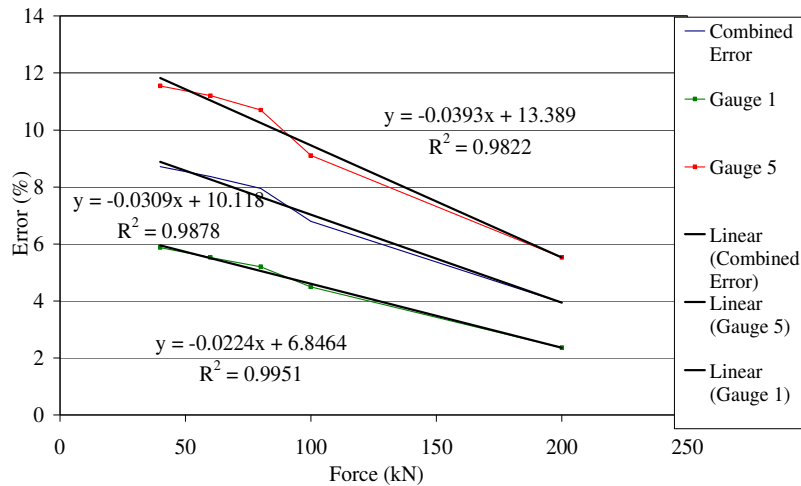


Figure 7.5: Prediction of errors in stress values at 200 kN in single load test

Figure 7.6 shows a different scenario with Ansys under predicting by 8% for the average of the two gauge values. Utilising the results from the propagations of both test cases, a recommendation that a 10% safety factor should be applied to the obtained stress values can be made in order to offer a buffer in the design process for the PMC application.

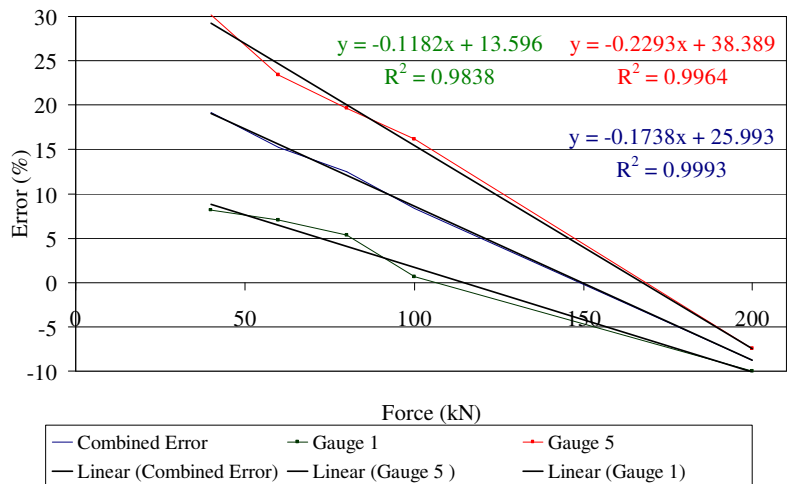


Figure 7.6: Prediction of errors in stress values at 200kN in multi load test

7.4 FEA comparison with Welding Institute report and Ansys on chassis

In 1988 FMC Harvesters contracted the Welding Institute to undertake strain gauge verification of the chassis. The chassis suffered major problems with fatigue occurring at the “dog leg” in the main structure. Table 7.5 shows values documented by the Welding Institute report and values which were obtained by undertaking analysis of the 1988 specification chassis in Ansys 10, while Figure 7.7 shows the Ansys analysis of the 1988 chassis.

Table 7.5: Comparison of Welding Institute testing and Ansys 10 simulations

Test Point	WI Stress (MPa)	Ansys Stress (MPa)	Error
1	70	71.076	1.54%
2	32	33	3.13%
3	20	22.671	13.36%
4	46	47.801	3.92%
5	90	90.73	2.16%
6	47	52.57	12.77%
7	63	62.395	-0.96%
8	117	117	0.00%

Comparing the results from the Welding Institute report and the Ansys simulation, Figure 7.7, it can be seen the difference is relatively low with the modulus of error across all eight test points being 4.74%. Reviewing Pt6 it can be noted that it is underestimated by 0.96%, if the proposed safety margin of 10% was applied to the simulation stress value then a new percentage error rate for Pt6 of 7.85% over estimated would be obtained, therefore suggesting that a simulated model would never have lower stress levels than a measured test piece when the safety margin was applied.

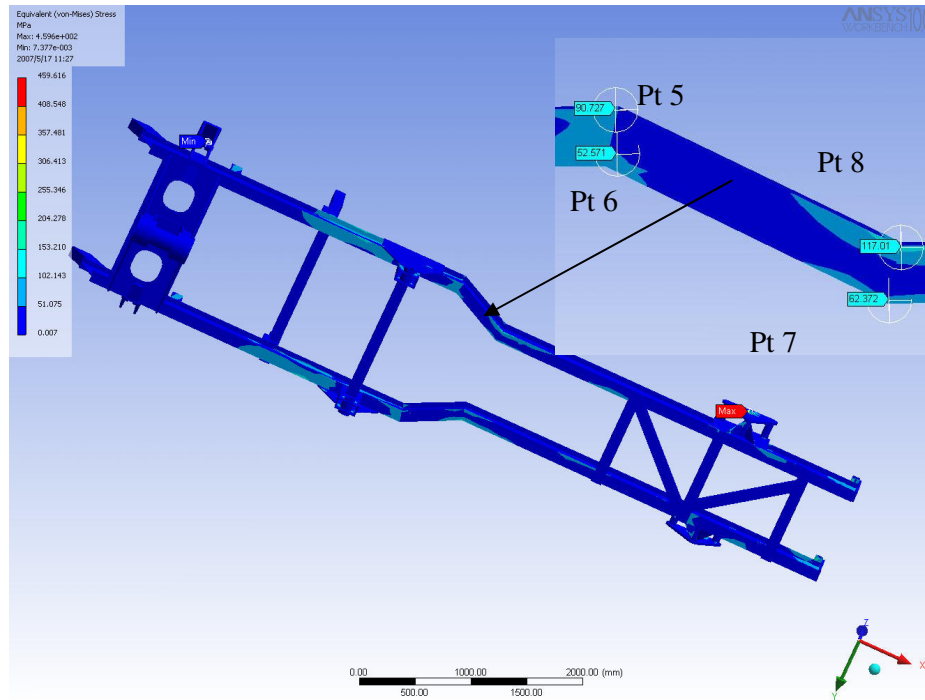


Figure 7.7: Trelleborg Twin: Screen shot of 1988 Chassis in Ansys 10 with four test points marked

By reviewing both the FEA verification testing held at CU@S and the results taken from the Welding Institute report (1988) it is warranted to state the following: When using Ansys 10 as a design tool a safety factor of 10% should be added to simulation results to maintain integrity between simulation and real stress values.

8 Support Structure Development

8.1 Modelling Technique

Ansys 10 FEA software is a versatile analysis tool; however it does not support weld joint analysis. The FEA verification carried out in the previous section quantified the percentage error in the modelling technique required to overcome this inadequacy of Ansys 10. The principle of the technique was to remove all engineering tolerances from the assembly and finish joints flush, therefore making Ansys assume the bodies were in bonded contact. The mesh subsequently generated formed symmetrically in the joint regions. The overall aim was to reduce the compaction generated by the 979 CT, hence by targeting the overall vehicle weight a reduction can be made in wheel load and as proved in section 5.2 a reduction in compaction will be noted. The development work remit was to evolve the PMC 979 CT, rather than create a new harvester, as the current machine is a world leader in its market place and PMC's current research and development budget offers restrictive monies for new machine development.

8.2 Main Pivot

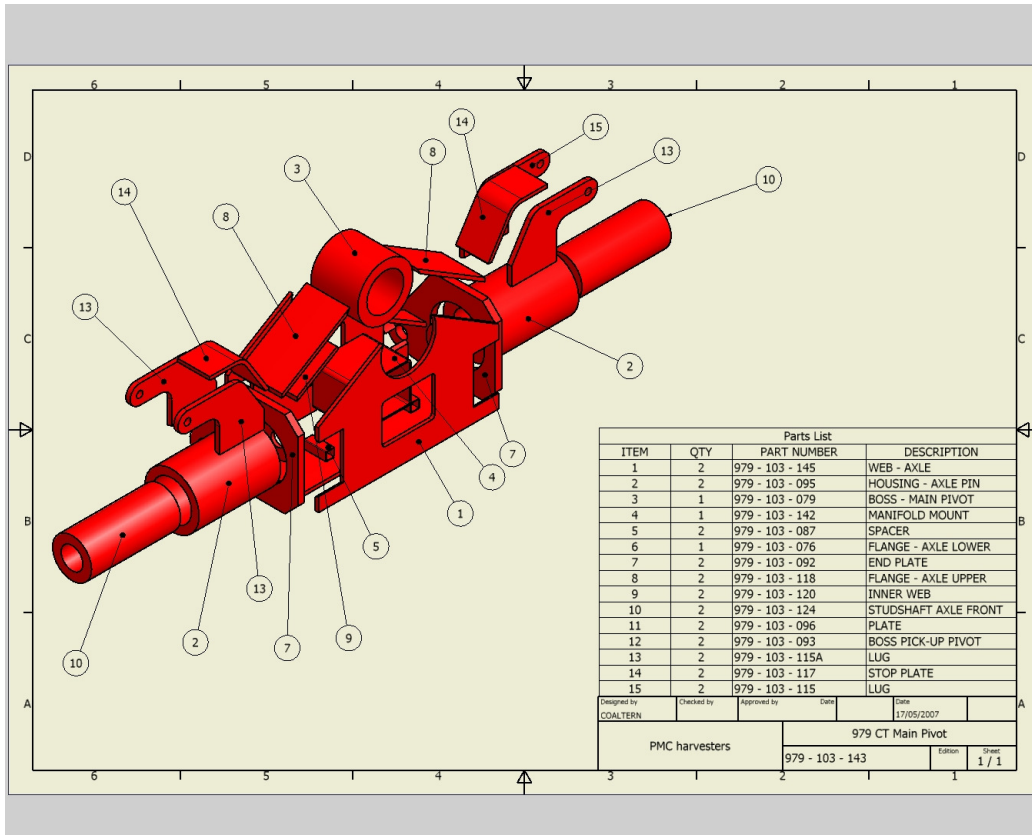


Figure 8.1: Exploded drawing sheet for 979 CT main pivot

The pivot, shown in Figure 8.1, is a 47 part welded assembly using MS 43A grade steel as the primary component material. Changes documented later in this section will utilise the descriptions shown in the Parts List shown in Figure 8.1.

8.2.1 Main Pivot Loading Criteria

The loads applied to the main pivot during analysis were as follows;

Maximum axle load	100 kN per side
Maximum thrust	41.25 kN per side
Levelling cylinder forces:	
Upwards	14.302 kN
Downwards	19.751 kN

Picking head forces:

Horizontal	36.8 kN
Vertical	56.8 kN
Side impact	7.75 kNm

For a comprehensive breakdown of the loading criteria and full calculations please see Appendix C, Section 15.1.

8.3 Main Pivot Development

8.3.1 Current Main Pivot

The standard PMC 979 CT main pivot weighs 541 kg. The main body is manufactured from 15 mm plate steel with an internal triangulation configuration connecting the axle pin housing to the main boss on either side.

8.3.2 Revision 1

Revision 1 of the main pivot prototype has a total mass of 488 kg. The mass reduction is due to a reduction in plate thickness on the main body of the axle with the specific details shown in Table 8.1.

Table 8.1: Design changes for main pivot revision 1

Description	Changes to Standard Parts
Web – Axle	Reduction in material thickness by 5 mm
Flange – Axle lower	Reduction in material thickness by 5 mm
End plate	Reduction in material thickness by 10 mm

8.3.3 Revision 2

Revision 2 has a total mass of 407 kg. It retained the original boss dimensions to allow fitment to the current chassis or the ability to be retro fitted to older machines. The main body of the main pivot has reduced plate thickness with the stub axles and housings reduced in overall diameter. Full design changes are listed in Table 8.2.

Table 8.2: Design changes for main pivot revision 2

Description	Changes to Standard Parts
Web – Axle	Reduction in thickness by 5 mm
Housing – Axle pin	Reduction to inner bore by 40 mm, reduction of 50 mm to outer bore
Flange – Axle lower	Reduction in material thickness by 5 mm
End plate	Reduction in material thickness by 10 mm
Flange – Axle upper	Reduction in material thickness by 5 mm
Stubshaft axle	Reduction to inner bore by 39 mm & reduction of outer bore by 39 mm
Boss pickup pivot	Reduction in material thickness by 20 mm
Lug	Reduction in material thickness by 5 mm, increase in lug length by 5 mm

8.3.4 Revision 3

Revision 3 has a total mass of 396 kg. This revision utilises all the changes made in revision 2, with further development in the following areas; main boss is the same diameter as the stub axles and the axle web has been modified to accommodate the smaller boss whilst retaining the original geometric position of the boss centre in the axle web. The manifold mount was evolved with larger radii corners. Table 8.3 documents the design changes.

Table 8.3: Design changes for main pivot revision 3

Description	Changes to Standard Parts
Web – Axle	Reduction in thickness by 5 mm
Housing – Axle pin	Reduction to inner bore by 40 mm, reduction of 50 mm to outer bore
Boss – Main pivot	Reduction to inner bore by 40 mm & reduction of outer bore by 40 mm
Flange – Axle lower	Reduction in material thickness by 5 mm
Manifold mount	Corner radii increased to 50 mm
End plate	Reduction in material thickness by 10 mm
Flange – Axle upper	Reduction in material thickness by 5 mm
Stubshaft axle	Reduction to inner bore by 39 mm & reduction of outer bore by 39 mm
Boss pickup pivot	Reduction in material thickness by 20 mm
Lug	Reduction in material thickness by 5mm, increase in lug length by 5 mm

8.4 Rear Axle

The 979 CT rear axle, shown in Figure 8.2, is a 25 part welded assembly. It is constructed of MS 43A mild steel with the main structure having plate thicknesses of 12 mm and 15 mm. Changes documented later in this section will utilise the descriptions shown in the Parts List shown in Figure 8.2.

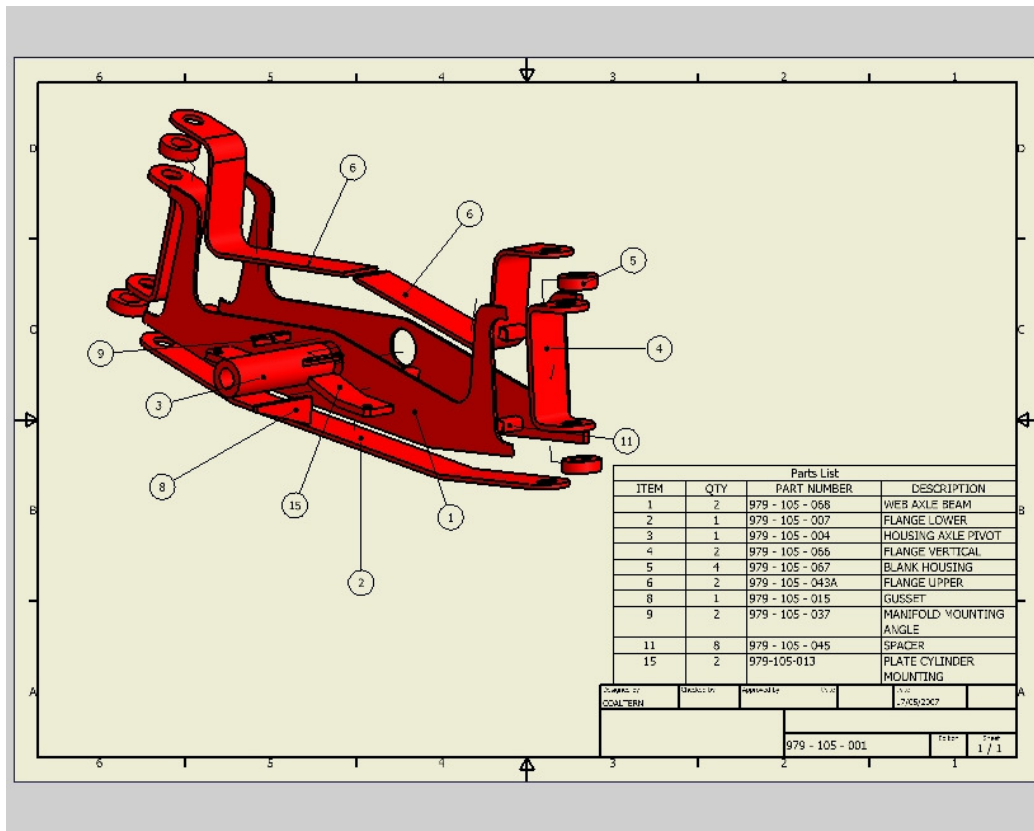


Figure 8.2: Exploded view of 979 CT rear axle

8.4.1 Rear Axle Loading Criteria

The loads applied to the rear axle during analysis were as follows;

Maximum axle load	50 kN per side
Maximum thrust	20.620 kN per side
Maximum steering cylinder force	120.6 kN
Vertical flange moment	25.7 kNm
Side impact	5.3 kNm

For a comprehensive breakdown of the loading criteria and full calculations please see Appendix C, Section 15.1.

8.5 Rear Axle Development

8.5.1 Current Rear Axle

The standard PMC 979 CT harvester rear axle has a mass of 304 kg. The axle is mounted to the rear levelling frame by means of a pin located through the axle pivot, thus restricting longitudinal movement. The wheel motor yokes are located between the faces of the vertical flanges and then held in place with two king pins.

8.5.2 Revision 1

Revision 1 of the rear axle has a total mass of 195.5 kg. The reduction in mass is achieved by reducing plate thickness in the main body with the single biggest reduction achieved by reducing the wall thickness of the axle pivot housing. Table 8.4 lists the design changes.

Table 8.4: Design changes for rear axle revision 1

Description	Changes to Standard Parts
Web axle beam	Reduction in material thickness by 2 mm, hole diameter reduced from 126 mm to 95 mm.
Housing axle pivot	Outer bore reduced to 95 mm
Flange vertical	Reduction in material thickness by 5 mm
Plate cylinder vertical	Reduction in material thickness by 10 mm.

8.6 Main Chassis

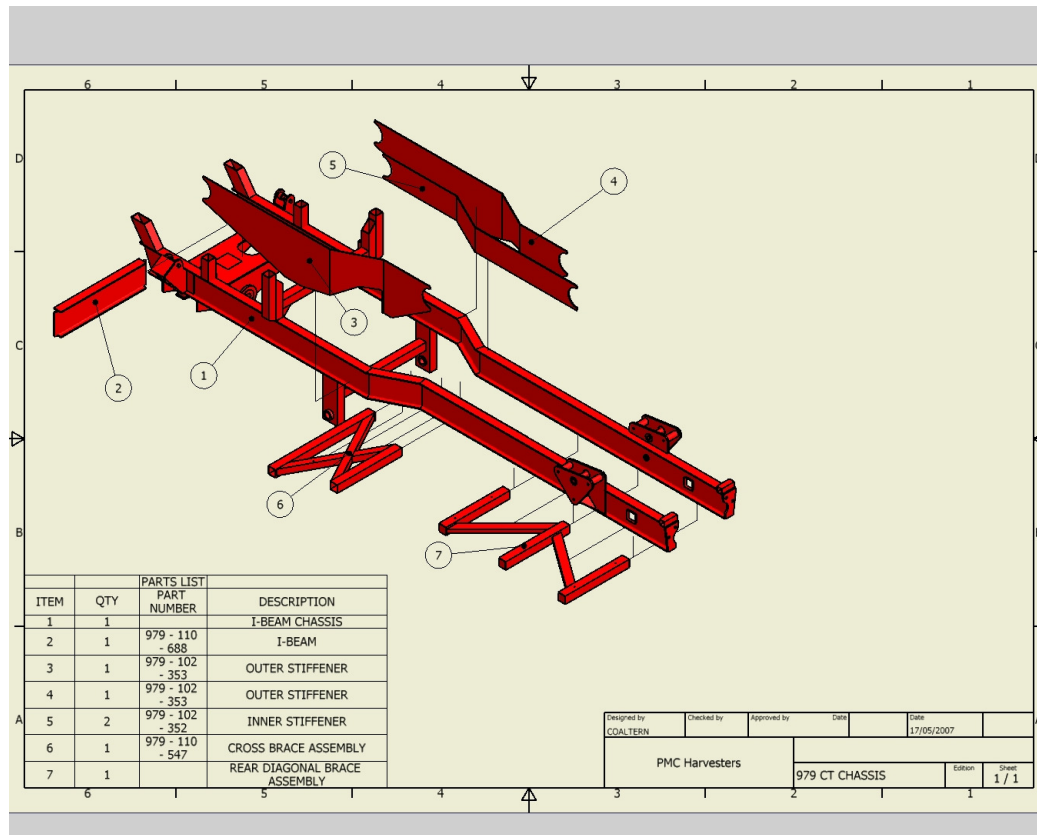


Figure 8.3: Exploded drawing of 979 CT chassis

The chassis, as shown in Figure 8.3, is built from six BS 4360/43A steel I-beams welded together. The chassis is restrained laterally by five sub-assemblies, they are as follows:

1. Front axle pivot welded to the underside of the front main rails.
2. I-beam brace welded between the front main rail I-beams.
3. Stiffening plates welded along each side of the I-beam structure extending approximately 1.5m forward and 2m rearward of the “dog leg”.
4. Forward of the “dog leg”, the rear levelling mount frame is welded to the underside of the rails and vertically to both rail stiffeners.
5. Two diagonal braces underpinned to the chassis main rails, one at the “dog leg” and one along the rear main rails at the back of the machine.

Changes documented later in this section will utilise the descriptions shown in the Parts List shown in Figure 8.3.

8.6.1 Main Chassis Loading Criteria

The loads applied to the main chassis during analysis were as follows:

Main pivot vertical load	200 kN
Front levelling loads:	
Upwards	14.3 kN
Downwards	19.75 kN
Rear levelling loads:	
Back up	42.9 kN
Back down	106 kN
Thrust	123.72 kN

For a comprehensive breakdown of the loading criteria and full calculations please see Appendix C, Section 15.1.

8.7 Main Chassis Development

8.7.1 Current Main Chassis

The current CT chassis, as shown in Figure 8.3, has a mass of 1425kg, and uses I-beams to provide strength with considerable under bracing to offer lateral stability. Although I-beams offer a good longitudinal weight/strength ratio, laterally they are very weak, due to the web dimensions. Another problem associated with the I-beam structure within the PMC application is cleanliness; the machines are used by the food industry and as such fall under strict hygiene regulations. The underside of an I-beam flange is awkward to clean and thus requires a more timely washing process. The extended washing process incurs greater expense for the grower. It was decided a

chassis made from box section could offer a valid solution to counteract these problems.

8.7.2 Revision 1

Revision 1 has a total mass of 1270 kg. The main rails of the chassis were created from 7 mm thick box section and the I-beam cross brace was replaced with 7 mm wall box section. The stiffeners were removed and instead triangulation plates fitted to support the rear levelling frame mount. The cross braces on the titanium underside were redesigned to fit between the rails and their overall span was increased, therefore increasing the level of triangulation for the rear of the chassis. Design changes are documented in Table 8.5.

Table 8.5: Design changes for standard chassis revision 1

Description	Changes to Standard Parts	New Parts
I-beam chassis	Replaced	7mm box section structure
I-beam	Replaced	7mm box section structure
Outer stiffener	Removed	
Outer stiffener	Removed	
Inner stiffener	Removed	
Cross brace assembly	Elongated and relocated 150 mm vertically above original position	
Rear diagonal brace assembly	Relocated 150 mm vertically above vertical position	

8.7.3 Revision 2

Revision 2 has a mass of 1162 kg and utilises the same box section configuration as revision 1, however the rearward brace network has been modified. The “dog leg” brace assembly has been designed to accurately span the “dog leg”, therefore offering additional bracing at the joints and generating a triangulation centre in the middle of

the “dog leg”. The rear brace has been extended slightly making the triangulation support bigger, thus covering more distance. Both brace assemblies have been moved back to their original under pinning position as the higher position in revision 1 would require modification of the long pea conveyor within the machine. Design changes are documented in Table 8.6.

Table 8.6: Design changes for standard chassis revision 2

Description	Changes to Standard Parts	New Parts
I-beam chassis	Replaced	7 mm box section structure
I-beam	Replaced	7 mm box section structure
Outer stiffener	Removed	
Outer stiffener	Removed	
Inner stiffener	Removed	
Cross brace assembly	Designed to fit "dog leg"	
Rear diagonal brace assembly	Located in "original" vertical position	

9 Results & Discussions – FEA

9.1 Main Pivot

9.1.1 Peak Stress Analysis

Initially the main pivot assembly and proposed revisions were evaluated by comparing the equivalent peak stress values predicted using Ansys 10. Using peak stress values as a definitive guide for component design would be a naive design practice; the peak values returned by a solver within any analysis package can be influenced by modelling idiosyncrasies, such as geometry characteristics, rate of change in material cross section, mesh refinement, nodal intensity and restraint method. However, as an initial guide to the performance of a part or assembly the results can be very informative.

Table 9.1: Peak stresses measured on the four front axle models

	Loading Criteria			
	Static	Static Level	Picking Head Up	Worst Case
Axle	Equivalent Peak Stress (MPa)			
Standard	86.59	112.57	117.18	151.36
Revision 1	131.28	132.28	141.90	155.14
Revision 2	151.20	193.28	207.02	223.94
Revision 3	93.15	132.13	109.22	137.73

Peak stresses calculated by Ansys 10 are shown in Table 9.1. From appraisal of the values, it is apparent that as the number and magnitude of loads exerted increased so did the magnitude of the peak stresses. The changes to the main pivot involved one or more of the following features – reduction in material thickness, reduction in boss diameter and reduction in stub axle diameter. These results agree with the accepted knowledge that if the overall geometric shape, loading criteria and material remain constant but the material thickness is reduced then the strength of a component will be reduced and thus stresses within the component will increase. However, what can be noted from this initial review is that the highest level of increase in peak stress from the static to maximum loading scenarios occurs in the standard main pivot. Quantification of the gains revealed the standard main pivot peak stress increased by

74.8% from static to worst case whilst peak stresses in Revision 3 increased 47.8% from static to worst case.

9.1.2 Preliminary Analysis of the Main Pivot

The underlying structure of the main pivot can be approximated by an isosceles triangle, utilising the two stub axles and the main boss as the three corners of the triangle. In normal operating conditions the dominant forces are exerted equally on the stub axles in a uniformly distributed format and the main body of the boss offers lateral resistance, with the boss faces offering longitudinal resistance to the loads. If the main pivot is treated as a simple triangle as shown in Figure 9.1, it can be said that the upper flanges will be under compression load and the material below the centre of the stub axles will be in tension.

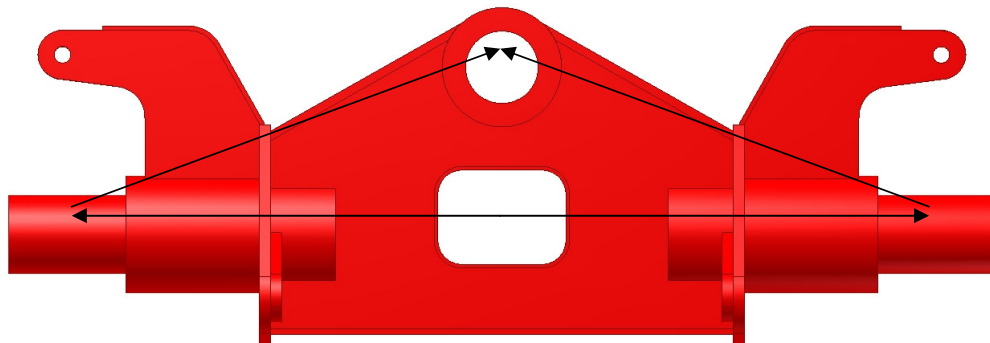


Figure 9.1: Triangulation of forces

However, the main pivot is a complex assembly with an additional four loads exerted on it, therefore under normal working conditions it is subjected to a range of forces acting in different directions. Breaking the main structure down we see the stub axles are of tubular design; therefore they have a neutral axis upon which no stress acts. The combined length of the two stub axles is 60% of the overall main pivot width and as the main pivot's overall structure takes the form of a box the neutral axis can be projected across the pivot width until it reaches the return manifold, situated in the

middle of the axle web. In general the material below this neutral axis of this assembly will be subjected to tensional stress. The underside of the stub axles, lower axle web and lower flange are subjected to these effects with the lower flange enduring the largest magnitude due to its geometrical position from the neutral axis. Similarly, compression loads are found above the neutral axis of the stub axle with the upper flanges subjected to the largest compressive forces.

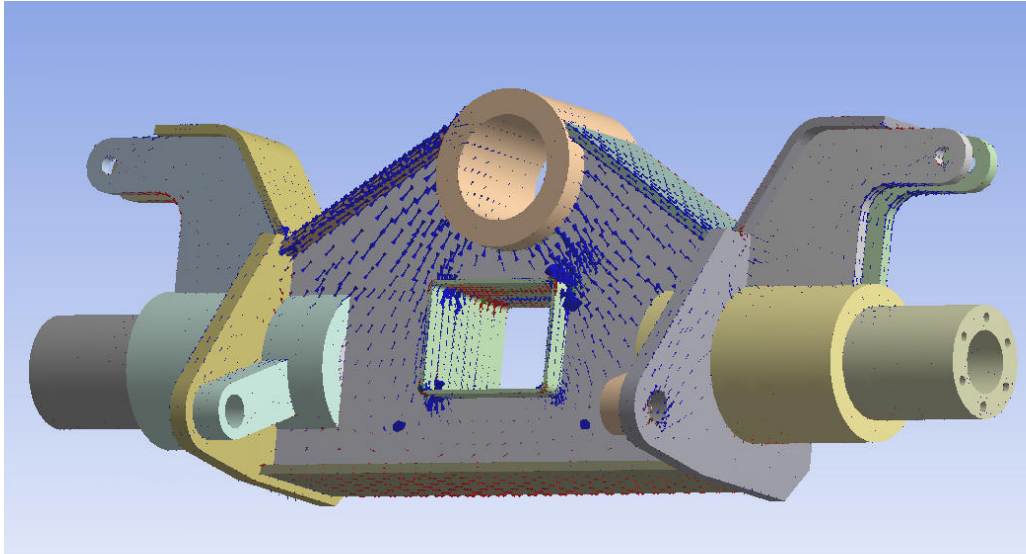


Figure 9.2: Equivalent stress vectors distribution

Further analyses of the main pivot show the complexity of the force and therefore stress distribution. Figure 9.2 shows the stress distribution within the axle under “normal” loading criteria. Blue arrows depict areas of high stress and red area show low/medium stress. It can be seen that the upper flange and main boss have both the highest magnitude and greatest concentration of stress. Close observation of the lower flange reveals the stress vectors originate from the centre and progress to either end. As this is a normal loading situation the stress vectors can also be seen in the picking head and levelling lugs areas. Overall, Figure 9.2 gives a good representation of the propagation of stress vectors within the main pivot and thus offers guidance on the critical areas within the main pivot.

9.1.3 Analysis of Sectioned Main Pivot

As mentioned in Section 9.1 peak stress should not be taken as a complete measure of how a body reacts under load. Instead the body should be manipulated such that areas of higher stress are thoroughly examined. This manipulation can be seen in Figure 9.3 and Figure 9.4.

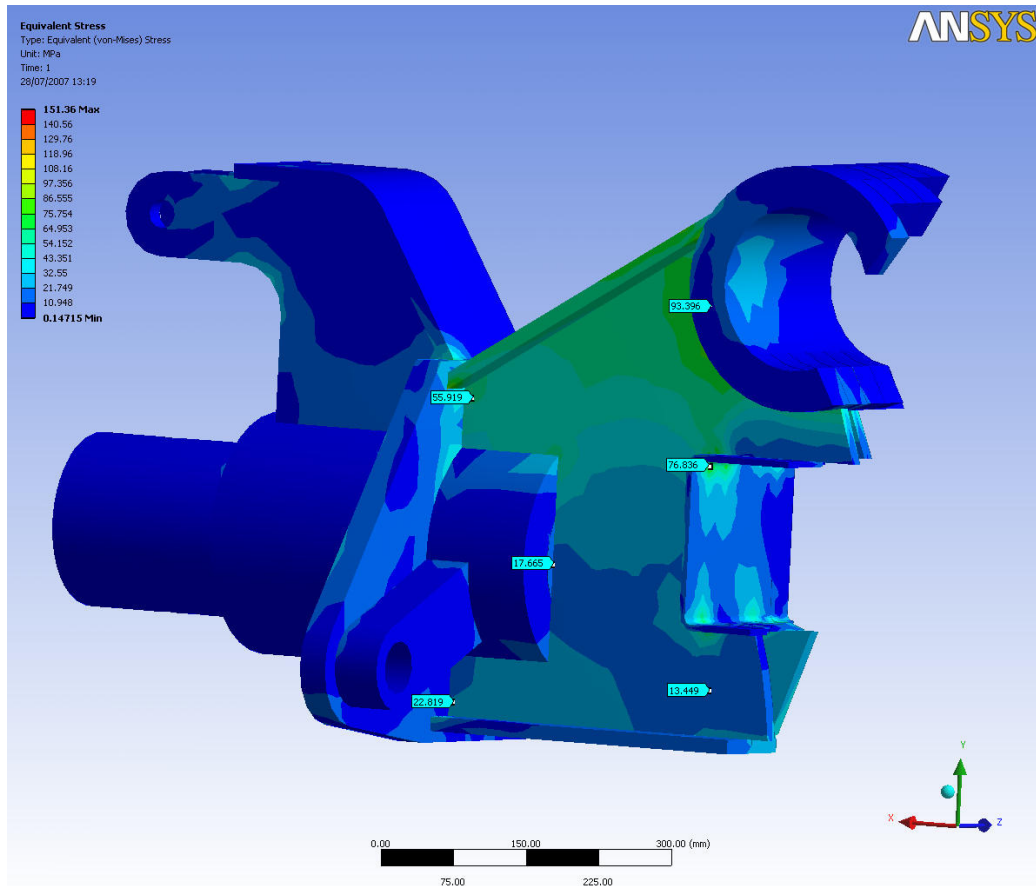


Figure 9.3: Sectioned view of standard main pivot under maximum loading criteria

Figure 9.3 shows that the upper part of the assembly is subjected to equivalent stress levels in the region of 55 MPa – 95 MPa, with the lower flange having a stress level of 20 MPa, this dominance in stress distribution and magnitude in the upper region concurs with the stress distribution in Figure 9.2. It can also be seen that the stub axle is subjected to the lowest level of stress in the whole structure with stress levels on the axle web directly inline with the stub axle neutral axis being in the magnitude of 18 MPa.

The stub axle used on this standard main pivot has dimensions as follows: 180mm x 40mm x 410 mm. Using basic bending theory and assuming the stub axle is a simple cantilever beam with a uniformly distributed load exerted on it, for an operating UTS of 200 MPa, it can be calculated that the stub axle's maximum permissible bending moment capacity is 25 times greater than that actually exerted upon it, therefore this single item is extremely over engineered (full calculation can be found in Appendix C, Section 15.1). If it is then considered that the stub axle has a bearing fitted the magnitude of deformation would also require to be reviewed in order to maintain the bearing life cycle. When the equivalent stress predicted in the stub axle is 18 MPa a deformation of 0.2 mm is seen.

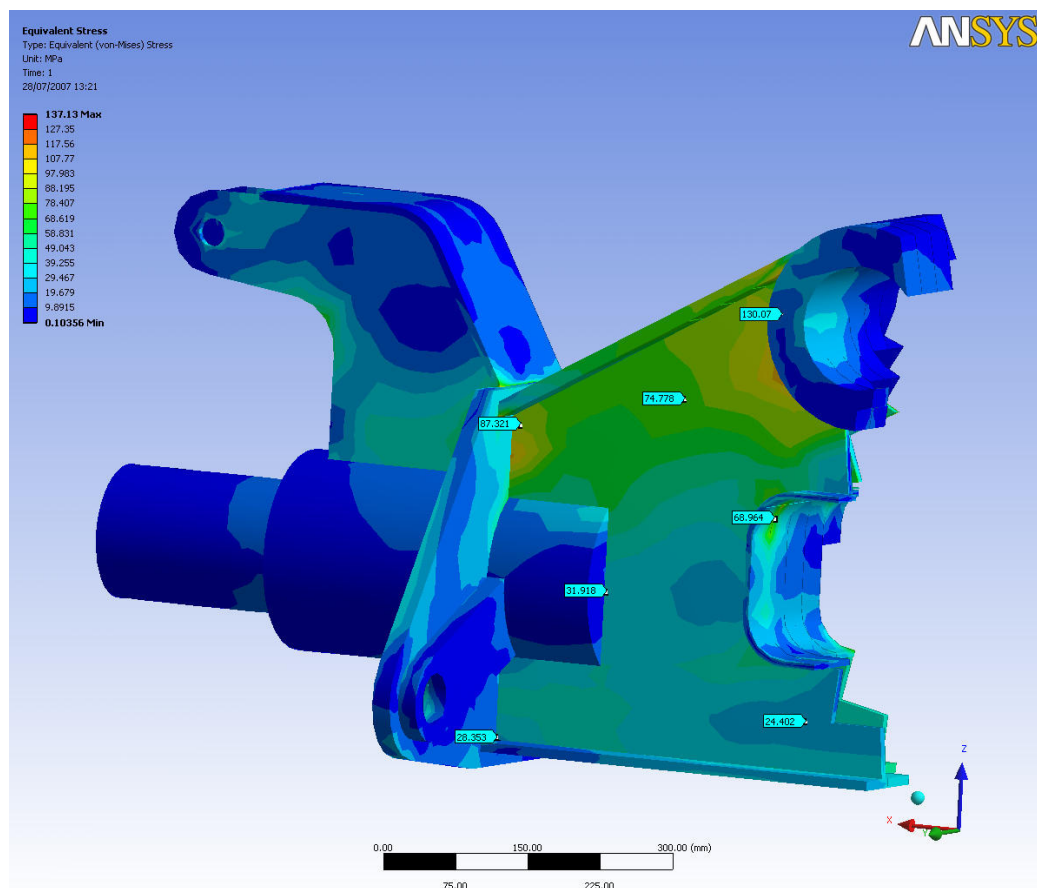


Figure 9.4: Sectioned view of the main pivot - revision 3 under maximum loading criteria.

In contrast to the standard main pivot, revision 3 shows a more even stress distribution, albeit at higher levels. The upper region of the axle web close to the

upper flange has a relatively uniform stress distribution running at the angle set by the flange. The stress recorded is in the range of 70 – 130 MPa, with the higher values close to the joint of the main boss, axle web and upper flange. The stress below the neutral axis of the stub axle is also increased, with values up to 90% higher than those in standard main pivot. A worthy point to note is the reduction in stress at the return manifold/axle web interface. In this revision the manifold has had the corner radii increased and therefore a reduction is observed in stress levels at the corner. Additionally, all values retrieved from the analysis are below 132 MPa and therefore are 37%, or less, of the normal UTS of mild steel.

9.1.4 Comparison of Values

Figure 9.3 and Figure 9.4 have probe readings showing the stress at various points on the main pivots. These readings are representational and are not located in precisely the same location on the axle, as the location may no longer exist, however they do offer good guidance on stress changes between the models. Table 9.2 shows the values obtained and accounting for only the increase in stress, it can be concluded that, on average, Revision 3 has stresses 51.5% higher than the standard main pivot, however the peak stress is 9.5% lower for revision 3 and the life expectancy due to fatigue for revision 3 is 43.5% longer than that of the standard main pivot.

Table 9.2: Standard and revised main pivot stress comparison

Equivalent Stress (MPa)		% Rate	Type
Standard Main Pivot	Revision 3 Main Pivot		
22.820	28.353	24.25	Increase
13.449	24.402	81.4	Increase
17.665	31.918	44.6	Increase
78.836	68.966	12.5	Decrease
55.919	87.321	56	Increase
93.396	130.017	39	Increase

9.2 Rear Axle

9.2.1 Peak Stresses

The peak stresses found for the standard and revised rear axle are shown in Table 9.3.

Table 9.3: Peak stresses measured on the standard and revised rear axle

	Loading Criteria		
	Minimum	Normal	Maximum
	Equivalent Peak Stress (MPa)		
Standard Axle	171	204	227
Revision Axle	241	286	309

Table 9.3 clearly shows that the revised axle has the highest peak stress values across the test range. As mentioned in Section 9.1 peak stress should only be used as a guide for initial review. Further investigation of the values shown in Table 9.3 highlight that the peak stress occurs at interfaces between component parts where material thickness changes. Reviewing the results for the maximum loading criteria it can be concluded that the revised axle has a peak stress increase of 36%, which, occurs at the joint between the axle web and a spacer. The spacer in a normal axle build would be tacked in place, in combination with the loading criteria applied to the axle in this test, it is apparent that the result is misleading as the axle cannot be undergoing the quoted stress in these conditions at that point. Therefore the values for peak stress in this testing process shall be treated with caution and greater emphasis put on the detailed studies.

9.2.2 Preliminary Analysis of the Rear Axle

The rear axle is configured in a similar way to the main pivot and is mounted centrally through the pivot. Unlike the main pivot it does not have stub axles, instead it uses yokes to mount the hydrostatic wheel motors. The yoke is located in line with the vertical flange and between the two kingpins. The rear axle analysis does not include a study of the motor yoke as it does not form part of the fabricated structure.

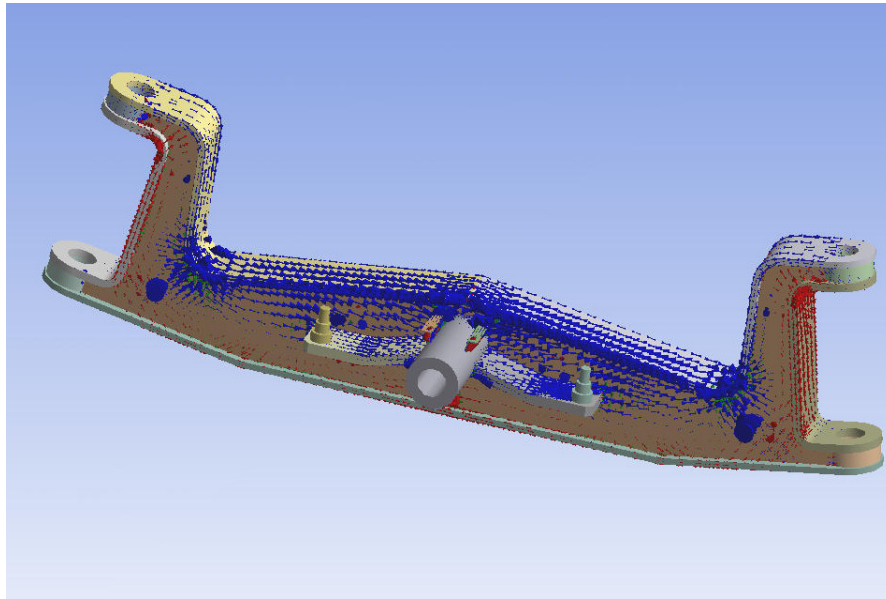


Figure 9.5: Force vector plot of the axle when under a normal static load condition

As shown in Figure 9.5 the dominant forces in the rear axle during normal loading are generated by the wheel loads. The wheel load is applied to the vertical flange therefore generating a compression force on the upper flange and thus causing the potential for a high stress concentration at the transition between vertical and horizontal planes in the upper flange. The lower flange spans the width of the rear axle and opposes the stress in the upper flange therefore it is subjected to tensional force components.

9.2.3 Analysis of Sectioned Rear Axle

Figure 9.6 and Figure 9.7 show sectioned views of the standard and revised axle respectively. The probe tool which obtained the values shown in Figure 9.6 and Figure 9.7 was not located at precise points for reasons mentioned in Section 9.1.4 and thus the generated values offer a representative view of the stress values obtained for both axles under the same maximum loading criteria.

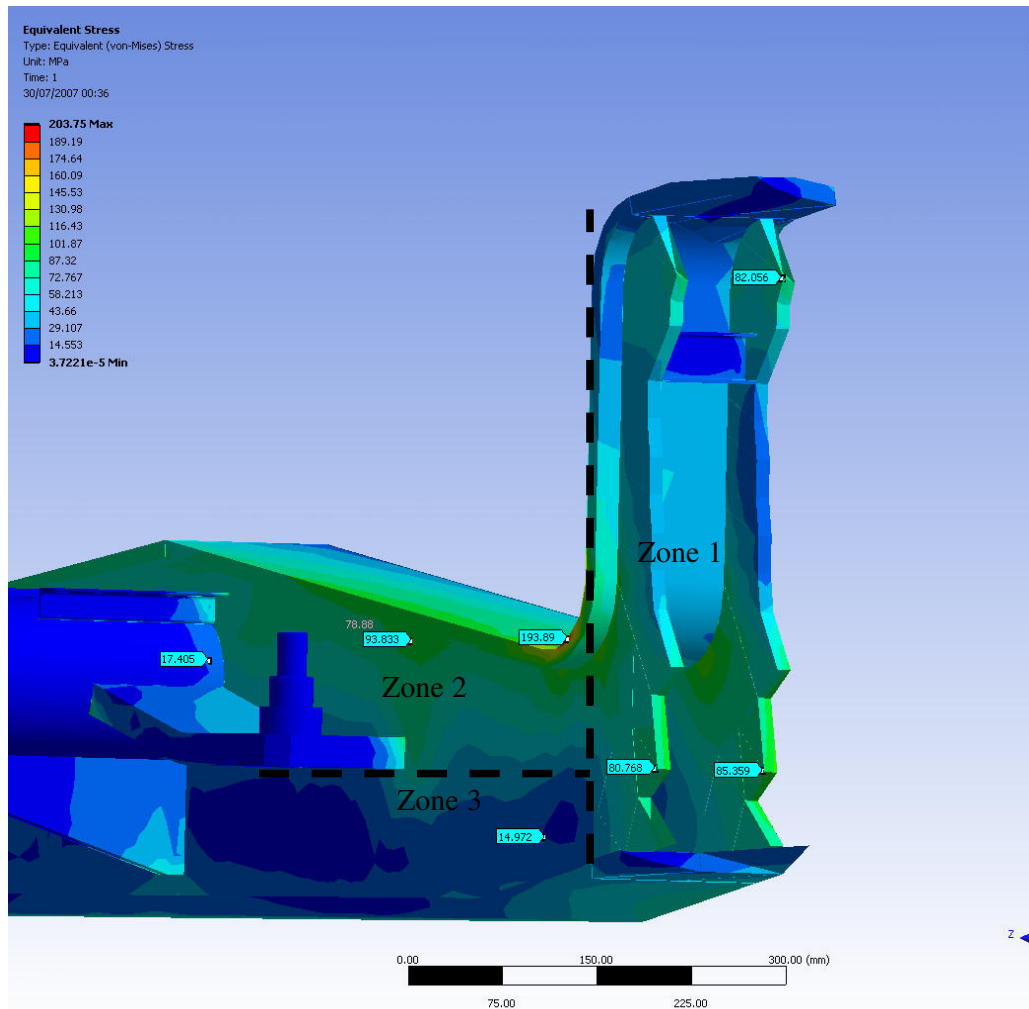


Figure 9.6: Sectioned view of the standard rear axle

The standard rear axle can be split into three stress zones, vertical flange, upper flange and lower flange. The sectioned view of the vertical flange (zone 1) shows the spread is relatively uniform with a nominal value of 85 MPa recorded for the upper regions of the vertical flange. The upper flange and upper axle web (zone 2) show the highest stress values in the axle. At the transition between vertical and horizontal planes on the upper flange a value of 194 MPa is recorded. As the distance from the transition increases the stress level subsides, however values of >90 MPa are still recorded above the main pivot. Below the axle centre line (zone 3) the stress levels are much lower, with the value shown in Figure 9.6 being 15 MPa. The lower flange does have higher levels of stress than the lower part of the axle web, however these levels are much lower than the upper web and upper flange.

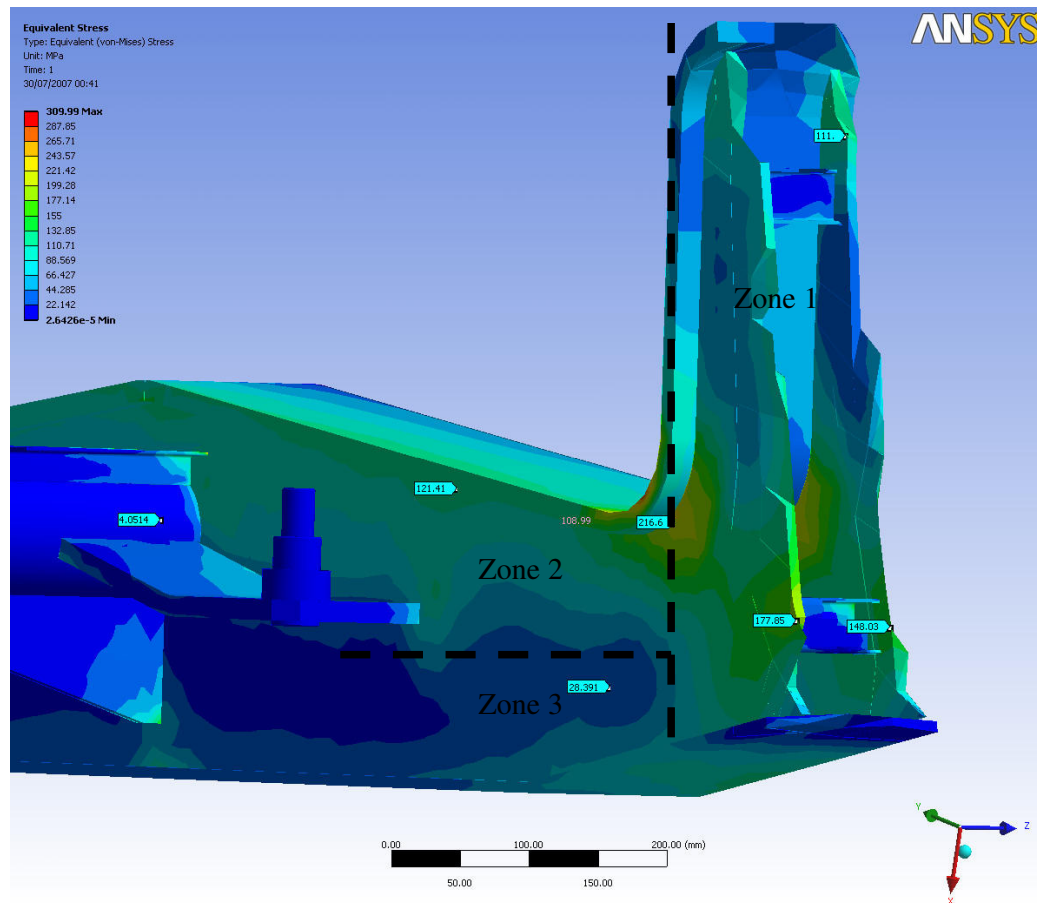


Figure 9.7: Sectioned view of the revised rear axle

The revised axle has a much higher stress level across the whole unit. The revised axle can also be defined into three parts. Zone 1 on revision 1 exhibits a wider spectrum of stress, which is on occasion 90.5% higher than that of the standard axle. Zone 2 shows stress values of approximately 30 MPa greater in magnitude than that of the standard axle across its length. Zone 3 of the axle web also has stress values in the order of 100% greater. Although some of these values are 120% greater, they do still lie within acceptable levels with respect to the UTS of mild steel.

9.2.4 Comparison of Values

A note should be made that both axles show low stress levels in their respective main pivots, ~20 MPa which suggests that the main stress dissipation occurs at a considerable distance from the pivot point. Table 9.4 shows the representational

values for both axles. Comparing these readings it can be concluded that the overall stress level increase is 55.6% for the revised axle over the standard axle with the life expectancy for this revision being 67% lower than the standard axle.

Table 9.4: Standard and revised rear axle peak stress comparison

Equivalent Stress (MPa)		% Increase	Type
Standard Rear Axle	Revised Rear Axle		
17.4	19	9.2	Increase
93.8	121.41	29.4	Increase
14.9	28.39	90.5	Increase
193.9	216.6	11.7	Increase
80.7	177.8	120.3	Increase
85.0	148	74.1	Increase

9.3 Main Chassis

9.3.1 Peak Stresses

Table 9.5 shows peak stress for all main chassis analyses. As stated in Section 9.1, peak stress should only be used as a guide; however, the results for revision 2 are interesting. On 3 out of the 5 tests the revised chassis outperforms the standard chassis, with the differences between test 4 and 5 being relatively small ($\leq 15\%$). Revision 2 is designed utilising RHS (rectangular hollow section) for the main structure whereas the standard chassis uses I-beams plated on either side. In all the tests in which the box section surpassed the I-beam machine, levelling was involved; (application of chassis twist), therefore, on preliminary inspection the box section appears to offer enhanced performance on 60% of the test scenarios.

Table 9.5: Peak stresses measured on the standard and revised main chassis

Peak Stress (MPa)	Standard Chassis	Revision 1	Revision 2
Maximum	292.44	460.14	260.84
Back Up	293.18	316.77	183.99
Back Down	282.12	328.39	274.42
Full Forward	237.62	262.94	243.41
Static	159.98	188.59	183.94

9.3.2 Preliminary Analysis of the Main Chassis

The PMC 979 CT chassis is a relatively simple structure utilising commercially available steel sections fabricated using conventional MIG welding. The load application occurs at seven points through four main structural networks. The harvester has longitudinal (fore/aft) and lateral (side/side) levelling, thus the chassis is subjected to high torsional strains.

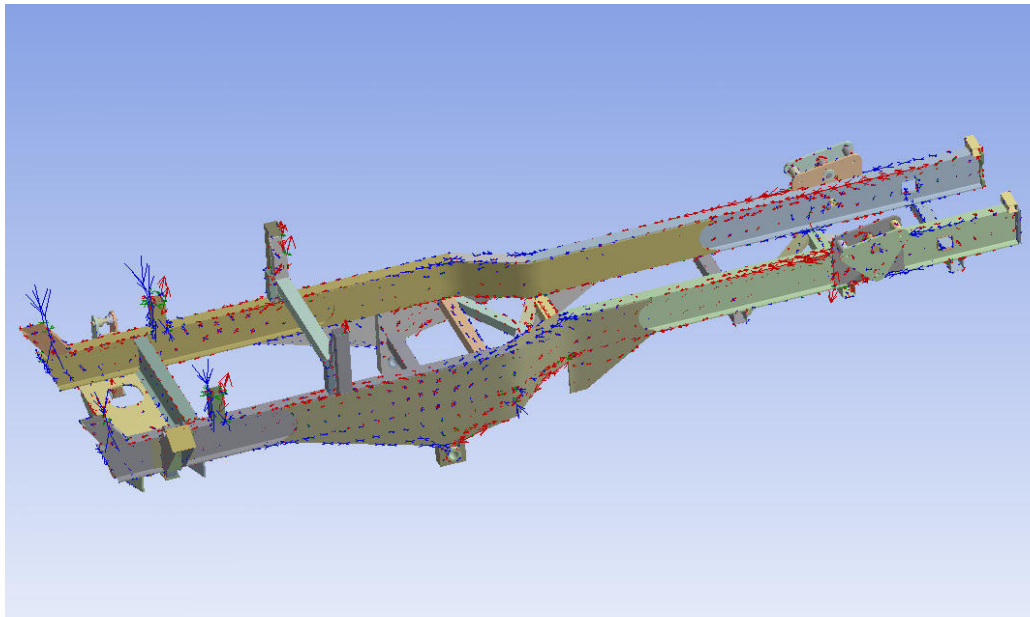


Figure 9.8: Stress vectors in standard main chassis during normal loading

In Figure 9.8 the stress vectors show relatively small areas of high stress concentration near all loading interfaces with long sections of the chassis under minimal stress; an example of such a low stress section is the main rail rearward of the dogleg.

9.3.3 Analysis of Sectioned Main Chassis

The base chassis of the PMC 979 CT Harvester is of considerable proportions, 1.5 m x 1.5 m x 7 m; consequently Ansys screen prints of the whole chassis are unsuitable as the key areas of interest are not clearly visible, therefore subsequent figures will show only sectioned views of the chassis.

9.3.3.1 Standard Chassis – Dog Leg

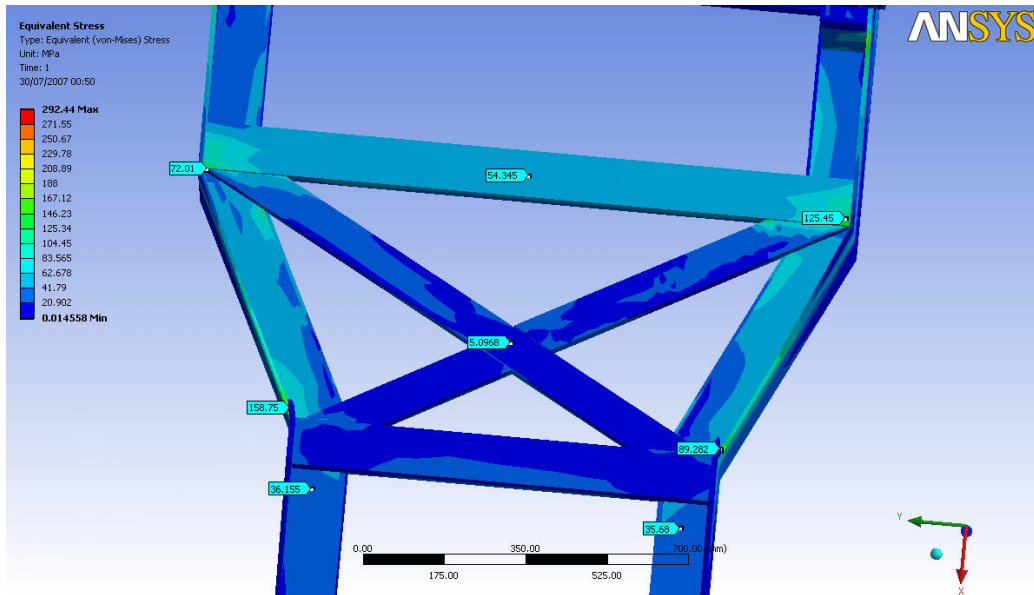


Figure 9.9: Cross brace network located on the underside of the current main chassis dogleg

Reviewing the stress distribution in the cross brace box section, I-beams and gusset plates, shown in Figure 9.9, it can be seen that localised stress peaks form at the joints with the distribution of stresses in the cross brace being relatively low. At the centre of the cross brace a stress value of 5 MPa is shown, whereas 125 MPa is shown on the upper right section of the brace, this comparison demonstrates that the difference in structural activity is vast. The stress transfer from the gussets on either side of the dog leg to the main rails is also low, a value of 285 MPa is noted on the inside face of the outer gusset and yet a point on the I-beam 10 mm away is only 158 MPa, therefore the gusset is absorbing the majority of the stress. Overall, from Figure 9.9, it can be stated that due to changes in geometry, material cross-section and shape that the natural flow of stress within the structure is disturbed and thus localised stress peaks are inevitable

9.3.3.2 Revision 2 – Dog Leg

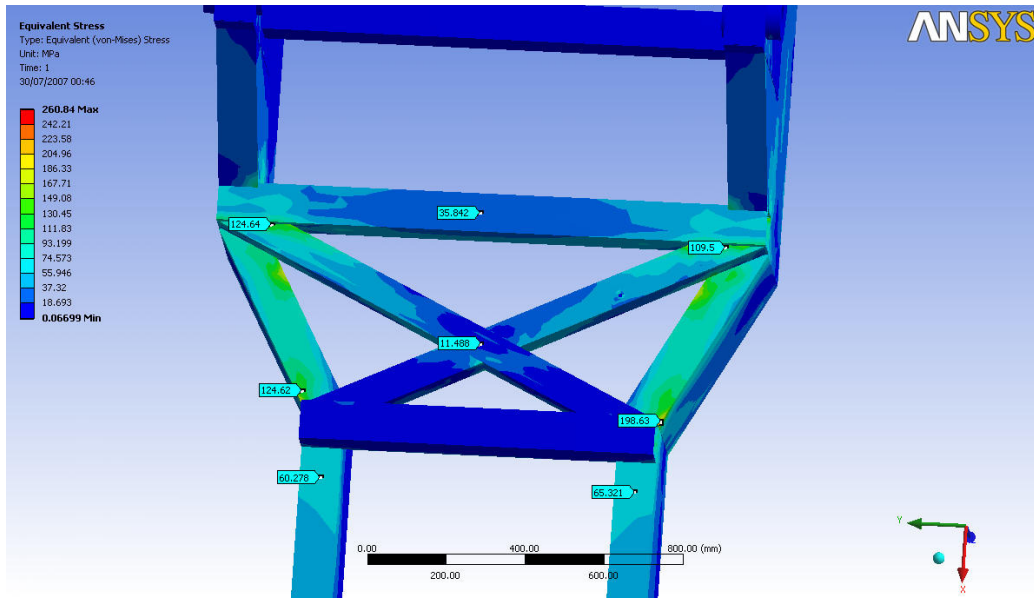


Figure 9.10: Cross brace network located on the underside of the revision 2 main chassis dogleg

The revision 2 chassis, as shown in Figure 9.10 has been designed using RHS as the main structural component; please refer to Section 7.3 for a complete breakdown on revision 2. The standard chassis is constructed from I-beam which has been plated either side; revision 2 mimics this design but without the centre web found in the standard chassis. The cross brace has also been adapted to fit the dog leg, rather than being offset. The stress levels in the dogleg are higher than that seen in the standard chassis; however no area exceeds 200 MPa with the highest stresses found close to weld joints. The centre of the cross brace is also subjected to higher stress levels therefore it can be noted that the brace is offering more rigidity to the structure. The levels of stress along the main rails are also greater in this box section design.

9.3.3.3 Standard Chassis – Levelling Structure

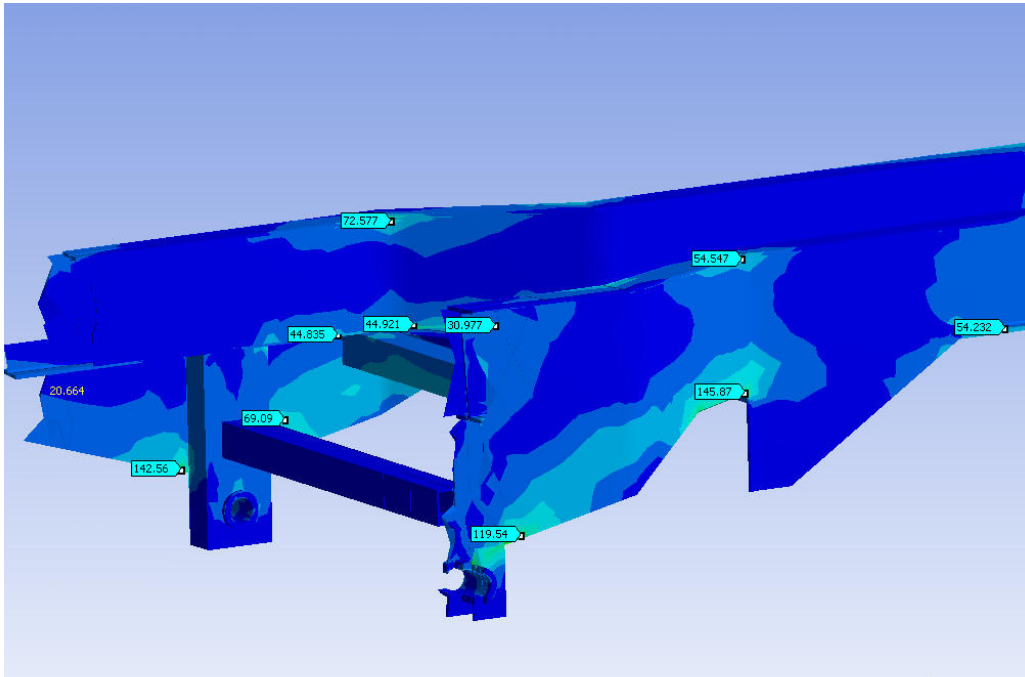


Figure 9.11: Standard chassis showing levelling structure under load

Reviewing each of the main components in the chassis allows a better understanding of how the stress distribution forms through these members. Figure 9.11 shows the wide range of stress (20.7 MPa – 145.9 MPa) recorded in the main chassis under loading. The LHS outer gusset is clearly working well with the triangulation taking stress away from the levelling frame and directing it back into the chassis. Looking at the gusset we see that the lower tip experiences lower stress due to the linearity of force vectors. Another important point to note is the performance of the gusset at the cut-out for the rear levelling frame/axle. Rearward of the levelling frame cut-out and below the lower part of the main rail the gusset offers minimal additional strength. The peak which occurs at this transition point between the gusset and rail is strongly influenced by the severe change in material section at this point. This change produces a high stress concentration and diminishes the effective stress dispersal gained by gusseting the structure. Looking rearward of this point on the LH chassis rail we see a low stress on the outer gusset with higher levels of stress appearing further down the rail. Reviewing the RH inside gusset and main rail it is clear that the structural member is now working as if it were RHS, with a neutral axis appearing along the whole length of the inside gusset. The cross brace network also appears to

be working at a lower than desired level which puts more pressure on the main chassis network. This occurs because the braces are mounted both forward and rearward of the dog leg, therefore tying the rails together. However at the critical changes in profile of the dog leg, the braces, with their offset format, do not offer maximum resistance to the torsional effects and thus make the main rails endure higher levels of stress.

9.3.3.4 Revision 2 – Levelling Structure

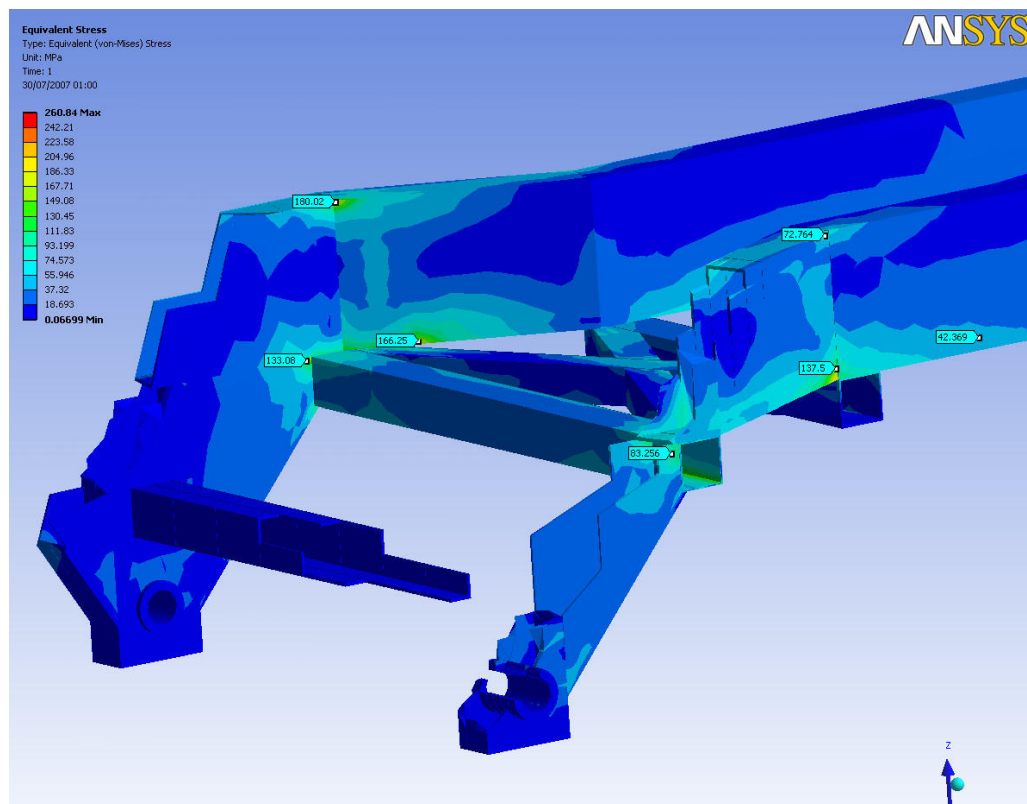


Figure 9.12: Revision 2 main chassis showing levelling structure under load

Looking at Figure 9.12 we see a more even stress distribution across the structure when compared to Figure 9.11. The level of stress seen at the rear face of the dogleg on the LH main rail is 6% less than that on the standard main chassis. The stress along the length of the main rails has also decreased in magnitude in the critical areas; however they have increased in spread and can be noted to engulf more of the steel work. An improved utilisation of the cross brace at the centre of the dog leg can also

be seen in revision 2 with the severity and consumed area increased but still within the desired maximum stress for the design criteria. The overall level of stress in the structure in the key areas of the main chassis is lower than that of the standard chassis with levels of <200 MPa being predicted.

9.3.4 Comparison of Values

Tables 9.5 and Table 9.6 show probe readings for the stress at various points in the main chassis and its revisions. As with previous work these readings are representational and are not located on precisely the same point, as the particular point may no longer exist. The trend evident from the readings in both tables demonstrates that revision 2 of the main chassis out performs the current main chassis in the majority of tests. The peak stress seen in revision 2 is 10.8% lower than that in the main chassis and also falls within an acceptable maximum stress level of 260 MPa - 74% of the materials UTS. Using Ansys to predict the life expectancy of the revision 2 main chassis it can be noted that this chassis has a 42.6% longer working life span prediction with respect to fatigue than the main chassis, which when coupled with a 18.4% reduction in weight results in a chassis which is performing better and utilising more of its inherent strength.

Table 9.6: Standard and revised main chassis equivalent stress comparison

Equivalent Stress (MPa)		% Rate	Type
Standard Chassis	Revision 2 Chassis		
5.09	11.489	125.72	Increase
89.28	198.63	122.48	Increase
72.01	124.64	73.09	Increase
145.87	137.5	5.74	Decrease
54.55	72.76	33.38	Increase
54.23	42.37	21.87	Decrease

The shear stress generated in the Revision 2 chassis is also of an acceptable level, reviewing Table 9.7 it can be seen that Revision 2 produces shear levels of a similar magnitude to the standard chassis with both increases and decreases in actual values over the entirety of the structure. The average increase in shear stress in the structure is 45%; however peak shear is reduced by 28%.

Table 9.7: Shear stress comparison between standard and revision 2 chassis.

Shear Stress (MPa)		% Rate	Type
Standard Chassis	Revision 2 Chassis		
23.29	27.3	17.22	Increase
45.1	42.8	5.10	Decrease
2.99	5.57	86.29	Increase
12.58	29.06	131.00	Increase
2.97	4.71	58.59	Increase
46.1	38.5	16.49	Decrease

A final check of Revision 2 chassis can be made by looking at the deformation generated in the chassis under loading. Table 9.8 compares the two chassis models and it is clear that the level of deformation in the new lightweight Revision 2 is very similar to the standard chassis and on occasions lower than the standard. The average increase of deformation of the structure over the standard chassis is in the order of 6%, however putting these values into perspective the chassis is enduring approximately 2 mm distortion under maximum loading which on a structure that is in excess of 12 m long and 4 m wide the overall percentage of deformation is very low.

Table 9.8: Deformation comparison between standard and revision 2 chassis

Deflection (mm)		% Rate	Type
Standard Chassis	Revision 2 Chassis		
1.35	1.54	14.07	Increase
1.31	1.58	20.61	Increase
1.97	1.93	2.03	Decrease
1.73	1.82	5.20	Increase
1.92	1.89	1.56	Decrease
1.89	1.91	1.06	Increase

10 Conclusions

The following may be concluded from the outcomes of the research, please note that all tyre tests were conducted using a driven wheel unless otherwise stated:

10.1 Tyre Tests

- Following loading a sandy soil loam of a type used in this experiment it was found that the elastic recovery completed in 1.2 seconds after application.
- The Trelleborg Twin Radial tyre inflated to 1.2 bar generates a lower level of compaction when compared to the Michelin Mega XBib and Trelleborg 425 inflated at 1.6 bar respectively. These inflation pressures the manufacturer minimum operating inflation pressures for the PMC 979 CT Harvester application.
- Operating the PMC CT Harvester on Trelleborg Twin Radial tyres inflated to 1.6 bar in field conditions increases topsoil compaction by 12.6% on soil with a DBD of 1.37 g/cm^3 when compared to the same tyre inflated to 1.6 bar. However the increased compaction is only superficial as it does not extend below the normal plough depth of 250 mm.
- Reducing individual tyre vertical load by 10 kN will reduce soil deformation by 26.8% at a depth of 300 mm through the soil profile.
- This reduction in compaction will be financially beneficial in both cost savings made from post harvest rectification £4 per hectare and increased future yield potential as compaction is less severe at depth.
- Tyre tests undertaken using a towed test rig produce inaccurate results if findings are to be used for a self propelled vehicle. At 300 mm depth in the soil profile a trailed tyre will produce 21.3% less compaction than that of a self propelled tyre.
- For the PMC application replacing the tandem bogie front axle with tracks would not offer a distinct advantage in the reduction of soil compaction. Comparisons undertaken showed that the Claas track generated marginally

lower compaction levels between 100 mm - 290 mm depth; however the draft force requirement for tine rectification was 25% higher due to hardened track pan created by the track.

10.2 FEA Verification

- Through the design and refinement of two testing methods utilising the calibration frame at CU@S it can be concluded that the modelling technique used in Autodesk Inventor 11 and the analysis technique applied in Ansys 10 was within 40% of the measured values with a range of -10% and +30% .
- The over prediction of stress by Ansys 10 occurred at low load levels, this can be attributed to residual stress within the fabricated assemblies unaccounted for by the software.
- A comparison was also undertaken between previous independent test results and the CAD/FEA modelling technique. The findings from this comparison concurred with the calibration results.
- A recommendation for a 10% factor of safety to be added to all results obtained from Ansys10 was made.

10.3 Structural Development

10.3.1 Main Pivot

- The revision 2 of the main pivot offers the best performance for the PMC application. It is 26.8% lighter with an increased life expectancy of 43.5% over the standard main pivot
- Stress distribution in the whole structure has increased through all members of the fabricated assembly; this increase has a positive effect on reducing localised areas of high stress rate.
- Increasing the corner radii of the return manifold in the centre of the axle web improves stress distribution throughout the main body.

- The stub axles and main pivot of the current main pivot are heavily over engineered and are the main cause of the excessive weight in the main pivot.

10.3.2 Rear Axle

- The current rear axle on the PMC 979 CT Harvester is fit for purpose with only minor capacity for improvement in the current design.
- The minor changes would not add any value to the machine performance or reduce machine build costs.

10.3.3 Main Chassis

- Revision 2 of the main chassis out performs the current main chassis. It is 18.4% lighter, has a life expectancy of 42.6% longer than the current and the maximum peak is 10.8% lower than the standard.
- The box section constructed main rails out-perform the I-beam and gusset configuration.
- Re-design of the cross brace network in the dog leg region of the chassis reduces localised stress concentrations forming in main rails at the dog leg joints.
- Triangulation supports added to the main rails for the hopper support frame reduce stress in this area by 6%.

11 Recommendations

The following recommendations can be made from this study for PMC Harvesters revised 979 CT Pea Harvester.

- The best currently available tyre for the PMC 979 CT Harvester is the Trelleborg Twin Radial tyre.
- The Trelleborg Twin Radial Tyre operating at road inflation pressure can be used for all but extremely soft soil conditions ($DBD < 1.3 \text{ g/cm}^3$) provided the farmer is aware that rectification costs will be marginally higher when compared to those incurred using the Trelleborg Twin Radial at manufacturers minimum recommended field pressures.
- The use of Tracks or a Central Tyre Inflation (CTI) system is not beneficial when soil has a $DBD \geq 1.3 \text{ g/cm}^3$.
- When carrying out FEA using Ansys 10 Design space a safety factor of 10% should be added to results to guarantee authenticity.
- Box section should be used for the main chassis rails, with the dogleg having butt welds rather than the current construction of offsetting material, joining and machining flush.
- The cross brace should be manufactured and installed such that no offset is inbuilt at the dogleg, therefore complimenting the butt joints of the main rails.
- The main pivot, stub axles and stub axle housings should all be reduced in size to improve weight-to-strength ratio.
- Triangulation supports should be constructed and installed between the levelling frame, main chassis and dogleg support brace, therefore utilising the full potential of this complex chassis transition.
- Triangulation support should be added to the hopper support frame legs to improve rigidity and reduce premature failure due to fatigue at the joint.
- Revision 2 main pivot and main chassis should be manufactured and fitted to a prototype harvester for assessment and benchmarking.
- The rear axle should remain unchanged for the time being.

12 References

Agricultural Advisory Council (1970) Modern Farming and the soil: report of the agricultural advisory council on soil structure and soil fertility. London: HMSO

Alakukku L & Elonen P (1994) Finnish experiments on subsoil compaction by vehicles with high axle loads. *Soil and Tillage Research* 29, 151-155

Alakukku L (1996) Persistence of soil compaction due to high axle load traffic.1. Short term effects on the properties of clay and organic soils. *Soil and Tillage Research*, 37, 211-222

Alexandrou A & Earl R (1998) The relationship among pre-compaction stress, volumetric water content and initial dry bulk density. *Journal of Agricultural Engineering Research*, 71, 75-80

Ansorge D (2005) Comparison of soil compaction below wheels and tracks. M.Sc by Research thesis, Cranfield University.

Botta G F, Jorajuria D & Draghi L M (2002). Influence of the axle load, tyre size and configuration on the compaction of a freshly tilled clayey soil. *Journal of Terramechanics*, 39, 47-54

Brown H J, Cruse R M, Erbach D C & Melvin S W (1992). Tractive device effects on soil physical properties. *Soil and Tillage Research*, 22, 41-53

Carmen K (1994) Tractor forward velocity and tire load effects on soil compaction. *Journal of Terramechanics*, 31 (1), 11-20

Carmen K (2002) Compaction characteristics of towed wheels on clay loam in a soil bin. *Soil and Tillage Research*, 65 37-43

Danfors B (1994) Changes in subsoil porosity caused by heavy vehicles. *Soil and Tillage Research*, 29, 135-144

Dickson J W (1994) Compaction by a combine harvester operating on moist, loose soil. *Soil and Tillage Research*, 29, 145-150

Dickson J W (1994) Compaction by a combine harvester operating on moist, loose soil. *Soil and Tillage Research*, 29, 145-150

Gameda S, Raghaven G S V, McKeys E, Watsn A K & Mehuys G (1994) Long-term effects of a single incidence of high axle compaction on a clay soil in Quebec. *Soil and Tillage Research*, 29, 173-177

Godwin R J (1975) An extended octagonal ring transducer for use in tillage studies. *Journal of Agricultural Engineering Research*, 20, 347-352

Godwin R J & Ansoorge D (2006) Soil management and profitability, a comparison of the effects of tracks and tyres. Cranfield University

Hakansson I & Reeder R C (1994) Subsoil compaction by vehicles with high axle load - extent, persistence and crop response. *Soil and Tillage Research*, 29, 277-304

Keller T & Arvidsson J (2004) Technical solutions to reduce the risk of subsoil compaction: effects of dual wheels, tandem wheels and tyre inflation pressure on stress propagation in soil. *Soil and Tillage Research*, 79, 191-205

Raper R L, Bailey A C & Burt E C (1994) Prediction of soil stresses caused by tire inflation pressures and dynamic loads. American Society of Agricultural Engineers International Winter Meeting.

Schäfer-Landefeld L, Brandhuber R, Fenner S, Koch H-J & Stockfisch N (2004) Effects of agricultural machinery with high axle load on soil properties of normally managed fields. *Soil and Tillage Research*, 75, 75-86

Slater G, Martin B A & Jarvis D (1988) Stress analysis of chassis detail. Model 979 Pea and Bean Harvester.

Smith D L O & Dickson J W (1990) Contribution of vehicle weight and ground pressure to soil compaction. *Journal of Agricultural Engineering Research*, 46, 13-29

Soane B D, Blackwell P S, Dickson J W, et al (1981) Compaction by agricultural vehicles - A review.1. Soil and Wheel characteristics. *Soil and Tillage* 1(3): 207-237

Soane B D, Boone F R (1986) The effects of tillage and traffic on soil structure. *Soil and Tillage*, 8, 303-306

Taylor J H & Burt E C (1987) Total axle load effects on soil compaction under tractor tires. *American Society of Agricultural Engineers, Paper 86 ((1046):17)*

Van den Akker J J H, Arts W B M, Koolen A J & Stuiver H J (1994) Comparison of stresses, compaction and increase of penetration resistance caused by a low ground pressure tyre and a normal tyre. *Soil and Tillage Research*, 29, 125-134

Wong J Y (1994) On the role of mean maximum pressure as an indicator of cross-country mobility for tracked vehicles. *Journal of Terramechanics*, 31, 197-213

Wong J Y (1991) Some recent developments in vehicle-terrain interaction studies. *Journal of Terramechanics*, 28, 269-288

Wong J Y & Huang Wei, (2004) Wheels vs. Tracks - a fundamental evaluation from the traction perspective. *Journal of Terramechanics*, 43, 27-42

13 Appendix A

13.1 Penetration Graphs

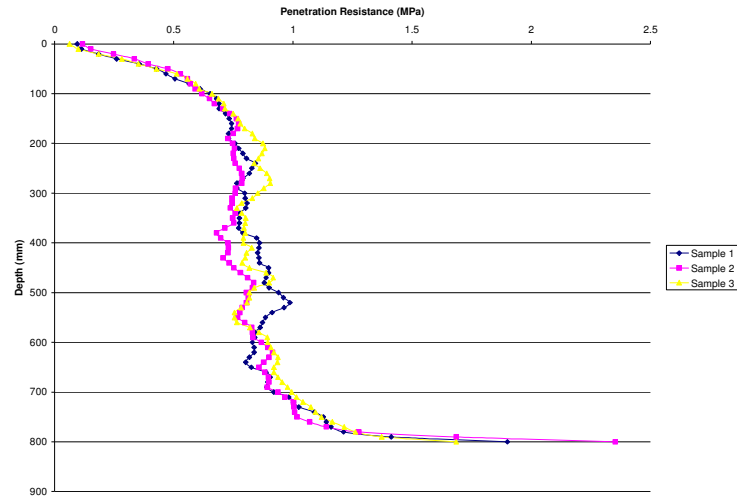


Figure 13.1: Michelin tyre control

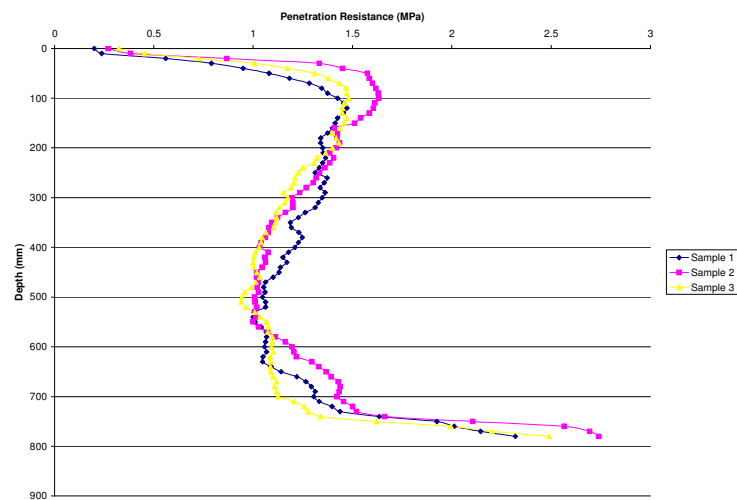


Figure 13.2: Michelin tyre, 1st pass @MMRI, 50 kN load

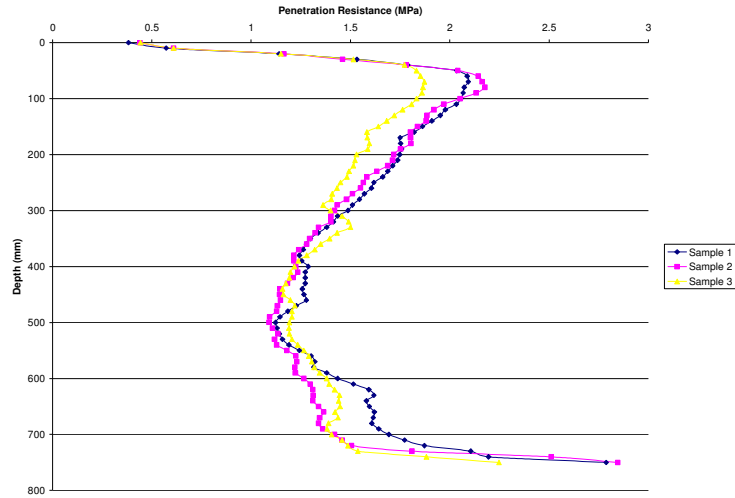


Figure 13.3: Michelin tyre, 2nd pass @MMRI, 50 kN load

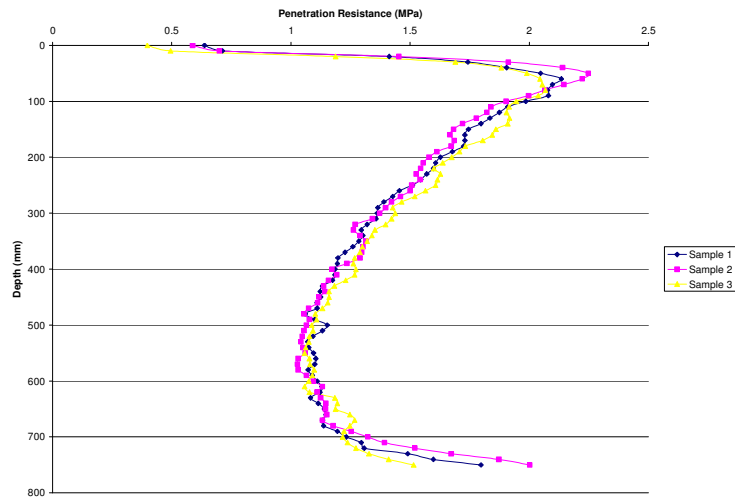


Figure 13.4: Michelin tyre, 3rd pass @MMRI, 50 kN load

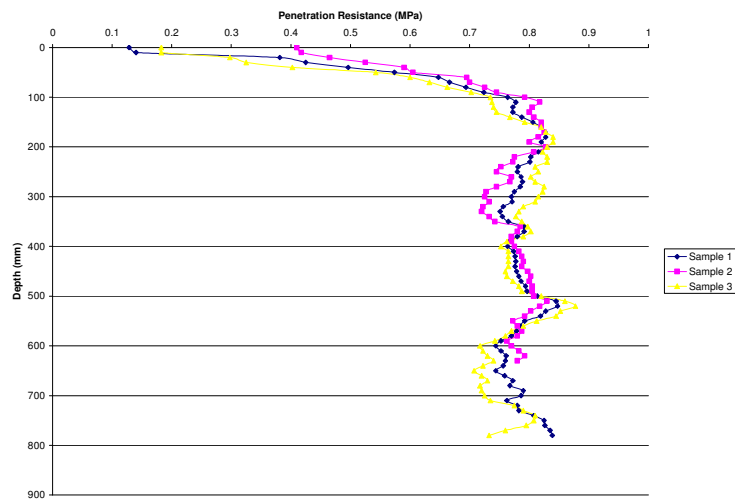


Figure 13.5: Trelleborg 425 tyre control

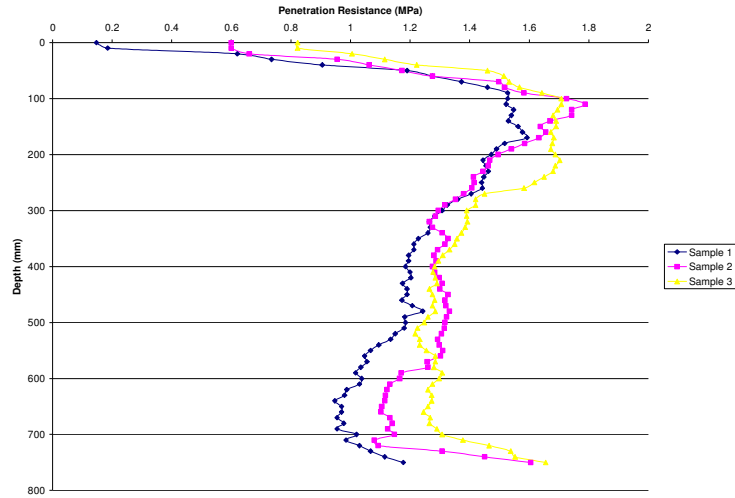


Figure 13.6: Trelleborg 425 tyre, 1st pass @MMRI, 50 kN load

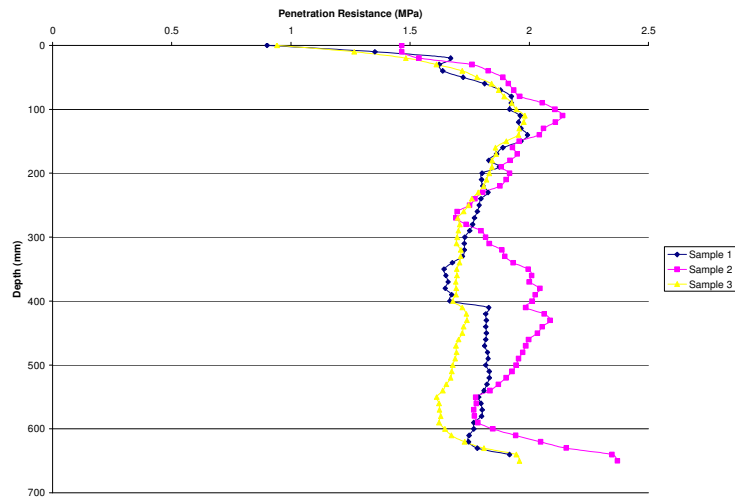


Figure 13.7: Trelleborg 425 tyre, 2nd pass @MMRI, 50 kN load

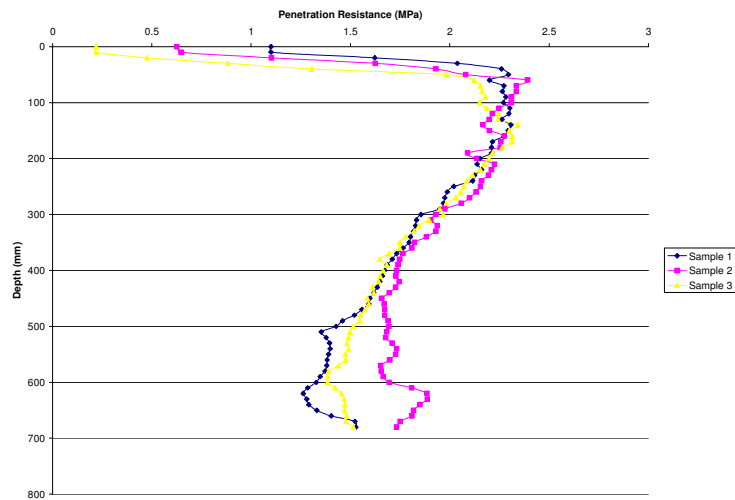


Figure 13.8: Trelleborg 425 tyre, 3rd pass @MMRI, 50 kN load

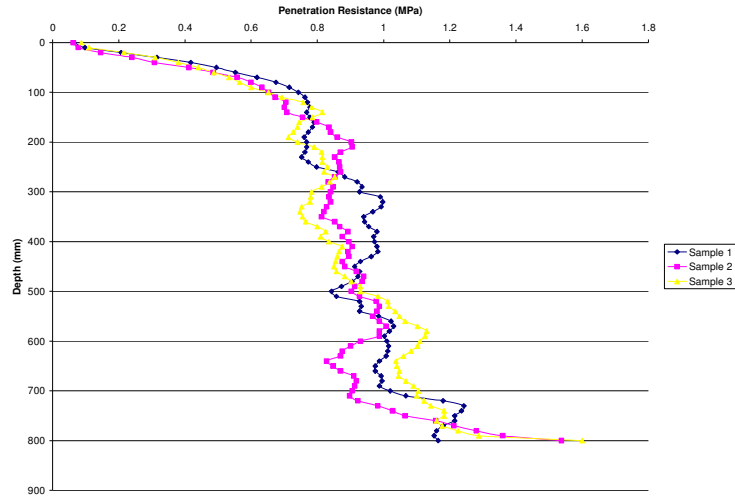


Figure 13.9: Trelleborg Twin Radial Control

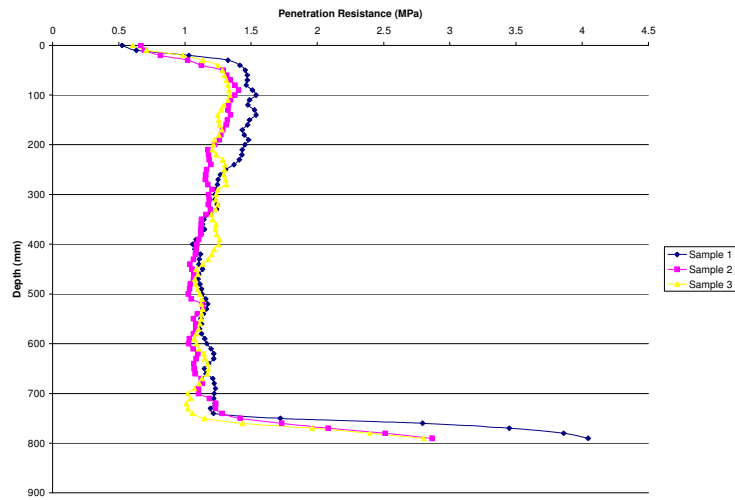


Figure 13.10: Trelleborg Twin Radial, 1st pass @ 1.6 Bar, 45 kN

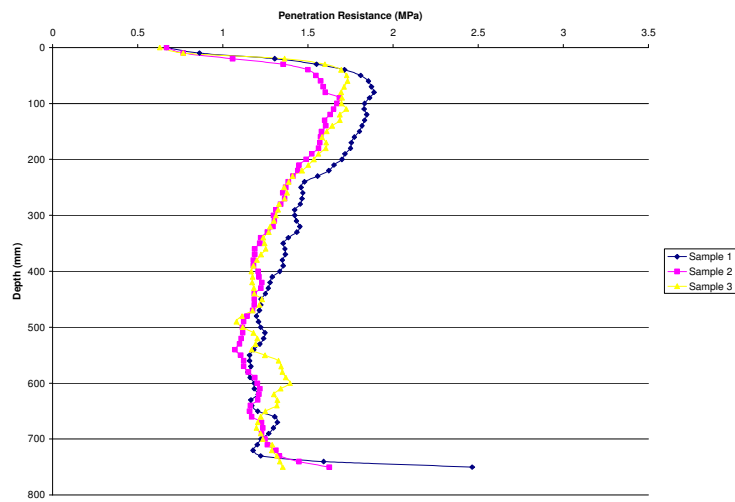


Figure 13.11: Trelleborg Twin Radial, 2nd pass @ 1.6 Bar, 45 kN

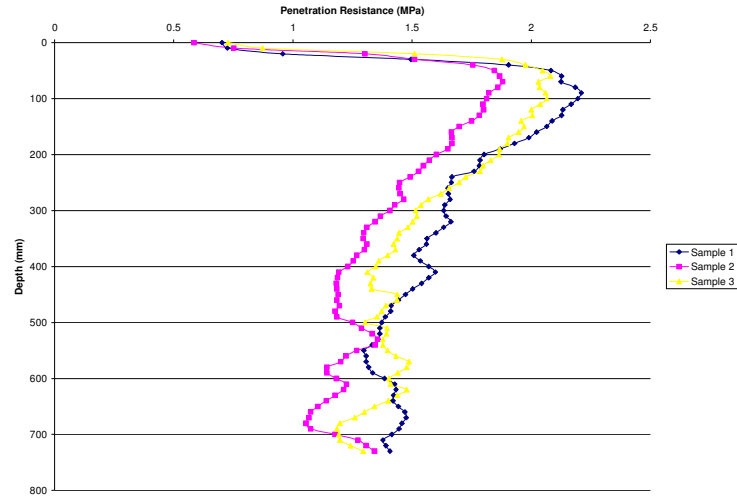


Figure 13.12: Trelleborg Twin Radial, 3rd pass @1.6 Bar, 45 kN

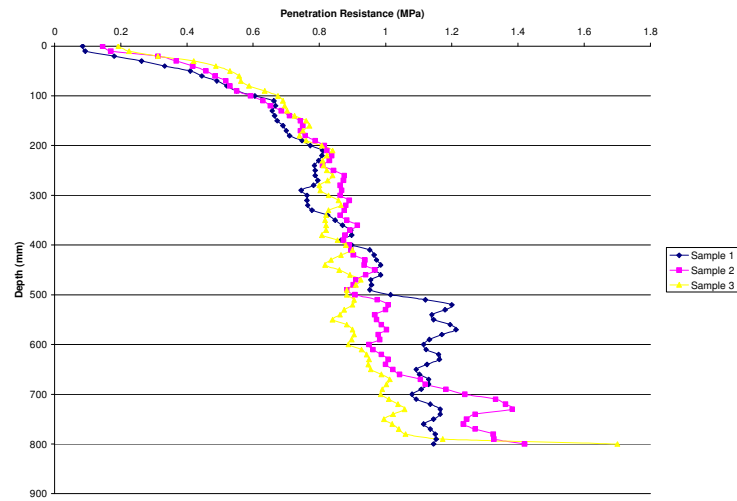


Figure 13.13: Trelleborg Twin Radial, Control, load 40 kN

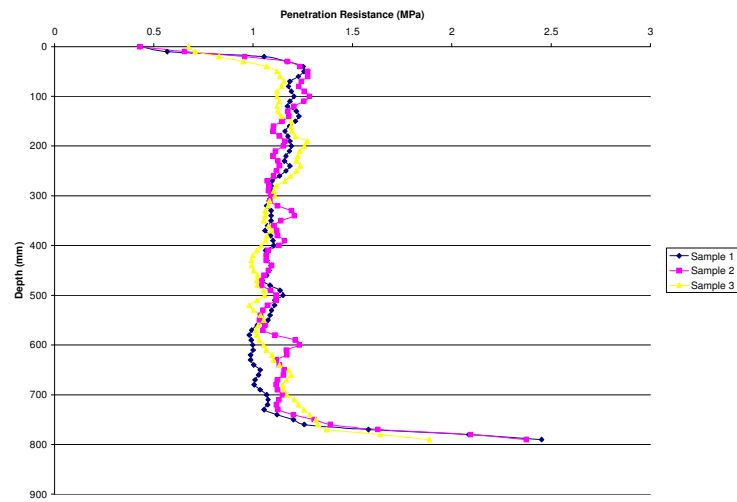


Figure 13.14: Trelleborg Twin Radial, 1st pass @MMRI, load 40 kN

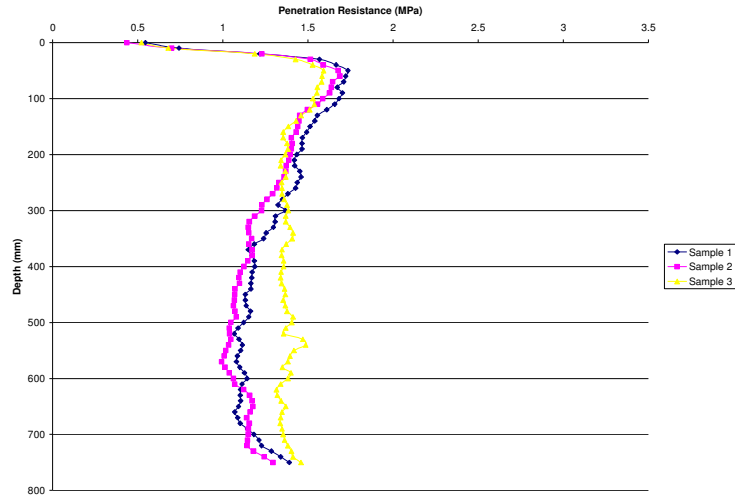


Figure 13.15: Trelleborg Twin Radial, 2nd pass @MMRI, load 40 kN

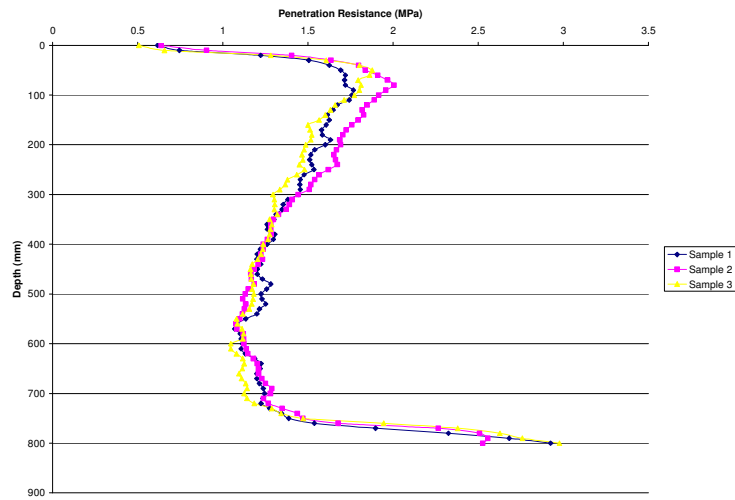


Figure 13.16: Trelleborg Twin Radial, 3rd pass @MMRI, load 40 kN

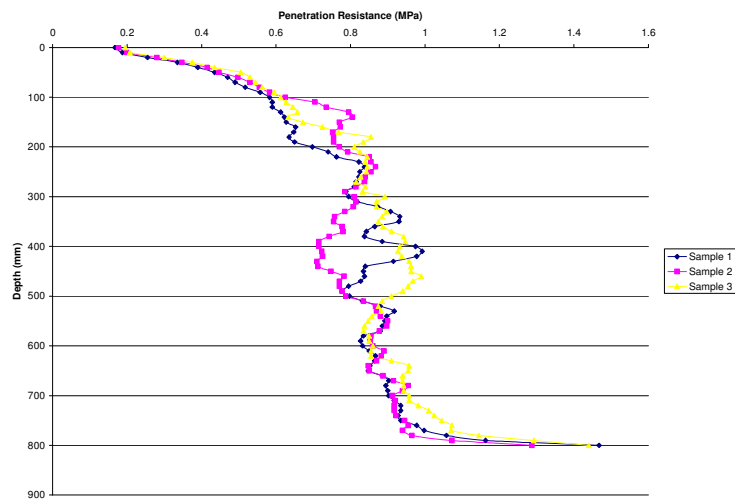


Figure 13.17: Trelleborg Twin Radial, Control, load 45 kN

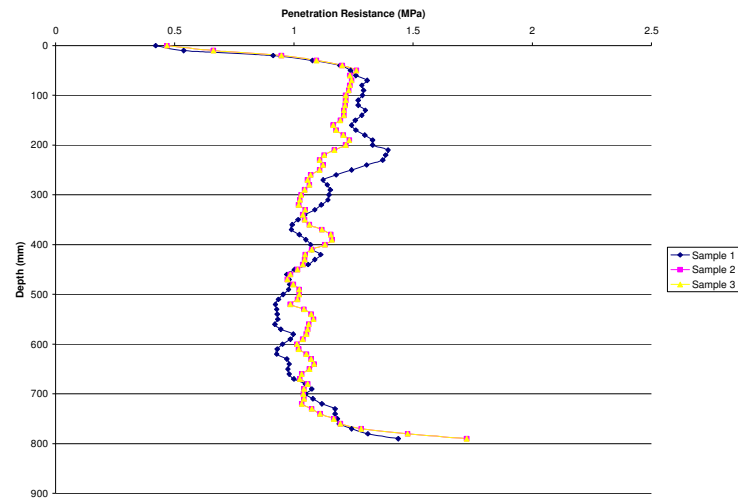


Figure 13.18: Trelleborg Twin Radial, 1st pass @MMRI, load 45 kN

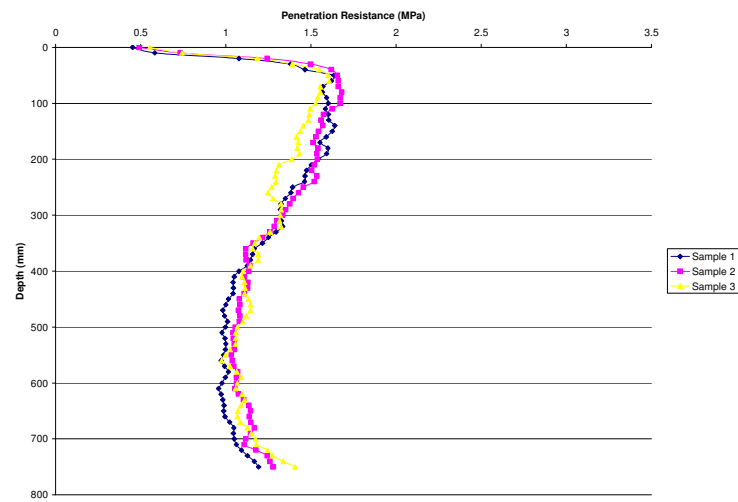


Figure 13.19: Trelleborg Twin Radial, 2nd pass @MMRI, load 45 kN

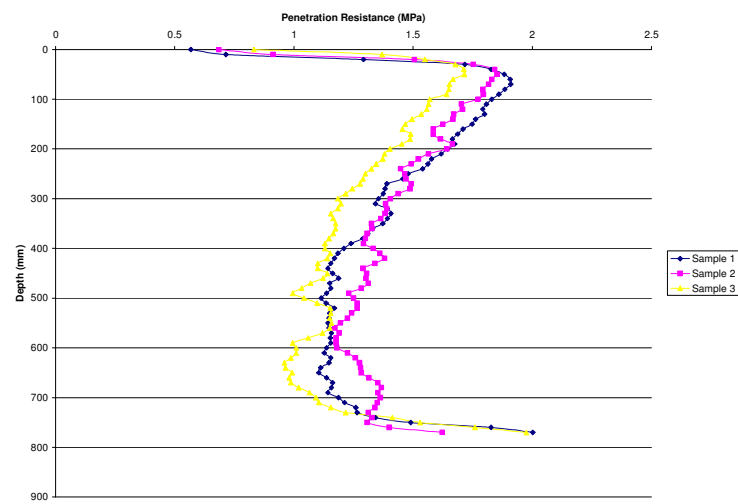


Figure 13.20: Trelleborg Twin Radial, 3rd pass @MMRI, load 45 kN

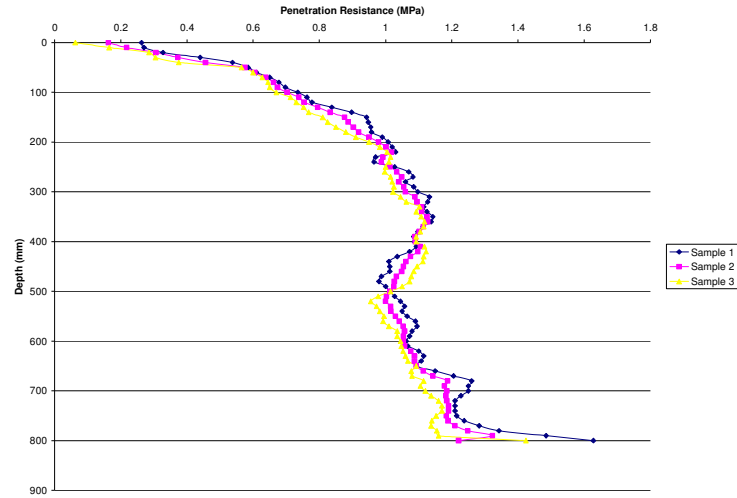


Figure 13.21: Trelleborg Twin Radial, Control, load 50 kN

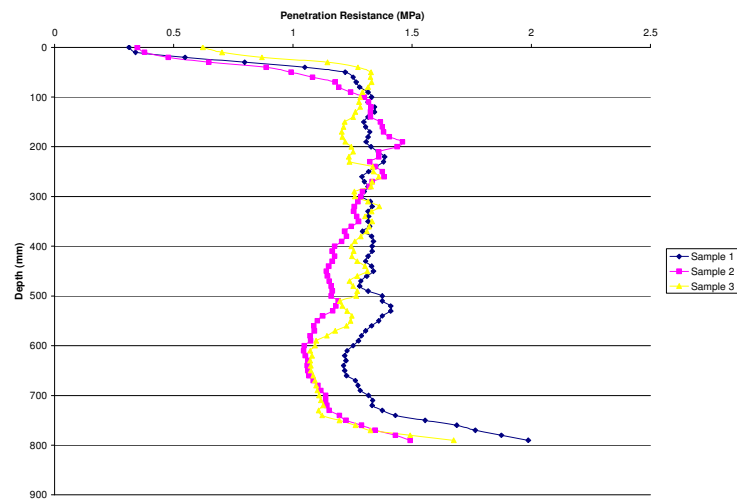


Figure 13.22: Trelleborg Twin Radial, 1st pass @MMRI, load 50 kN

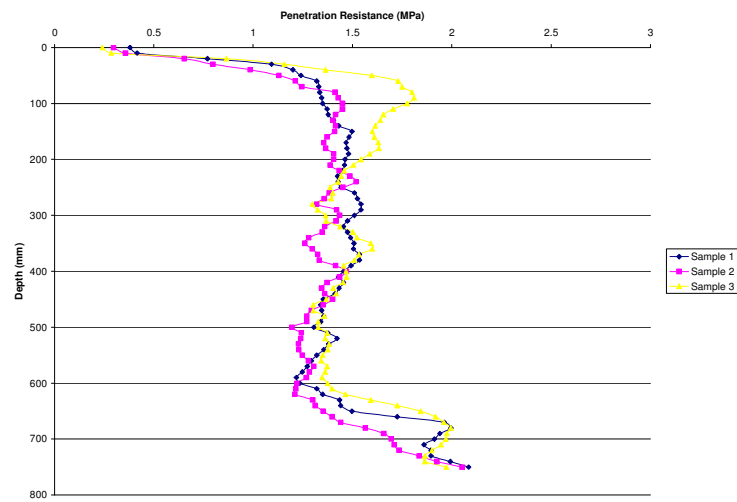


Figure 13.23: Trelleborg Twin Radial, 2nd pass @MMRI, load 50 kN

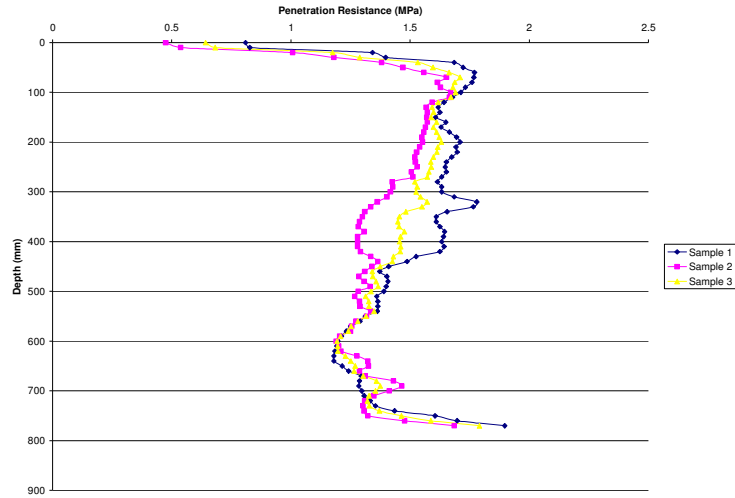


Figure 13.24: Trelleborg Twin Radial, 3rd pass @MMRI, load 50 kN

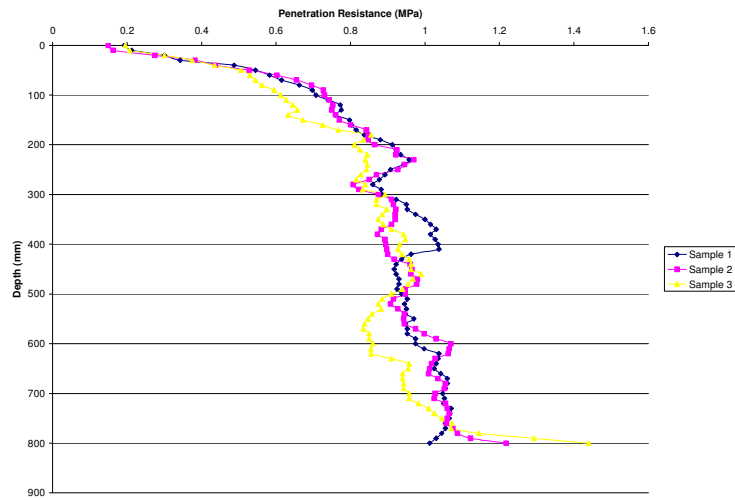


Figure 13.25: Trelleborg Twin Radial, Control, load 45 kN, trailed

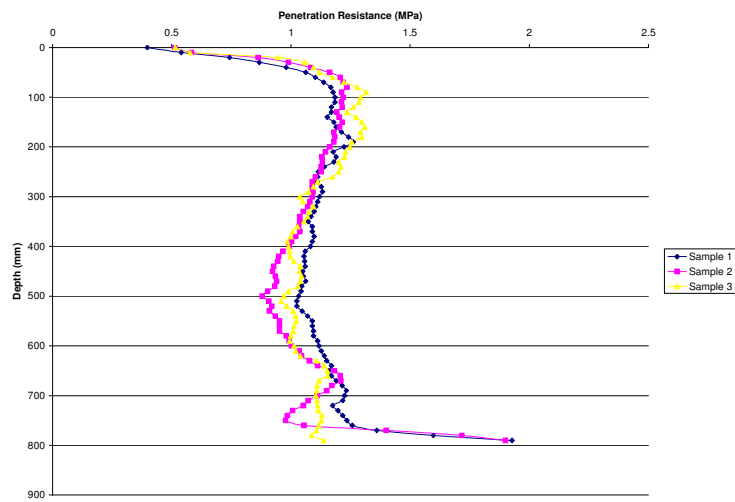


Figure 13.26: Trelleborg Twin Radial, 1st pass @MMRI, load 45 kN, trailed

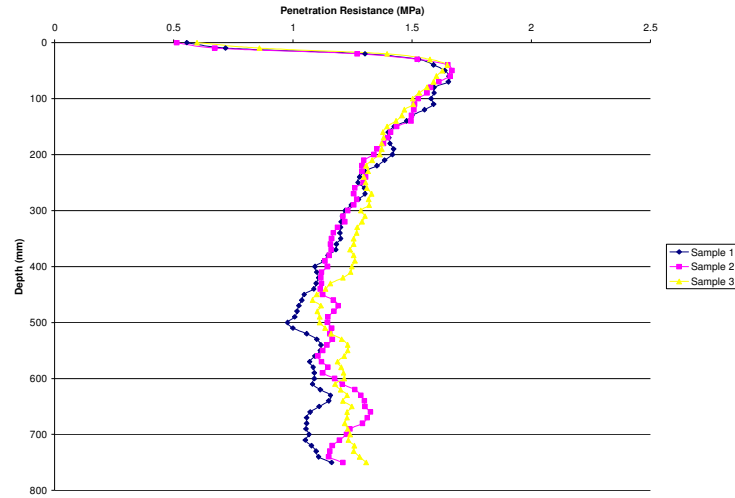


Figure 13.27: Trelleborg Twin Radial, 2nd pass @MMRI, load 45 kN, trailed

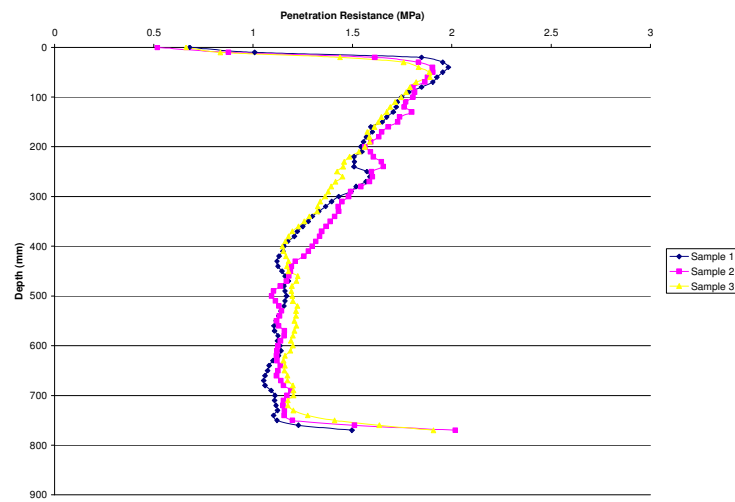


Figure 13.28: Trelleborg Twin Radial, 3rd pass @MMRI, load 45 kN, trailed

13.2 Deformation Graphs

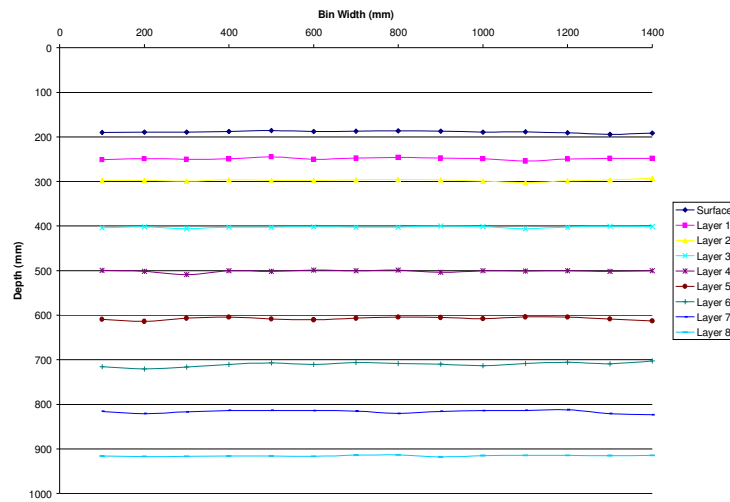


Figure 13.29: Control sample for Michelin wheel at MMRI with 50 kN

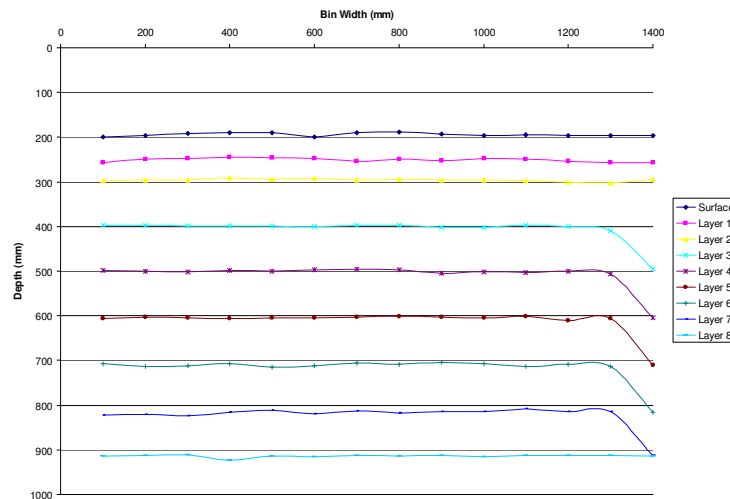


Figure 13.30: Control sample for Michelin wheel at MMRI with 50 kN

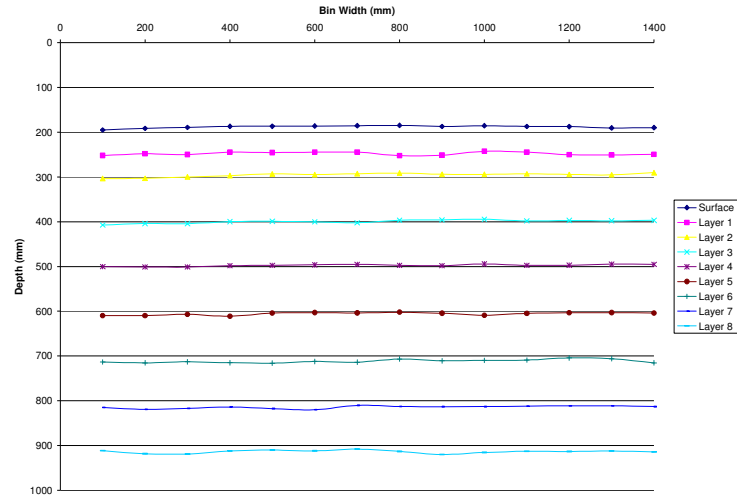


Figure 13.31: Control sample for Michelin wheel at MMRI with 50 kN

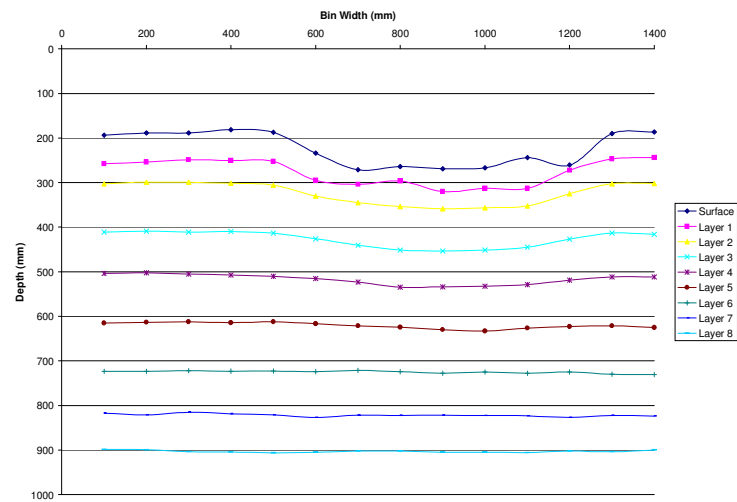


Figure 13.32: 3rd pass sample for Michelin wheel at MMRI with 50 kN test

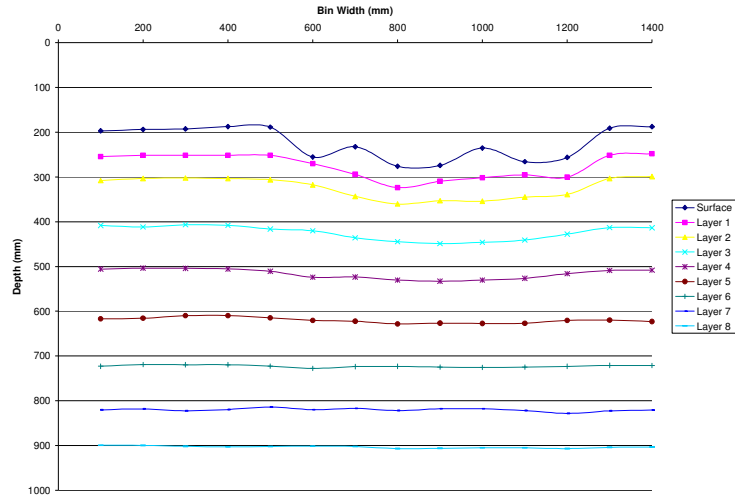


Figure 13.33: 3rd pass sample for Michelin wheel at MMRI with 50 kN test

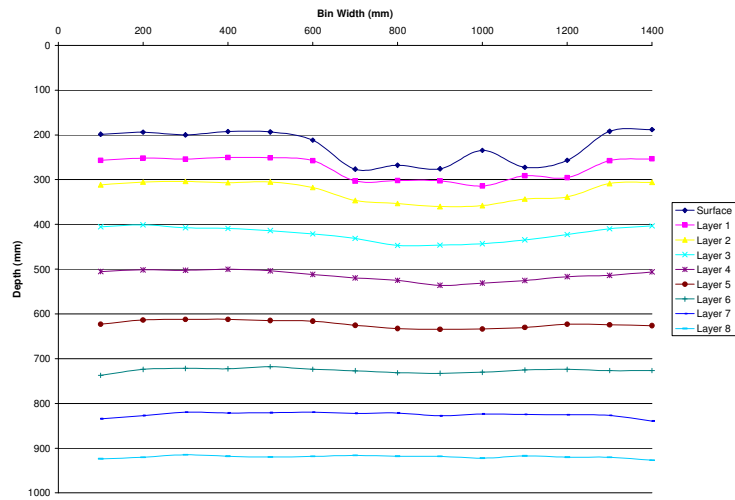


Figure 13.34: 3rd pass sample for Michelin wheel at MMRI with 50 kN test

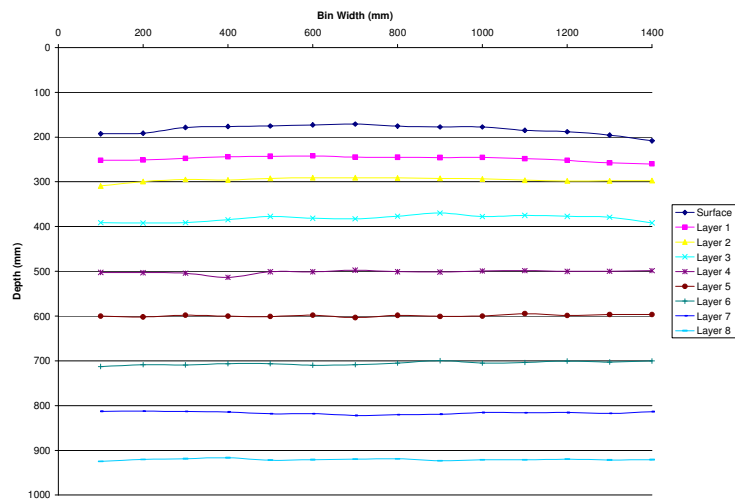


Figure 13.35: Control sample for Trelleborg 425 wheel at MMRI with 50 kN test

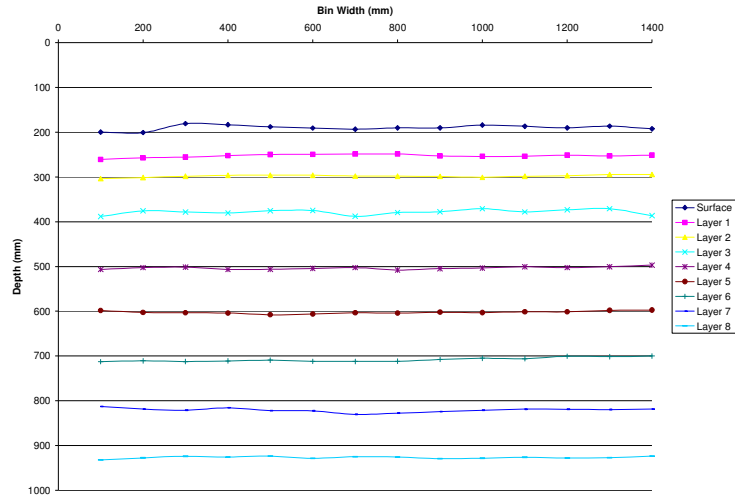


Figure 13.36: Control sample for Trelleborg 425 wheel at MMRI with 50 kN test

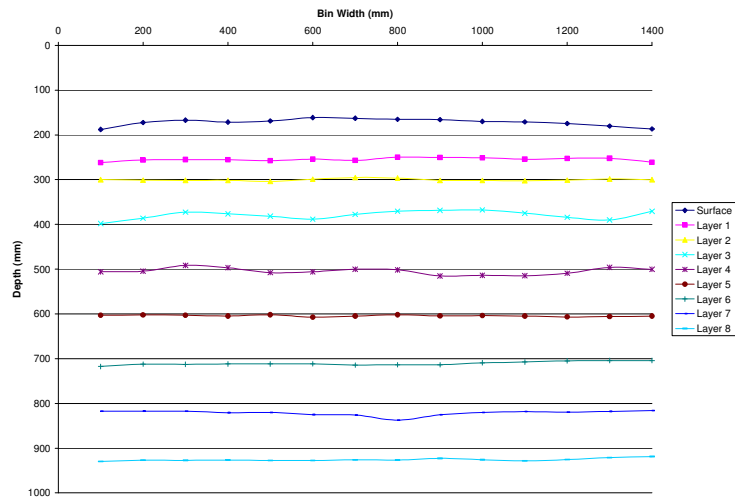


Figure 13.37: Control sample for Trelleborg 425 wheel at MMRI with 50 kN test

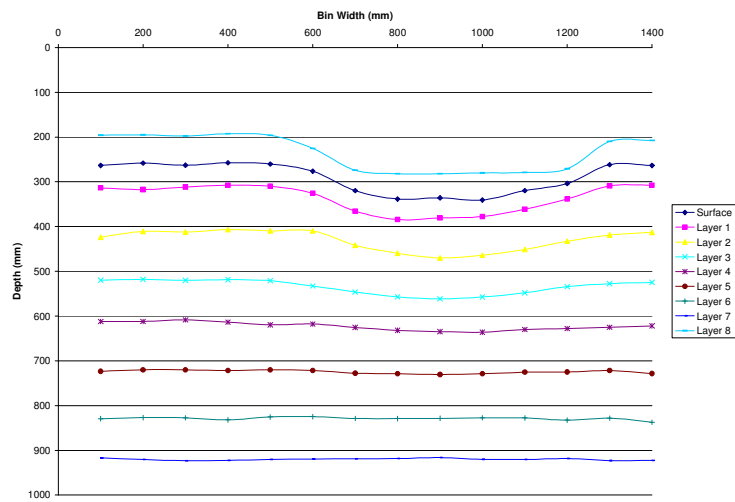


Figure 13.38: 3rd pass sample for Trelleborg 425 wheel at MMRI with 50 kN test

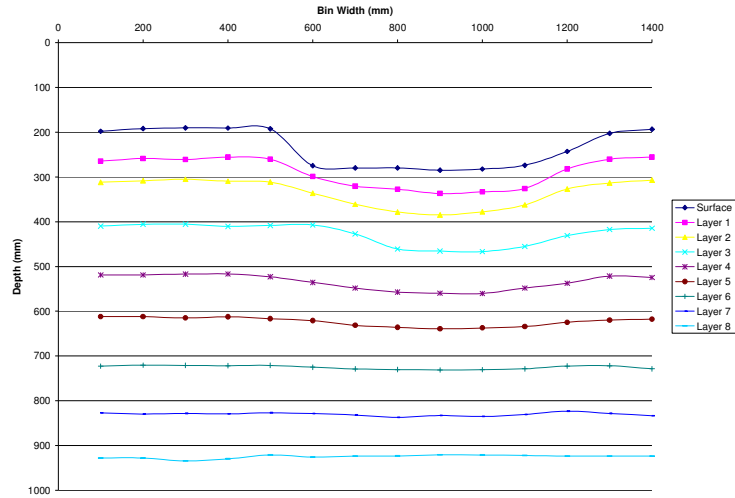


Figure 13.39: 3rd pass sample for Trelleborg 425 wheel at MMRI with 50 kN test

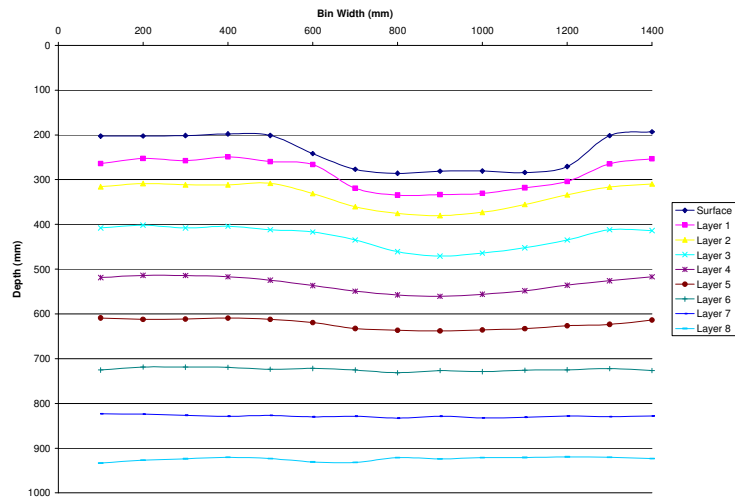


Figure 13.40: 3rd pass sample for Trelleborg 425 wheel at MMRI with 50 kN test

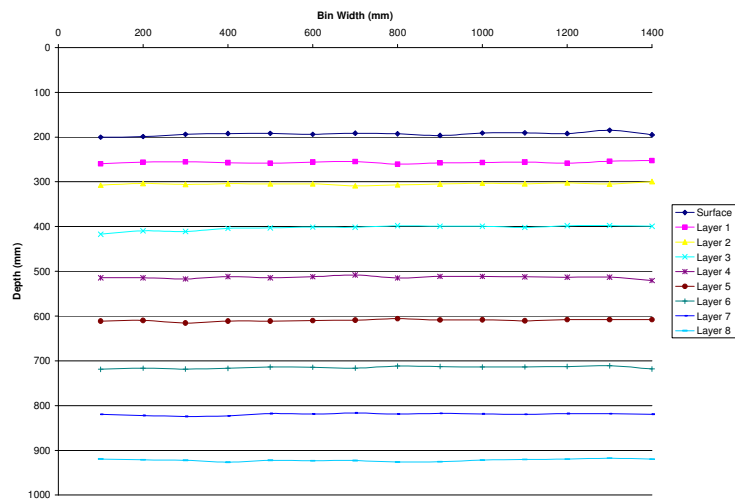


Figure 13.41: Control sample for Trelleborg Twin Radial wheel at MMRI with 40 kN test

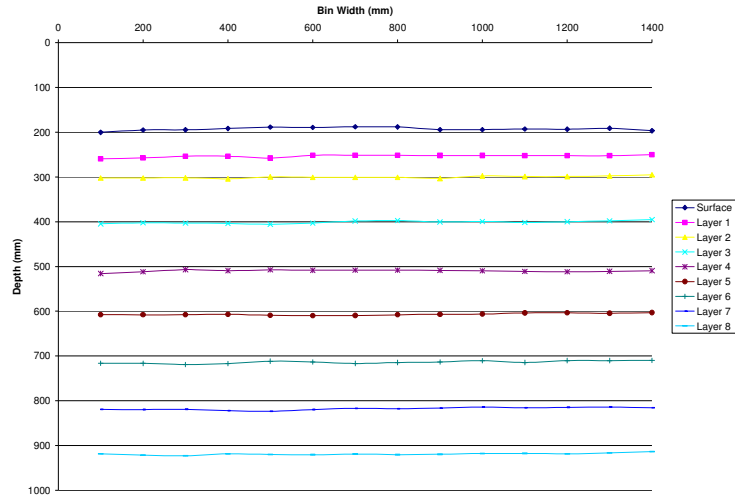


Figure 13.42: Control sample for Trelleborg Twin Radial wheel at MMRI with 40 kN test

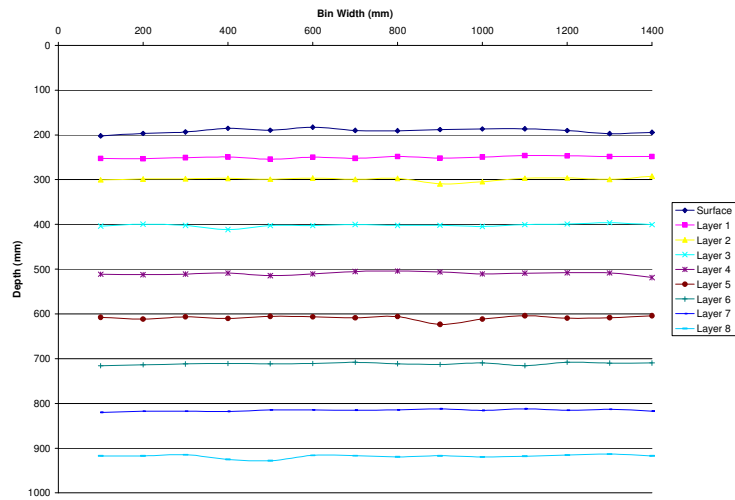


Figure 13.43: Control sample for Trelleborg Twin Radial at MMRI with 40 kN test

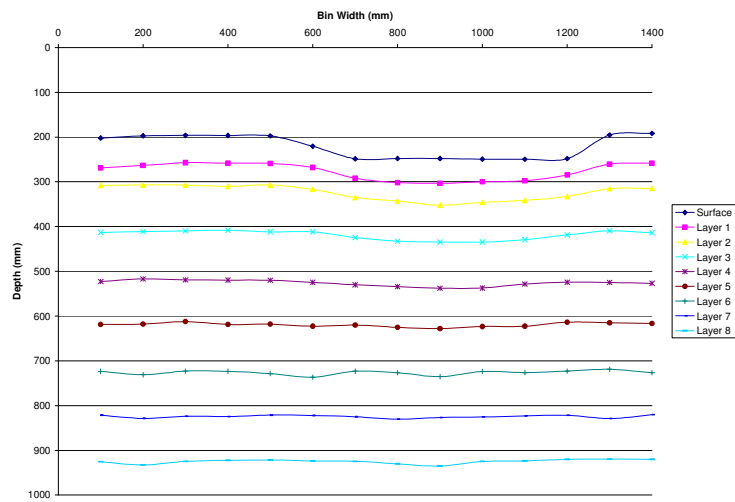


Figure 13.44: 3rd pass sample for Trelleborg Twin Radial wheel at MMRI with 40 kN test

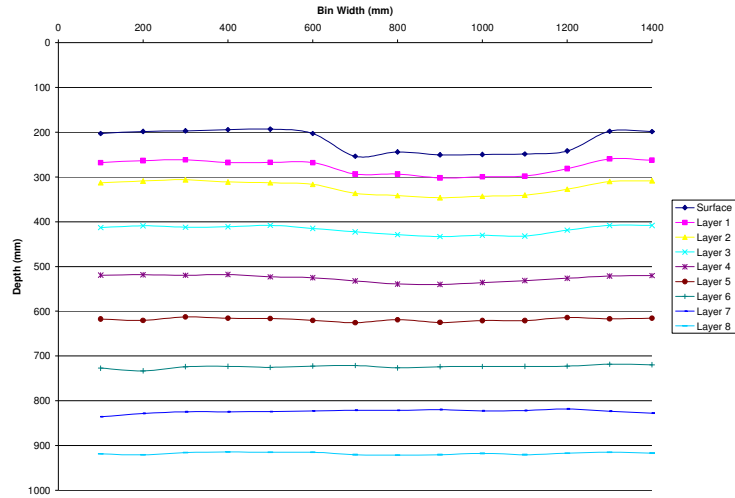


Figure 13.45: 3rd pass sample for Trelleborg Twin Radial wheel at MMRI with 40 kN test

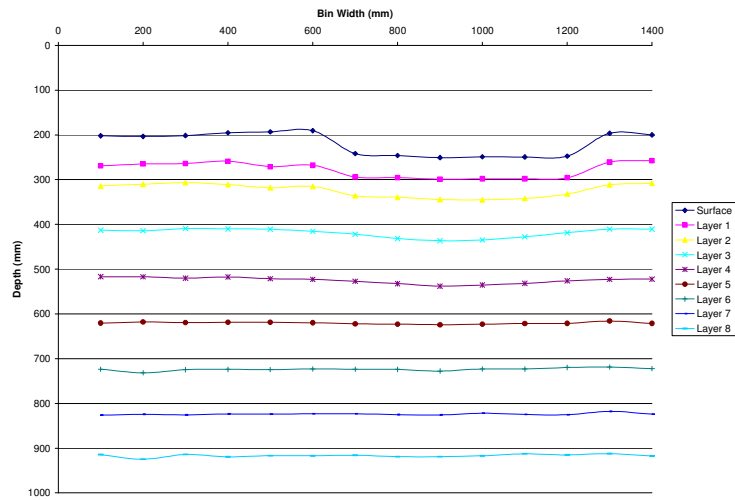


Figure 13.46: 3rd pass sample for Trelleborg Twin Radial wheel at MMRI with 40 kN test

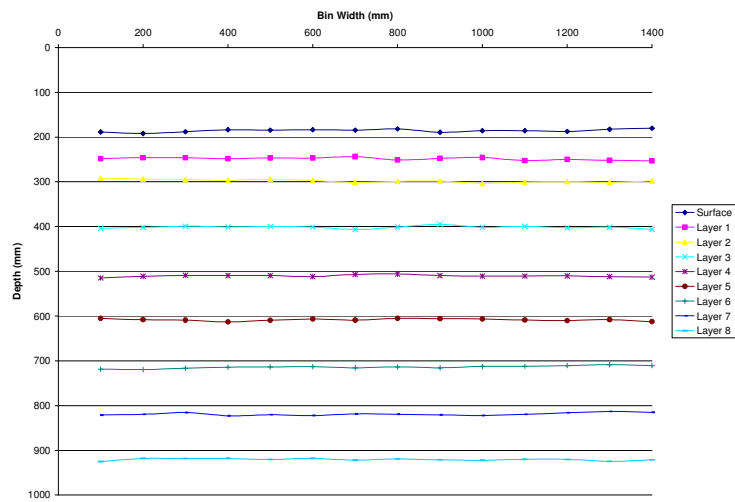


Figure 13.47: Control sample for Trelleborg Twin Radial wheel at MMRI with 45 kN test

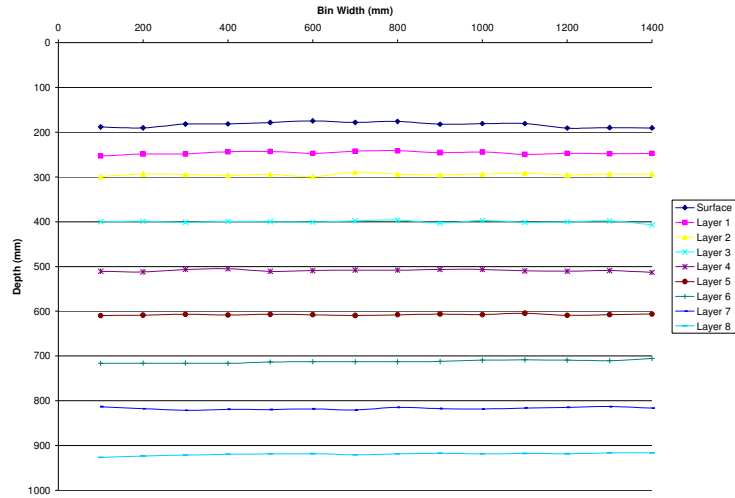


Figure 13.48: Control sample for Trelleborg Twin Radial wheel at MMRI with 45 kN test

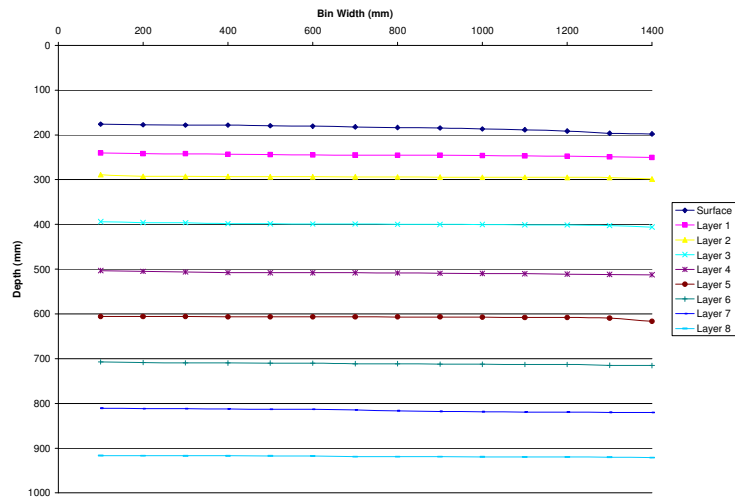


Figure 13.49: Control sample for Trelleborg Twin Radial wheel at MMRI with 45 kN test

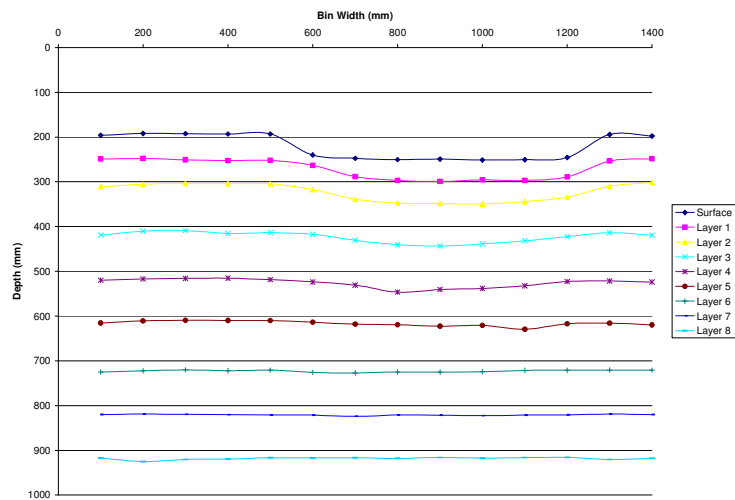


Figure 13.50: 3rd pass sample for Trelleborg Twin Radial wheel at MMRI with 45 kN test

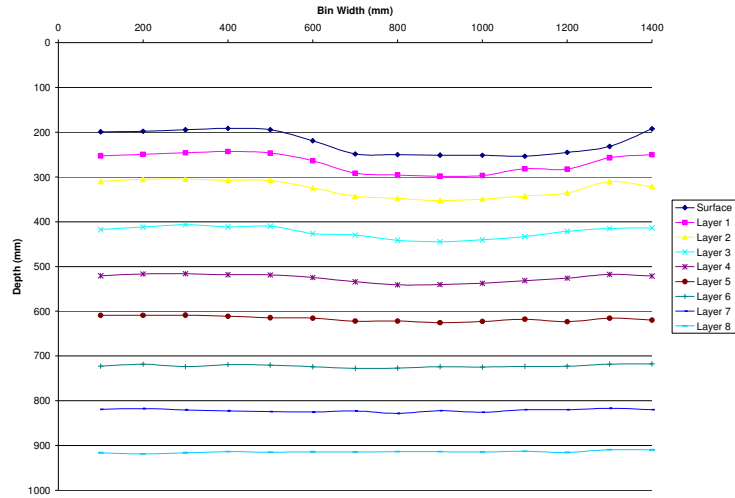


Figure 13.51: 3rd pass sample for Trelleborg Twin Radial wheel at MMRI with 45 kN test

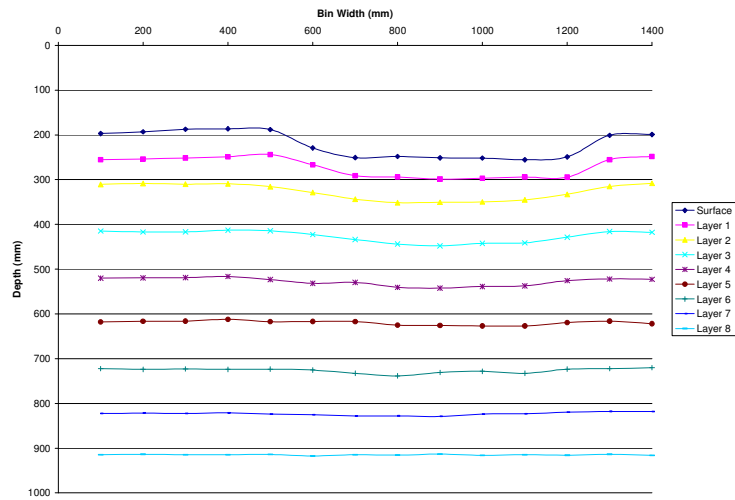


Figure 13.52: 3rd pass sample for Trelleborg Twin Radial wheel at MMRI with 45 kN test

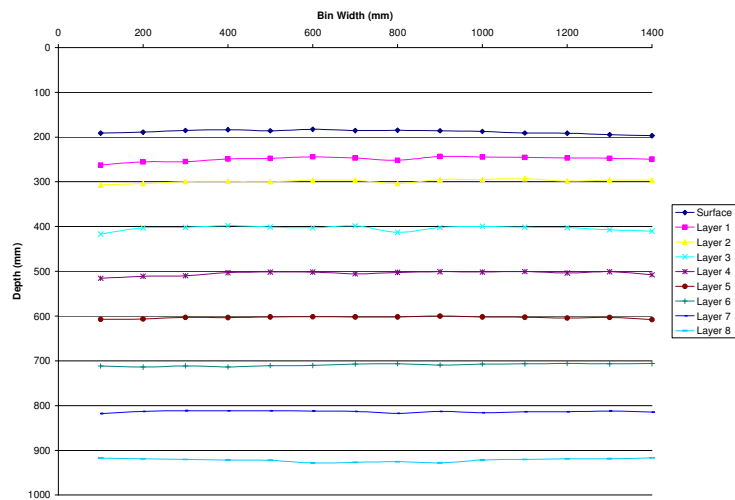


Figure 13.53: Control sample for Trelleborg Twin Radial wheel at MMRI with 50 kN test

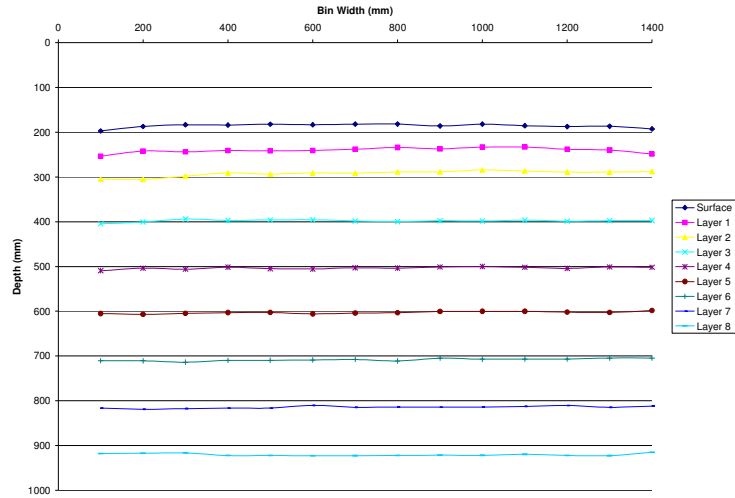


Figure 13.54: Control sample for Trelleborg Twin Radial wheel at MMRI with 50 kN test

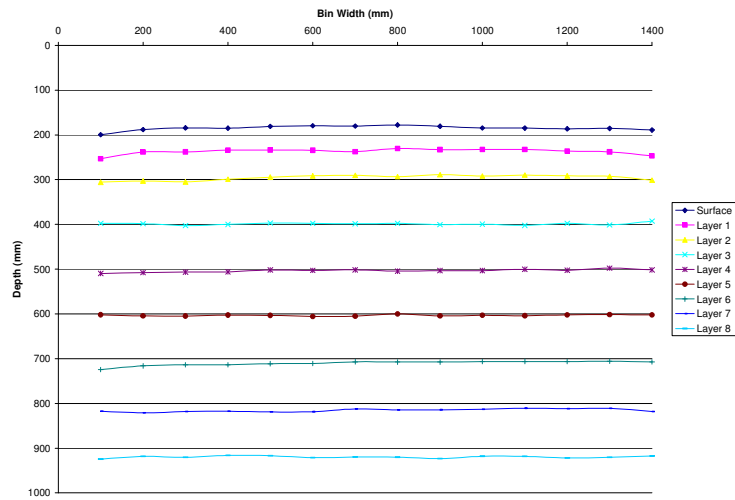


Figure 13.55: Control sample for Trelleborg Twin Radial wheel at MMRI with 50 kN test

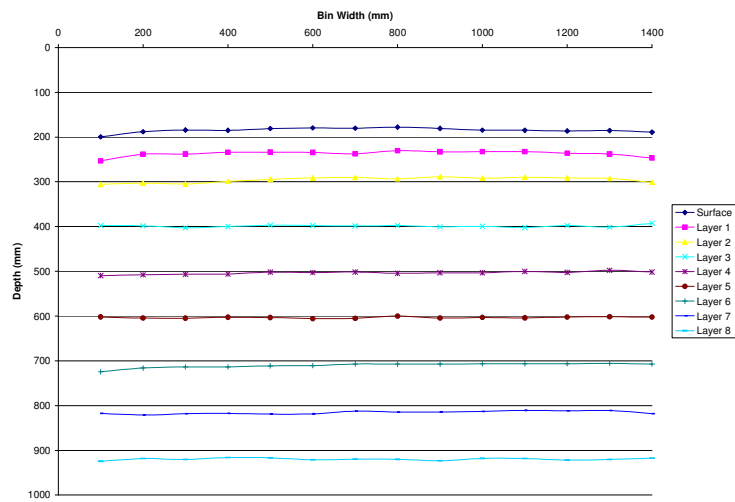


Figure 13.56: 3rd pass sample for Trelleborg Twin Radial wheel at MMRI with 50 kN test

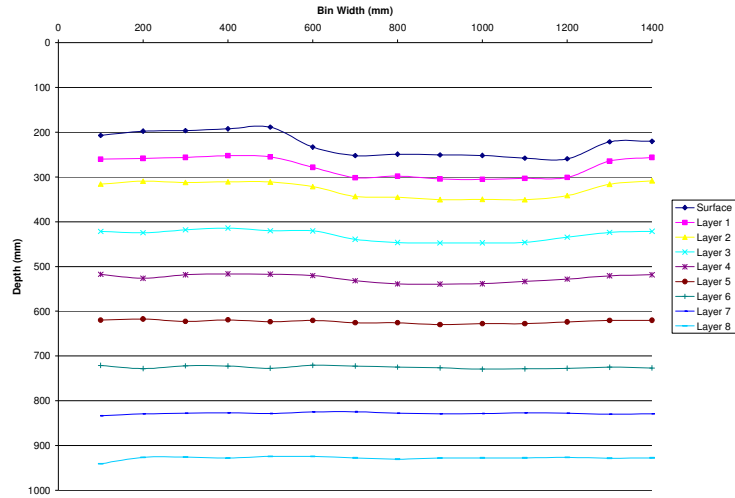


Figure 13.57: 3rd pass sample for Trelleborg Twin Radial wheel at MMRI with 50 kN test

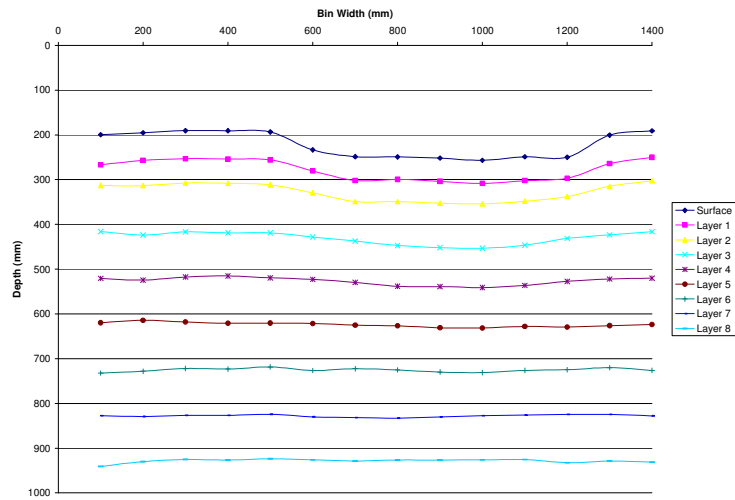


Figure 13.58: 3rd pass sample for Trelleborg Twin Radial wheel at MMRI with 50 kN test

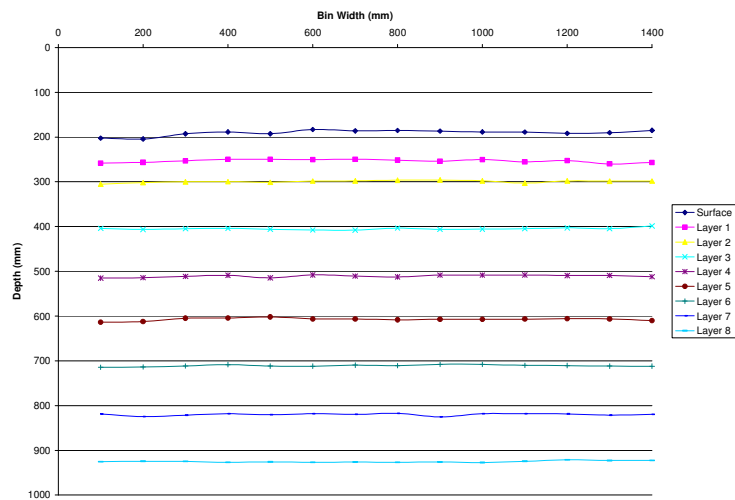


Figure 13.59: Control sample for Trelleborg Twin Radial wheel at MMRI with 45 kN test, trailed

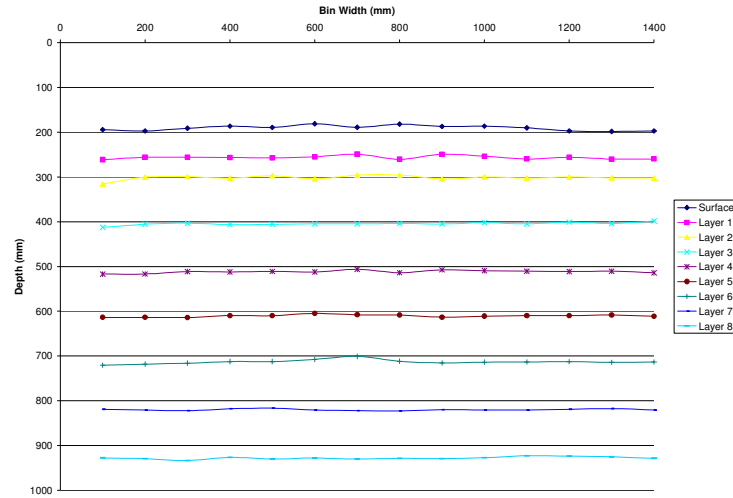


Figure 13.60: Control sample for Trelleborg Twin Radial wheel at MMRI with 45 kN test, trailed

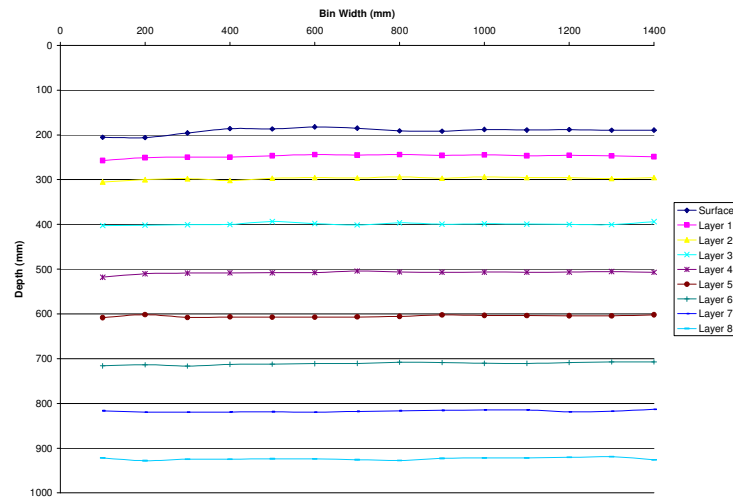


Figure 13.61: Control sample for Trelleborg Twin Radial wheel at MMRI with 45 kN test, trailed

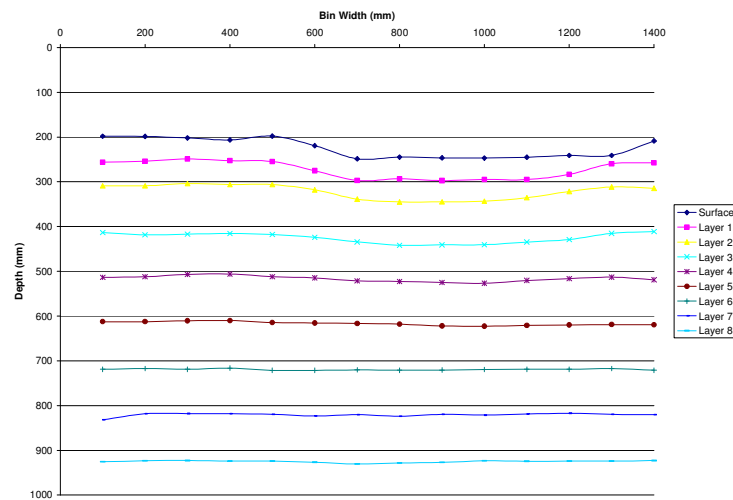


Figure 13.62: 3rd pass sample for Trelleborg Twin Radial wheel at MMRI with 45kN test, trailed

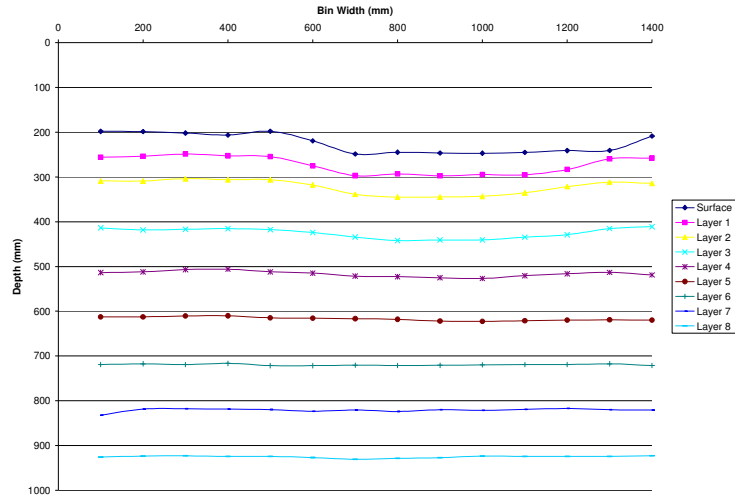


Figure 13.63: 3rd pass sample for Trelleborg Twin Radial wheel at MMRI with 45kN test, trailed

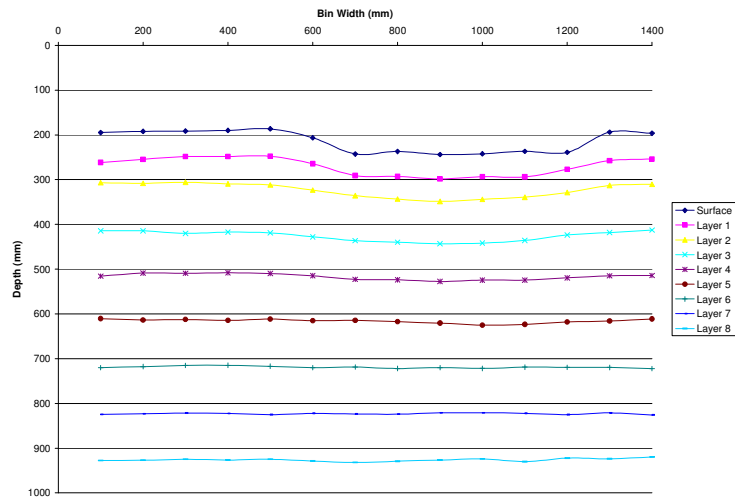


Figure 13.64: 3rd pass sample for Trelleborg Twin Radial wheel at MMRI with 45kN test, trailed

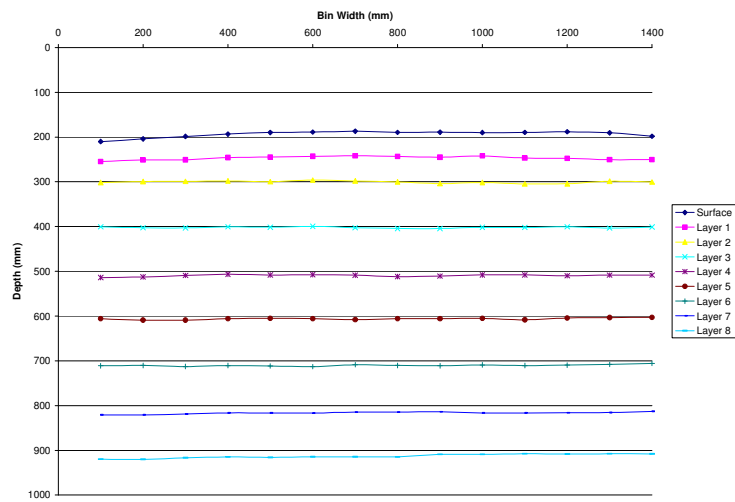


Figure 13.65: Control sample for Trelleborg Twin Radial wheel at 1.6 bar with 50 kN test

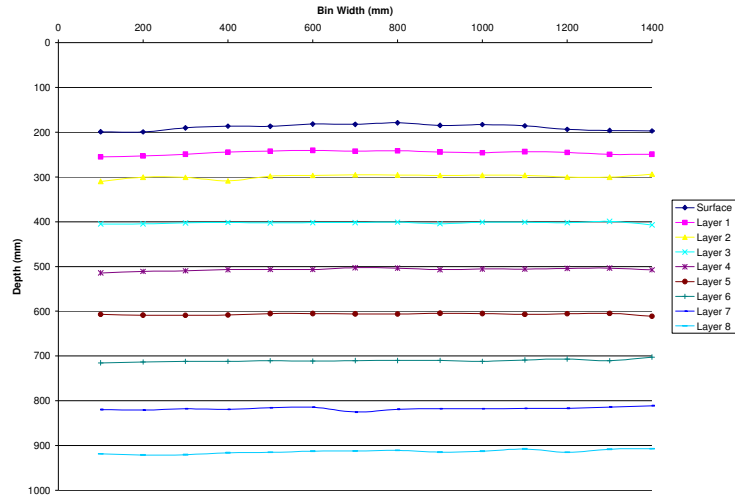


Figure 13.66: Control sample for Trelleborg Twin Radial wheel at 1.6 bar with 50 kN test

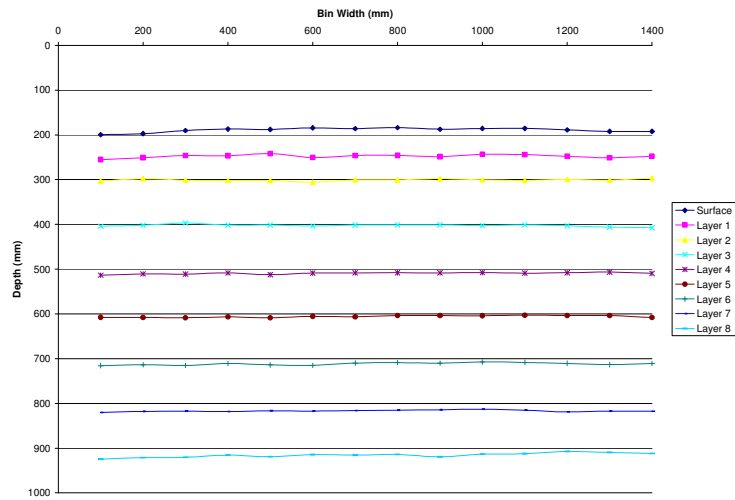


Figure 13.67: Control sample for Trelleborg Twin Radial wheel at 1.6 bar with 50 kN test

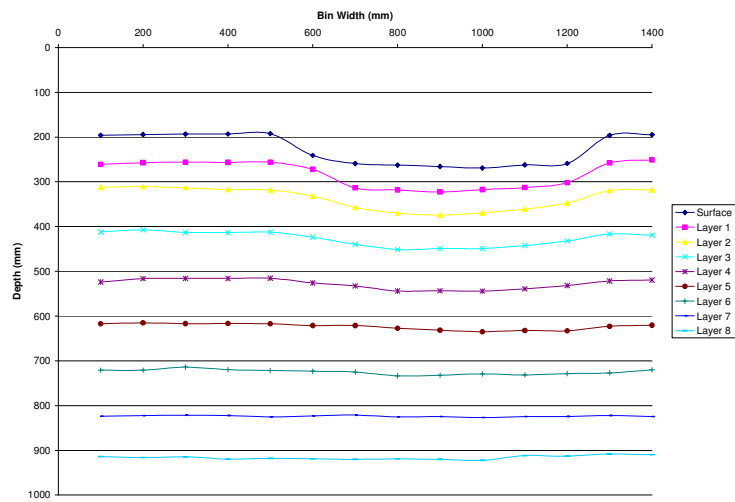


Figure 13.68: 3rd pass sample for Trelleborg Twin Radial wheel at 1.6 bar with 50 kN test

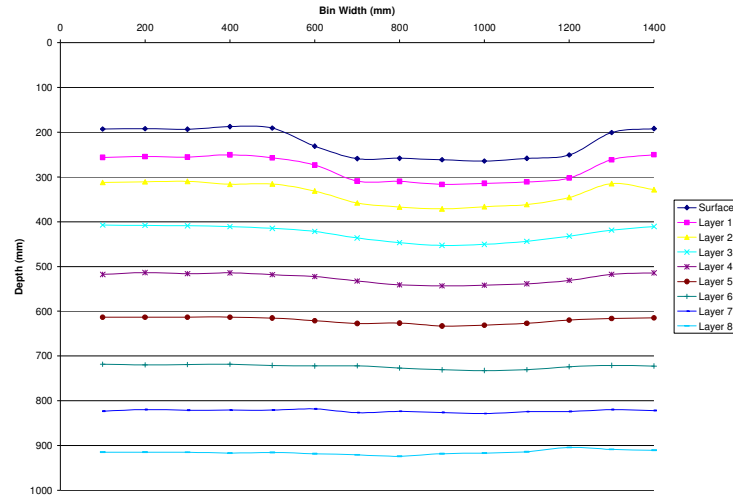


Figure 13.69: 3rd pass sample for Trelleborg Twin Radial wheel at 1.6 bar with 50 kN test

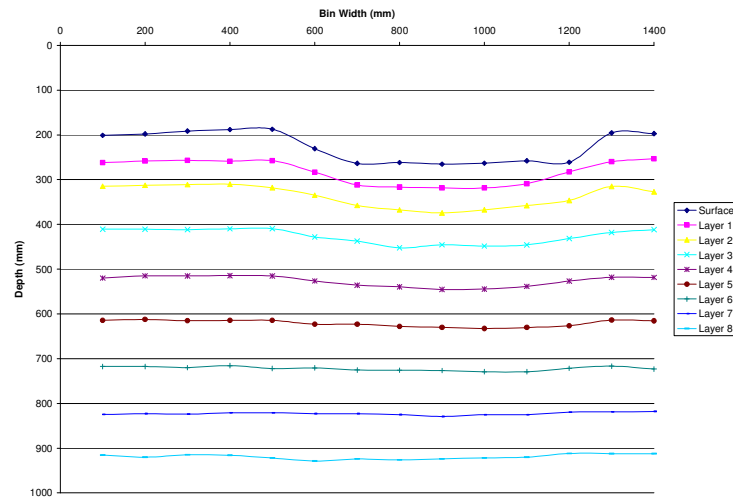


Figure 13.70: 3rd pass sample for Trelleborg Twin Radial wheel at 1.6 bar with 50 kN test

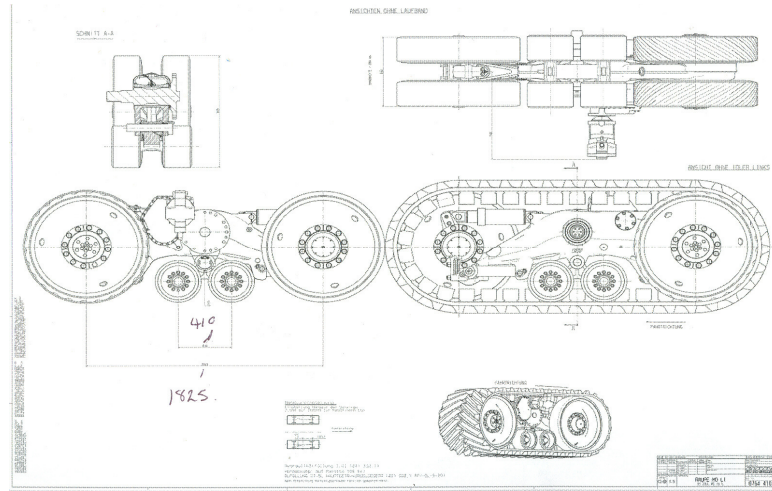


Figure 13.71: Claas tracks

14 Appendix B

14.1 FEA Verification

Silsoe Campus Design Office
NSRI Engineering Group

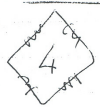
Cranfield
UNIVERSITY
Silsoe

CALCULATION SHEET

Project Title: Tractor Transducer supply - Compostala		Calc. No:	
Subject: PDS and Stress Calculation		Sheet No:	
Budget/Job: DO 731 - WR0195S		Dwg:	
Designer: Dr James L. Brighton	Date:	Revised:	Date:
Checker:	Date:	Checked:	Date:


BRIDGES

ACTIVE GAUGES




B.F. = 1

$$V_{out} = \frac{E \cdot V_s \cdot K}{1} = \frac{\Delta V}{V} = \epsilon \cdot K$$



B.F. = 1/2

$$V_{out} = \frac{E \cdot V_s \cdot K}{2}$$



B.F. = 1/4

$$V_{out} = \frac{E \cdot V_s \cdot K}{4}$$

$$\frac{\Delta V}{V} = K \cdot \epsilon \cdot B.F.$$

$$\epsilon = \frac{\Delta V}{V} / K \cdot B.F.$$

$$E = \frac{\sigma}{\epsilon}$$

$$\frac{M_y}{I} = \sigma = \epsilon \cdot r$$

SV = Gauge

Typical K_0 Gauge factor = 2.060 $\frac{\Delta V}{V} = K \cdot \epsilon \cdot B.F.$

Form: Calsh2.doc
Issue 06/03
JLB

VISHAY VISHAY MICRO-MEASUREMENTS & SR-4
General Purpose
STRAIN GAGES

FOR COMPLETE TECHNICAL DATA, VISIT WWW.VISHAY.COM/REF/STRAIN/GAGES


GRID	GRID RESISTANCE IN OHMS	TC OF GAGE FACTOR, %/100°C
	120.0±0.4%	(+1.2±0.2)
GRID	GAGE FACTOR @ 24°C	TRANSVERSE SENSITIVITY
1		
2		
3		
NOM	2.07 NOM	(+1.3 ±0.2)%

ORDER	THERMAL OUTPUT COEFFICIENTS FOR 1018 STEEL	
	FAHRENHEIT	CELSIUS
0	-2.02E+2	-7.50E+1
1	+5.10E+0	+5.28E+0
2	-3.83E-2	-9.64E-2
3	+9.28E-5	+4.94E-4
4	-6.35E-8	-6.67E-7

FOIL LOT NUMBER	BATCH NUMBER
A66AD889	VF383464

ITEM CODE	QUANTITY	CODE
6829	10	162714

MADE IN UNITED STATES



EA-06-060RZ-120/E

15 Appendix C

15.1 Support System Development

15.1.1 Picking Head Lugs

(979-103-143.
Picking head.

2 scenarios to be considered.

Situation ①.

Header being carried by high Rams, i.e. at headload.

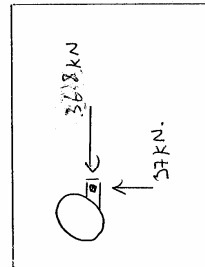
Situation ②.

Header in transport position, i.e. carried on chains.

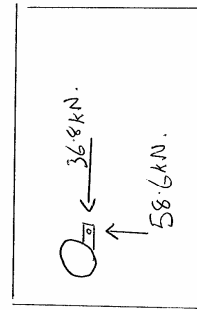
Both situation has a horizontal load set out 3g.

∴ $M \times 3g \Rightarrow 368 \text{ kN}$.

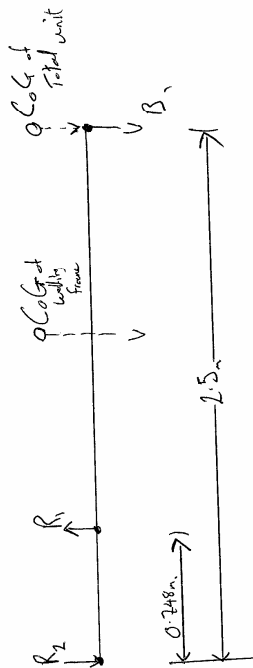
Situation 1.



Situation 2.



Situation 1.



$$\sum M_A \Rightarrow 2.5 \times 2.5 - R_1 (0.748) = 0$$

$$R_1 = \frac{62.5}{0.748}$$

$$= 83.6 \text{ kN.}$$

$$= 41.8 \text{ kN.}$$

R_1 max hyd pressure $\Rightarrow 53 \text{ kN}$
Reaction @ A

$$\sum M_B \Rightarrow (R_2 \times 2.5) - 41.8 (1.752) = 0 \quad \text{Mass Case}$$

$$\Rightarrow R_2 = 29.3 \text{ kN.} \Rightarrow \text{IF constrained by hyd cylinder travel.}$$

Hyd Case

$$\sum M_B \Rightarrow R_2 (2.5) - 53 (1.752) = 0$$

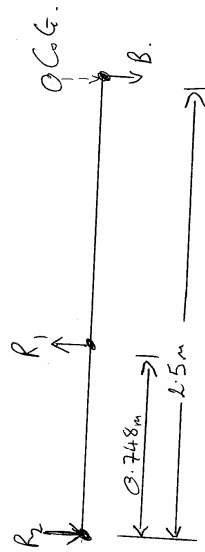
$$R_2 = 37 \text{ kN Vert.}$$

Max Cond if lift is not constrained by hyd cylinder travel.

$$\therefore \text{Max } R_2 = 37 \text{ kN } \uparrow$$

Situation 2.

$$B = 25 \text{ kN.}$$



$$\sum M_{R_1} \Rightarrow B(1.752) - R_2(0.748) = 0.$$

$$R_2 = \frac{25(1.752)}{0.748}$$

$$= 58.56 \text{ kN.}$$

$$\therefore \text{Max } R_2 = 58.56 \text{ kN } \uparrow$$

15.1.2 Tractive Forces

$$() 979 - 103 - 143 - ()$$

Traction Forces.

Front wheel motors \rightarrow MS18.

Assume ① Torque @ 100 Bar = 3098 Nm.

② Rolling Radius = 631 mm.

\therefore Max Thrust assuming Torque limited NOT Traction limited (op pressure 100 Bar)

$$\Rightarrow \frac{3098}{0.631} = 4909 \text{ N, cutting through contact patch.}$$

However assume op pressure is 420 Bar @ motor

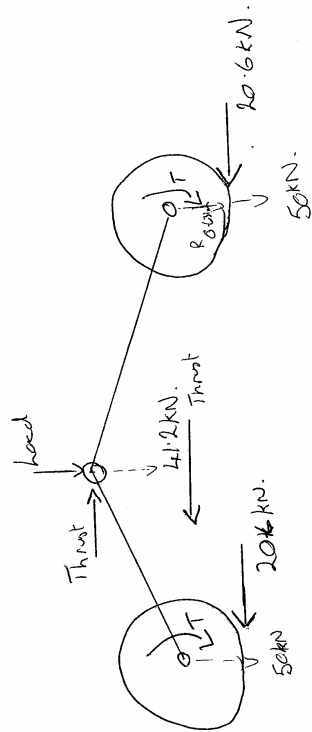
$$\therefore \frac{13012}{0.631} = 20621 \text{ N Thrust}$$

\Rightarrow 41242 N per Axle side.

NB. $13012 = 3098 \left(\frac{420}{100} \right)$

$$T = 3098 \text{ Nm}$$

$$\text{COT} \approx 0.5$$



15.1.3 Side Impact

19-103-143

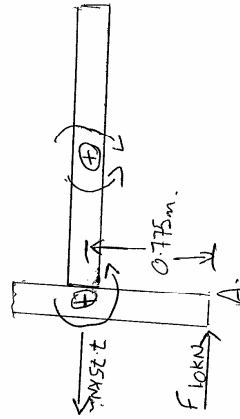
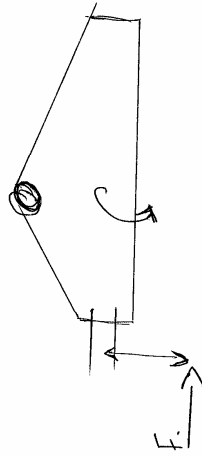
Side Impact on 1 tyre.

$$F = 10\text{kN}.$$

$$x = 0.775\text{m}.$$

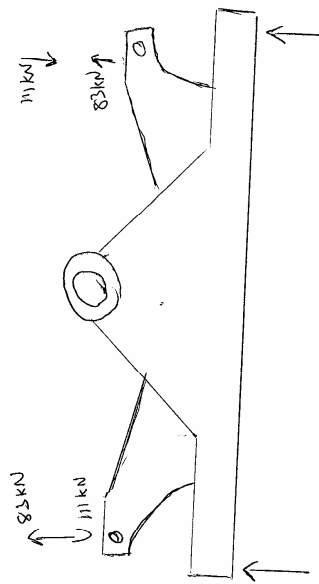
$$M_A \Rightarrow Fx$$

$$\Rightarrow 7.75\text{ kNm}.$$



15.1.4 Levelling Rams

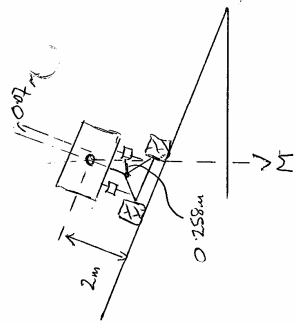
979-103-143.
Levelling Rams.



Hyd Press = 220 Bar, 22 MPa

Hyd Ram - 80mm bore, 40mm piston : Area $5026 \text{ mm}^2 + 3770 \text{ mm}^2$

Max loads Hyd Applied \Rightarrow 83 kN Vertical (\uparrow)
111 kN Vertical (\downarrow)



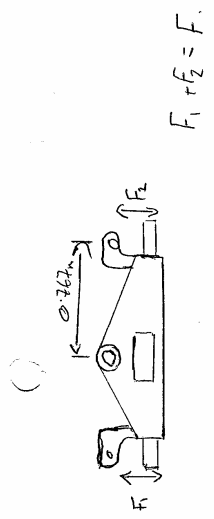
Derivation of M.

M = mass above pivot point.

- Wheels 0.26 x 6
- Wheel motors 0.22 x 6
- Beams 0.32 x 2
- Front Axle 0.52
- Rear Axle Assy 0.74
- Rear Axle Motor 0.05 x 2
- Hyd
- Rear Levelling Frame 0.55
- 5.48

Book weight of machine 26120 kg

∴ M above Axle = 20640 kg.



OM = overturning moment.

$$OM = 20640 \times 9.81 \times 0.258 = 52240 \text{ Nm.}$$

$$F = OM / 0.767 / 2.$$

= 34054 N. This is case when machine is perfectly level.

Radi. of hyd Ram potential.

$$\frac{85}{194}, \frac{111}{194} \Rightarrow 0.42, 0.58.$$

$$\therefore F_1 = 14751 \text{ N. } \downarrow$$

$$F_2 = 14302 \text{ N. } \uparrow$$

This occurs when machine is levelling on max side slope.

15.1.5 Stub Axle Calculation